



<https://theses.gla.ac.uk/>

Theses Digitisation:

<https://www.gla.ac.uk/myglasgow/research/enlighten/theses/digitisation/>

This is a digitised version of the original print thesis.

Copyright and moral rights for this work are retained by the author

A copy can be downloaded for personal non-commercial research or study,  
without prior permission or charge

This work cannot be reproduced or quoted extensively from without first  
obtaining permission in writing from the author

The content must not be changed in any way or sold commercially in any  
format or medium without the formal permission of the author

When referring to this work, full bibliographic details including the author,  
title, awarding institution and date of the thesis must be given

Enlighten: Theses

<https://theses.gla.ac.uk/>  
[research-enlighten@glasgow.ac.uk](mailto:research-enlighten@glasgow.ac.uk)

# **Developments and Applications in Solid-State NMR Spectroscopy**

Submitted in partial fulfilment of the requirements  
for the degree of Doctor of Philosophy

Marica Cutajar  
University of Glasgow  
Department of Chemistry  
August 2008

ProQuest Number: 10800639

All rights reserved

INFORMATION TO ALL USERS

The quality of this reproduction is dependent upon the quality of the copy submitted.

In the unlikely event that the author did not send a complete manuscript and there are missing pages, these will be noted. Also, if material had to be removed, a note will indicate the deletion.



ProQuest 10800639

Published by ProQuest LLC (2018). Copyright of the Dissertation is held by the Author.

All rights reserved.

This work is protected against unauthorized copying under Title 17, United States Code  
Microform Edition © ProQuest LLC.

ProQuest LLC.  
789 East Eisenhower Parkway  
P.O. Box 1346  
Ann Arbor, MI 48106 – 1346

GLASGOW  
UNIVERSITY  
LIBRARY

# Abstract

---

Recently there has been a lot of interest in using  $^2\text{H}$  ( $I = 1$ ) MAS NMR as an alternative method to 'static'  $^2\text{H}$  quadrupolar-echo NMR for studying dynamics on the  $\mu\text{s}$  timescale in solids. This thesis discusses two novel observations that increase the usefulness of the MAS approach.

The spinning sidebands observed in  $^2\text{H}$  MAS NMR spectra may be very strongly broadened if  $\mu\text{s}$ -timescale dynamics are present. In Chapter 4, it will be shown that the usefulness of this phenomenon for the study of motion is significantly enhanced by the fact that this motional broadening is either absent or greatly reduced in the corresponding  $^2\text{H}$  double-quantum MAS spectrum. A comparison of linewidths in the single- and double-quantum dimensions in a two-dimensional  $^2\text{H}$  double-quantum MAS NMR experiment provides a very sensitive test for the presence of dynamics. Various simple deuterated materials, organic and inorganic, as well as a synthetic polymer will be used as examples to show how results drawn from the  $^2\text{H}$  double-quantum MAS NMR experiment yield information about the dynamics of the system.

$^2\text{H}$  quadrupolar-echo NMR studies of static solids are often hampered by the presence of very long spin-lattice ( $T_1$ ) relaxation times, up to several minutes for immobile deuterons. In Chapter 5, therefore, it will be shown that this problem is often not present in  $^2\text{H}$  MAS NMR studies, where the phenomenon of rotational resonance, governed by spin diffusion can lead to the observation of a common  $T_1$  relaxation time for all deuterons in the solid state. Thus, if rapidly relaxing methyl group (or similar) deuterons are present, even highly immobile deuterons can exhibit  $T_1$  relaxation times of less than 1 s under MAS conditions, greatly facilitating data acquisition. To illustrate this phenomenon, experimental examples using  $^2\text{H}$  NMR of deuterated materials will be shown and discussed.

In the last chapter, solid-state MAS NMR spectroscopy is used to further investigate structure and framework topology of aluminophosphates. This is done by exploiting scalar ( $J$ ) couplings across the Al-O-P bonds to obtain a heteronuclear correlation (HETCOR) between  $^{27}\text{Al}$  and  $^{31}\text{P}$  which allows us to obtain spectra that show through-bond connectivities between the two respective nuclei. We show that using a MQMAS experiment in combination with a refocused INEPT HETCOR (MQ- $J$ -HETCOR) experiment we can obtain important information about AlPOs that x-ray diffraction techniques fails to yield. In addition to two-dimensional NMR experiments, 'first-principles' calculations are used to help and confirm the assignment of the spectra obtained.

# Acknowledgements

---

I would like to first of all thank Prof. Steve Wimperis, for his patience and support throughout these past few years. I must also thank Dr. Sharon Ashbrook for being always there and for her invaluable assistance in using the NMR machines. A big thank you goes to Thomas Ball for simply being there throughout this journey, without him this PhD would not have been the same. I am also eternally grateful to Michael for being always available to answer all of my questions and helping me grasp many concepts of NMR. I would like to thank Teresa, for balancing the group out, both because she happens to be female as well as foreign. I would like to also thank all the academic and technical staff at the Department of Chemistry for the friendly support and help they have given me.

Finally I would like to thank my family and friends that have been there for me unconditionally whenever I needed them.

To Nicholas

# Table of contents

---

<b>Abstract</b>	iii
<b>Acknowledgements</b>	iv
<b>Dedication</b>	v
<b>Table of Contents</b>	vi
<b>1. Introduction</b>	<b>1</b>
1.1 A Brief History of NMR	1
1.2 Thesis overview	5
<b>2. Fundamentals</b>	<b>8</b>
2.1 Basic NMR Theory	8
2.1.1 <i>Spin angular momentum and the magnetic field</i>	8
2.1.2 <i>The vector model</i>	11
2.1.3 <i>The FID and <math>T_1</math> and <math>T_2</math> relaxation</i>	13
2.1.4 <i>Fourier transform NMR</i>	15
2.1.5 <i>Two-dimensional NMR</i>	16
2.2 The Density Operator Formalism	17
2.2.1 <i>Introduction</i>	17
2.2.2 <i>The time evolution of the density operator</i>	19
2.2.3 <i>Operator formalisms</i>	22
2.2.4 <i>The Liouville formalism</i>	26
2.3 The Nuclear Spin Hamiltonian	28
2.3.1 <i>Introduction</i>	28
2.3.2 <i>Free precession</i>	29
2.3.3 <i>Radiofrequency pulses</i>	29
2.4 Shielding and Chemical Shift	30
2.5 Spin-Spin Coupling: Dipolar and Scalar Interaction	33
2.5.1 <i>Introduction</i>	33
2.5.2 <i>Dipolar coupling</i>	34
2.5.3 <i>Scalar (J) coupling</i>	39

2.6	Quadrupolar Interaction	41
2.6.1	<i>Introduction</i>	41
2.6.2	<i>First-order quadrupolar broadening for spin <math>I = 1</math> nuclei</i>	44
2.6.3	<i>First- and second-order quadrupolar broadening for spin <math>I = 1</math> nuclei</i>	47
<b>3.</b>	<b>Essential Techniques for Solid-State NMR</b>	<b>52</b>
3.1	Introduction	52
3.2	Coherence Selection	52
3.3	Spin-Echo Pulse Sequences	54
3.4	Magic Angle Spinning (MAS)	57
3.4.1	<i>Theory</i>	57
3.4.2	<i>Experimental example</i>	61
3.4.3	<i>Rotor synchronization</i>	63
3.5	Heteronuclear Decoupling	64
3.6	Insensitive Nuclei Enhance by Polarization Transfer (INEPT)	66
3.7	Multiple-Quantum Magic Angle Spinning (MQMAS)	68
3.8	Frequency Discrimination in Two-Dimensional Experiments	71
<b>4.</b>	<b><math>^2\text{H}</math> double-quantum MAS NMR spectroscopy as a probe of dynamics on the microsecond timescale</b>	<b>77</b>
4.1	Introduction	77
4.2	Literature Review	81
4.3	The Effect of Dynamics on Quadrupolar Lineshapes	83
4.4	Theory of Motional Broadening in Solids Under MAS	88
4.4.1	<i>Introduction</i>	88
4.4.2	$^2\text{H}$ MAS NMR	89
4.4.3	<i>The spin-echo model</i>	90
4.5	Experimental Procedures	94
4.5.1	<i>The double-quantum MAS NMR experiment</i>	94
4.5.2	<i>Experimental details</i>	98
4.6	Results	98
4.6.1	<i>Introduction</i>	98
4.6.2	<i>Oxalic acid dihydrate-<math>d_6</math></i>	99
4.6.3	<i>Sodium tetrathionate dihydrate-<math>d_4</math></i>	105

4.6.4 Calcium sulfate dihydrate- $d_4$	109
4.6.5 Poly(methyl methacrylate- $d_8$ ) – PMMA	111
4.6.6 Hydroxyl-clinohumite- $d_8$	116
4.6 Conclusions	120
<b>5. Effects of spin diffusion on spin-lattice relaxation in solid-state</b>	
$^2\text{H}$ MAS NMR spectroscopy	121
5.1 Introduction	121
5.2 Theoretical Background	123
5.2.1 Spin-lattice relaxation time $T_1$	123
5.2.2 Determination of spin-lattice relaxation times	124
5.2.3 Rotational resonance	125
5.2.4 The effects of spin diffusion on spin-lattice relaxation – a simple model	128
5.3 Review of Previously Documented $^2\text{H}$ MAS NMR Spin-Lattice Relaxation Studies	132
5.3.1 Alla, Eckman and Pines discussion	132
5.3.2 Gan and Robyr discussion	134
5.4 Experimental Procedures and Results	135
5.4.1 Experimental details	135
5.4.2 L-alanyl-glycine (ala-gly- $d_4$ )	135
5.4.3 Poly(methyl methacrylate- $d_8$ ) – PMMA	140
5.4.4 Dimethyl terephthalate- $d_{10}$	141
5.5 Conclusions	148
<b>6. Structure and NMR assignments in microporous</b>	
<b>aluminophosphates (AlPOs)</b>	150
6.1 Introduction	150
6.2 Aluminophosphates (AlPOs)	151
6.3 Heteronuclear NMR Experiments	153
6.3.1 The MQ-J-HETCOR experiment	153
6.3.2 The HMQC experiment	156
6.4 Experimental Details	158
6.5 AlPO-14: Results and Discussion	160
6.5.1 AlPO-14: An Overview	160

6.5.2 <i>AlPO-14 ipa</i>	163
6.5.3 <i>AlPO-14 pip</i>	169
6.5.4 <i>Calcined-dehydrated AlPO-14</i>	173
6.6 <b>AlPO-53: Results and Discussion</b>	177
6.6.1 <i>AlPO-53: An Overview</i>	177
6.6.2 <i>Calcined-dehydrated AlPO-53(B)</i>	178
6.6.3 <i>AlPO-53(A)</i>	183
6.7 <b>Conclusions</b>	191
<b>Appendix A</b>	192
<b>Appendix B</b>	193
<b>References</b>	194

---

## Chapter 1

### Introduction

---

#### 1.1 A Brief History of NMR

In 1945, the first nuclear magnetic resonance (NMR) signal was observed by two separate groups; Purcell and his colleagues in Harvard [1.1], and Bloch and his group in California [1.2]. The Purcell group observed NMR signal from protons in paraffin wax, while the Bloch group detected  $^1\text{H}$  signal from water molecules. Their work was rewarded by a joint Nobel Prize in physics in 1952 'for their development of new methods for nuclear magnetic precision measurements and discoveries in connection therewith'. Within a decade, nuclear magnetic resonance NMR spectroscopy had become recognized as an important analytical tool for investigating chemical structures through the observation of spectra produced by hydrogen nuclei.

The first commercial high-resolution continuous wave (CW) proton NMR spectrometer was produced in 1953 and was an integral part of every research laboratory for many years until the arrival of the Fourier transform (FT) technique, introduced by Ernst in the 1970s [1.3].

FT NMR eased problems associated with nuclei that were less sensitive due to their low natural abundance compared with protons such as  $^{13}\text{C}$ . Commercial FT spectrometers were introduced shortly after the work done by Ernst for which he was awarded the Nobel Prize in chemistry 'for his contributions to the development of the methodology of high resolution NMR spectroscopy' in 1991.

In 1971, two-dimensional NMR was introduced by Jeener [1.4] and since then the NMR community has been working on FT techniques in one-, two- and more dimensions. The development and availability of superconducting magnets has made possible the use of higher fields, which coupled with advances in computing technology allowed the possibility of data processing in a reasonable amount of time.

Solid-state NMR started to be widely used about thirty years ago. Studying solids using NMR resulted to be an extremely challenging task in part because of the rigidity of solid materials. The lack of thermal motion results in a collection of crystallites, each in a slightly different electronic environment and hence each producing a different frequency, producing several overlapping signals, consequently making it difficult to interpret the spectra obtained.

However, Andrew *et al.* [1.5, 1.6] introduced the magic angle spinning (MAS) technique, which started the development of high-resolution solid-state nuclear magnetic resonance. The MAS technique increases the resolution by several orders of magnitude. It involves

rapidly rotating a rotor (the sample container) holding the powdered sample at a spinning axis of  $54.74^\circ$  (the magic angle) to the external magnetic field. Better resolution is obtained by using magic angle spinning because the rotation of the sample about the magic averages out interactions that would otherwise broaden the NMR spectra. Such interactions are the first-order quadrupolar interaction, the chemical shift anisotropy (CSA) and the dipolar coupling [1.7]. Unfortunately most quadrupolar nuclei are affected by other, higher order quadrupolar interactions that are not completely removed by MAS. Amongst others, Pines together with Waugh continued to transform solid-state NMR with the introduction of the cross-polarization technique to help enhance the sensitivity of low abundance nuclei [1.8].

Although most NMR experiments are still performed on liquids, solid-state NMR has become a very popular technique. The ability to use NMR to analyse solid materials brings many advantages for chemists working with powdered materials. Firstly, it avoids the potential change in the chemical properties that might occur while melting or dissolving a solid material while converting it into a liquid. Secondly, with solid-state NMR one has the option of retaining important information about the material, such as the anisotropy of the nuclear spin interactions, which are often completely removed when dealing with a liquid sample. In addition, studying solid materials can give useful information about internal dynamics of systems which, in turn, helps in determining the chemical and physical properties of a material.

This thesis is predominantly going to deal with NMR in the solid-state of nuclei with a spin quantum number,  $I > 1/2$ , or otherwise known as quadrupolar nuclei. These nuclei are dominated by the quadrupolar interaction and the MAS technique is going to be used extensively throughout this work to improve resolution and help in the interpretation of the spectra obtained.

Apart from MAS, several techniques have been developed to help eliminate the second-order quadrupolar interaction. Two techniques that completely remove the second-order quadrupolar broadening are double rotation (DOR) [1.9, 1.10] and dynamic angle spinning (DAS) [1.11]. In a DOR setup, the sample is packed into a smaller inner rotor that is embedded into a larger outer rotor. The inner rotor axis is inclined with respect to the axis of the outer rotor at an angle of typically  $30.56^\circ$ . In other words, the material would be spun about two different axes simultaneously. On the other hand, in DAS the sample is spun about two angles in succession:  $30.56^\circ$  and the magic angle. Both DOR and DAS, however have their limitations. In DOR, the maximum spinning speed currently achievable is around 1 kHz, and hence the spectra obtained may consist of a large amount of peaks known as spinning sidebands, making analysis difficult. Fast DAS rate is also impossible to achieve. In addition, the radiofrequency probe used for DOR is located around the outer rotor and hence further away from the sample when compared to a conventional MAS probe, consequently making DOR a less sensitive technique than MAS. Moreover, since both techniques require the spinning of the sample around two axes of rotation, more specialized

equipment is needed for their implementation. For these reasons, both DOR and DAS are not very commonly used techniques.

Other methods used to remove second-order broadening are two-dimensional coherence transfer NMR experiments such as the multiple-quantum (MQ) MAS introduced by Frydman and Harwood [1.12] and the satellite-transition (ST) MAS techniques developed by Gan [1.13]. Both techniques yield isotropic spectra free from orientationally-dependent broadenings. In addition, both techniques require the same experimental equipment as used to acquire MAS spectra.

## 1.2 Thesis Overview

Chapter 2 of this thesis is going to start by discussing the basic principles of NMR, and then moves on to give an understanding of the interactions that contribute to the broadening of solid-state NMR spectra. The chemical shift, spin-spin coupling and the quadrupolar interactions are amongst the nuclear spin interactions discussed in this Chapter. Chapter 3 outlines essential techniques used in solid-state NMR. The aim of this chapter is to set a good understanding of all the techniques that will eventually be used in the experimental sections of this thesis.

Chapters 4 and 5 present work done using deuterium as the nucleus of interest.  $^2\text{H}$  is a spin  $I = 1$  nucleus and has been extensively

used over the past few decades as an NMR probe of structure and dynamics in solid materials. In Chapter 4, a two-dimensional  $^2\text{H}$  double-quantum MAS NMR experiment that correlates single- and double-quantum coherences will be used to obtain information about reorientational dynamics [1.14]. The method is presented here as an alternative to the 'static'  $^2\text{H}$  quadrupolar-echo NMR method conventionally used for studying dynamics on the  $\mu\text{s}$  timescale [1.15].

One of the aims of Chapter 5 is to emphasize one of the many advantages of using the double-quantum MAS NMR experiment introduced in Chapter 4, over static NMR methods. Here, a study of the spin-lattice relaxation time,  $T_1$ , of deuterated materials is carried out. Results obtained show that the very long  $T_1$  hampering static NMR experiments is often not present in MAS NMR studies. This observation is compared with similar observations already described in the literature [1.16, 1.17].

Finally in Chapter 6, high-resolution NMR techniques are used to further investigate the structure and framework topology of aluminophosphates. Interest in this family of materials is increasing as they can be potentially used as catalysts and sorbents. Consequently a lot of work has been done over the past decade to try and attain a better understanding of their chemical and physical properties. In this case this was achieved by using a MQMAS experiment, in combination with a refocused INEPT heteronuclear (MQ-J-HETCOR) experiment to obtain structural information [1.18]. To confirm the NMR parameters obtained

and hence the assignment of the correlation spectra, 'first-principles' calculations were carried out [1.19].

---

## Chapter 2

### Fundamentals

---

#### 2.1 Basic NMR Theory

##### 2.1.1 *Spin angular momentum and the magnetic field*

Nuclear spins possess an intrinsic angular momentum. The spin angular momentum,  $I$ , is a vector quantity, with quantized direction and magnitude. The magnitude of  $I$  is given by:

$$|I| = [I(I+1)]^{\frac{1}{2}} \hbar, \quad (2.1)$$

where  $I$  is the spin quantum number. The angular momentum of a nucleus can have  $2I+1$  possible orientations. The orientations remain degenerate unless exposed to a magnetic field,  $B_0$ , and can be represented by energy levels. The z-component of this vector,  $I_z$ , is given by:

$$I_z = m\hbar, \quad (2.2)$$

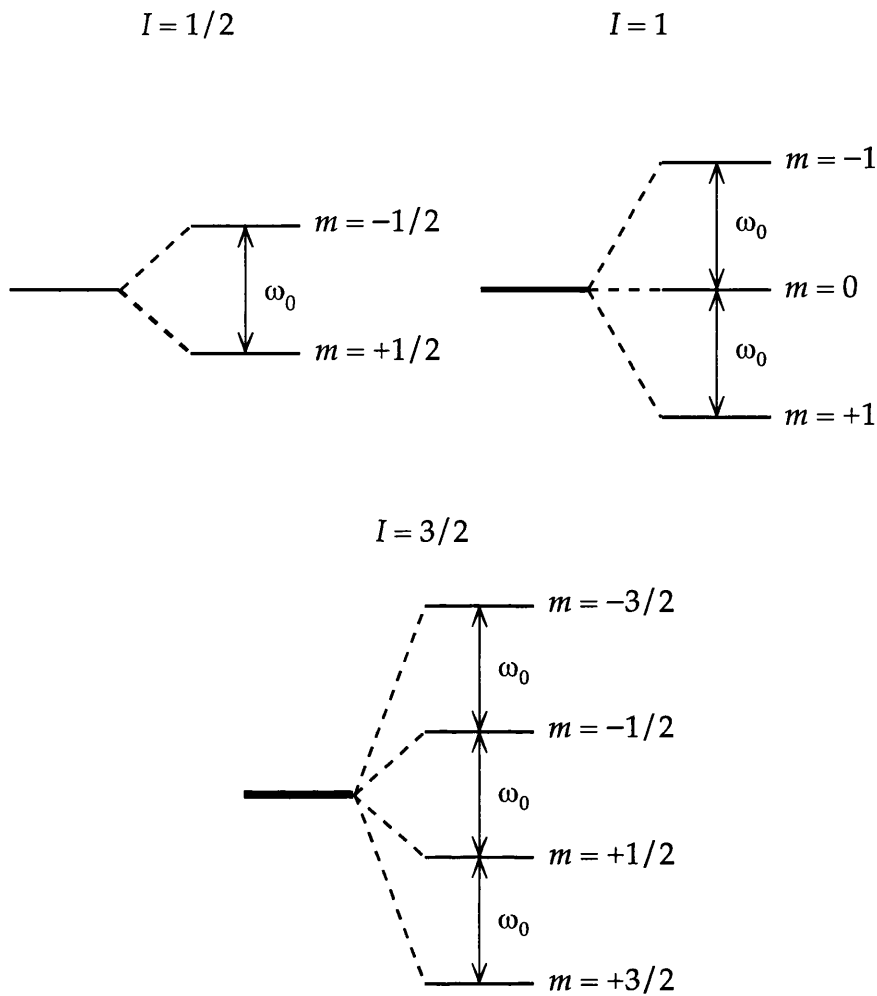


Figure 2.1: Energy level diagram for spin  $I = 1/2, 1$  and  $3/2$  nuclei. Energy levels have the same energy, until an external magnetic field  $B_0$  is applied. When exposed to  $B_0$ , the degeneracy is lost, and the energy levels are split by the Larmor frequency  $\omega_0$ .

where  $m$  is known as the magnetic quantum number and can take  $2I + 1$  values in integral steps between  $+I$  and  $-I$ . When placed in a magnetic field, the degeneracy of the  $2I + 1$  states is removed and each energy level is labelled with its unique magnetic quantum number, as shown in Fig. 2.1. The energy for a particular energy level is given by:

$$\begin{aligned}
 E &= -\mu_z B_0 \\
 &= -m\hbar\gamma B_0,
 \end{aligned}
 \tag{2.3}$$

where  $\mu_z$  is the z-component of the magnetic moment  $\boldsymbol{\mu}$ , which is proportional to the spin angular momentum  $I$ :

$$\boldsymbol{\mu} = \gamma I,
 \tag{2.4}$$

where the constant of proportionality  $\gamma$  is called the gyromagnetic ratio, a parameter which is unique to each magnetic isotope.

The selection rule for an observable transition in NMR refers to the transitions that occur between adjacent spin states, i.e.,  $\Delta m = \pm 1$ . The difference in energy between these transitions can be written as:

$$\begin{aligned}
 \Delta E &= h\nu_0 \\
 &= \hbar\gamma B_0,
 \end{aligned}
 \tag{2.5}$$

where the frequency of the electromagnetic radiation,  $\nu_0$ , is known as the Larmor frequency and is measured in Hz. The Larmor frequency can also be expressed in angular frequency  $\omega_0$  and hence measured in  $\text{rad s}^{-1}$ :

$$\omega_0 = -\gamma B_0.
 \tag{2.6}$$

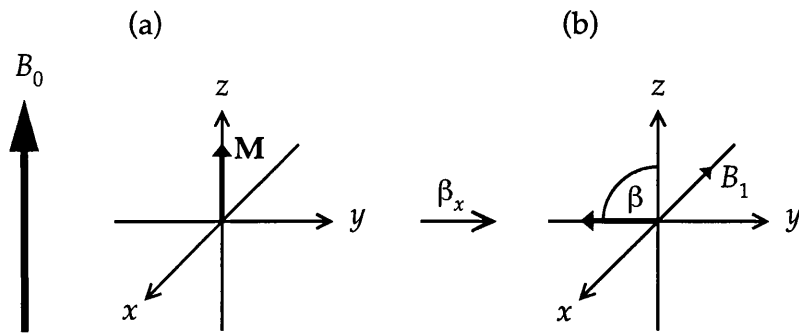


Figure 2.2: The vector model description of the effect of a pulse of strength  $B_1$  along the  $x$ -axis on the bulk magnetization vector  $M$ . The pulse causes  $M$  to nutate through flip angle  $\beta = 90^\circ$ .

### 2.1.2 The vector model

The 'vector model', introduced by Bloch [2.1], gives a simple geometric picture that helps visualize what happens during pulsed NMR experiments. However, because of its simplicity, it is a rather limited approach when dealing with complex NMR experiments such as those discussed later on in this thesis.

Consider a material at thermal equilibrium. At this point in time, the energy levels are populated with the nuclei according to the Boltzmann distribution, resulting into what is known as the bulk magnetization vector  $M$  along the  $z$ -axis of the applied magnetic field  $B_0$ , as shown schematically in Fig. 2.2a. If the material is subjected to a pulse of linearly oscillating radiofrequency (rf) with a frequency  $\omega_{rf}$  and a magnetic field strength of  $B_1$ , the bulk magnetization vector would be deflected from the equilibrium position along the  $z$ -axis and rotates about  $B_1$  at an angle  $\beta$  with respect to  $B_0$ , as shown in Fig. 2.2b.

It is rather complicated to picture the combined effect of the static magnetic field and the radiofrequency field  $B_1$  on  $\mathbf{M}$  in the laboratory frame and hence could be viewed more conveniently in the rotating frame. The rotating frame is a frame of reference that is rotating at the same frequency about the  $z$ -axis as that of the pulse applied. A pulse can be viewed as two counter-rotating fields with frequencies  $+\omega_{rf}$  and  $-\omega_{rf}$ , one rotating in the same direction as  $\omega_0$ , hence could be viewed as being static, and the other rotating in the opposite direction at a frequency of  $-\omega_{rf}$ .

The angle of tilt,  $\beta$ , also known as the 'flip angle', is defined as:

$$\begin{aligned}\beta &= -\gamma B_1 \tau_p \\ &= \omega_1 \tau_p,\end{aligned}\tag{2.7}$$

where  $\tau_p$  is the duration of the pulse and  $\omega_1 = -\gamma B_1$ , which corresponds to the frequency with which  $\mathbf{M}$  precesses about an on-resonance pulse. After the pulse is applied,  $\mathbf{M}$ , precesses at a frequency offset,  $\Omega$ , in the rotating frame:

$$\Omega = \omega_0 - \omega_{rf}.\tag{2.8}$$

This is called 'free precession' and it is affected by relaxation processes, which eventually cause  $\mathbf{M}$  to return to its original position along the  $z$ -axis. Using the vector model, Fig. 2.3 illustrates the free precession period  $t$ . When  $\Omega = 0$ ,  $\mathbf{M}$  will not precess at all in the rotating frame, and will

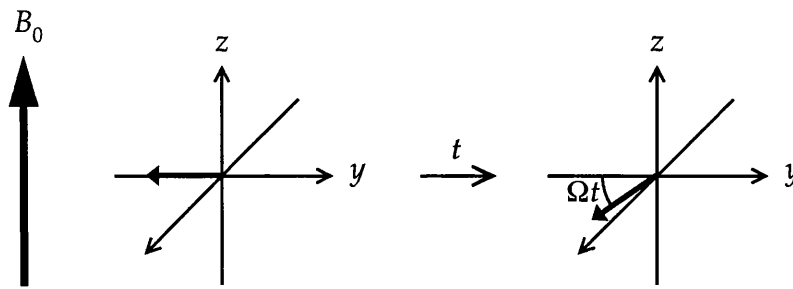


Figure 2.3: The vector model description of a free precession interval  $t$ , which allows  $\mathbf{M}$  to evolve with the offset frequency  $\Omega$ .

remain on the  $-y$ -axis. When  $\Omega \neq 0$ ,  $\mathbf{M}$  will precess about  $B_0$  sweeping out an angle  $\Omega t$  in a time  $t$ .

### 2.1.3 The FID and $T_1$ and $T_2$ relaxation

In the laboratory frame,  $\mathbf{M}$  precesses around  $B_0$  and the component in the  $xy$ -plane induces a current, which produces a free induction decay or FID. This signal does not oscillate forever, implying that  $\mathbf{M}$  does not precess indefinitely due to relaxation effects.

After a rf pulse, all energy levels become equally populated and then, after certain amount of time, depending on the material under test, the system returns to its thermal equilibrium state. This process is known as relaxation. The return of the  $z$ -component of  $\mathbf{M}$  to thermal equilibrium is known as spin-lattice or longitudinal relaxation and is characterized by the time constant  $T_1$ . Spin-lattice relaxation and how it is measured will be discussed in more detail in Chapter 5. In contrast, the loss of

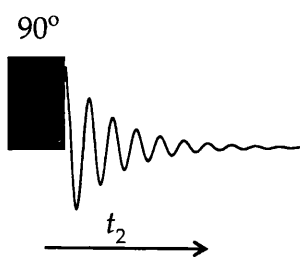


Figure 2.4: The pulse sequence for a simple NMR experiment.

magnetization from the  $xy$ -plane is known as spin-spin or transverse relaxation and is characterized by the time constant  $T_2$ .

Quadrature detection is the method generally used to acquire the FID. This method is equivalent to having two detectors placed orthogonal to each other (i.e., one along the  $x$ - and one along the  $y$ -axis) in the rotating frame and, therefore, acquiring a FID containing two components at the same time,  $90^\circ$  out of phase [2.2]. These two signal components are commonly referred to as the real and imaginary parts of the FID. Quadrature detection is necessary to determine the sense of precession of  $M$ . The detected signal is then digitized, which involves sampling data points at regular intervals.

Figure 2.4 shows the simplest NMR pulse sequence. A pulse-sequence describes the timing of events during the particular NMR experiment. The pulse sequence is written and stored on the computer-controlled spectrometer as a computer program known as the pulse program. Pulses are shown as shaded blocks and the oscillating line represents the FID that is detected during the acquisition period. All the

experiments discussed in this dissertation will be depicted in this manner.

#### 2.1.4 Fourier transform NMR

A Fourier transformation (FT) [2.3] is the operation that converts functions from the time domain (FID) to the frequency domain (spectrum) and vice-versa. For each resonance present in any given spectrum, the real and imaginary parts of the FID correspond to a cosine and a sine function of  $\Omega$ , decaying with a rate constant  $1/T_2$ . Hence, the time-domain signal,  $s(t_2)$ , for  $t_2 \geq 0$ , can be written as follows:

$$\begin{aligned} s(t_2) &= [\cos(\Omega t_2) + i \sin(\Omega t_2)] \exp(-t_2/T_2) \\ &= \exp(i\Omega t_2) \exp(-t_2/T_2), \end{aligned} \quad (2.9)$$

Upon Fourier transformation,  $s(t_2)$  can be converted into the corresponding frequency-domain function,  $S(\omega)$ :

$$\begin{aligned} S(\omega) &= \int_{-\infty}^{\infty} s(t_2) \exp(-i\omega t_2) dt \\ &= A(\Delta\omega) - iD(\Delta\omega), \end{aligned} \quad (2.10)$$

with:

$$A(\Delta\omega) = \frac{1/T_2}{(1/T_2)^2 + (\Delta\omega)^2} \quad \text{and} \quad D(\Delta\omega) = \frac{\Delta\omega}{(1/T_2)^2 + (\Delta\omega)^2}, \quad (2.11)$$

where  $\Delta\omega = \omega - \Omega$ ,  $A(\Delta\omega)$  represents the absorptive (real) Lorentzian curve, centred at frequency  $\Omega$ , and  $D(\Delta\omega)$  is the dispersive (imaginary)

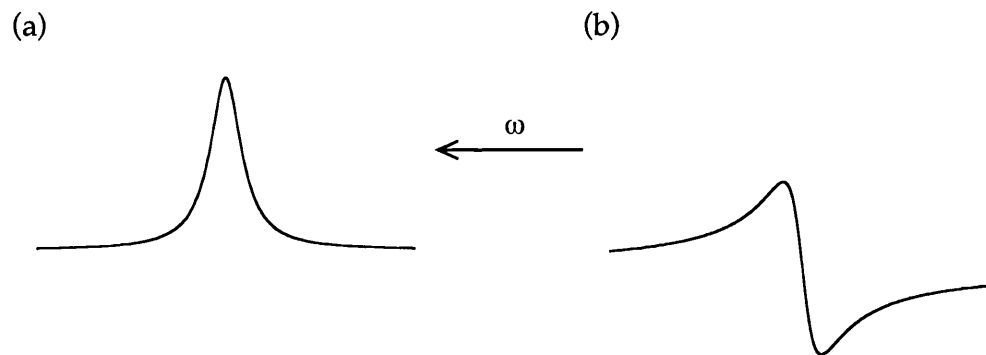


Figure 2.5: The (a) real and (b) imaginary Lorentzian lineshapes acquired using quadrature detection.

Lorentzian as shown in the computer-simulated one-dimensional Lorentzian lineshapes in Fig. 2.5a and Fig. 2.5b, respectively.

### 2.1.5 Two-dimensional NMR

Very simply, a two-dimensional NMR spectrum is a plot of intensity against two frequencies rather than one. This is achieved by adding an 'evolution' or  $t_1$  period, and a 'mixing' period to the one-dimensional NMR pulse sequence illustrated in Fig. 2.4. A simple two-dimensional NMR experiment is shown in Fig. 2.6.

The  $t_1$  period is a time that is incremented systematically, during which spins precess without interruption. The pulse sequence is then repeated with different values for  $t_1$ . Each value of  $t_1$  will yield a FID; therefore after  $x$  increments,  $x$  FIDs of length  $t_2$  will be available for processing, and each one, if Fourier transformed, will produce a one-dimensional spectrum. A Fourier transform of a two-dimensional spectrum can be viewed as a combination of two Fourier transforms; FT

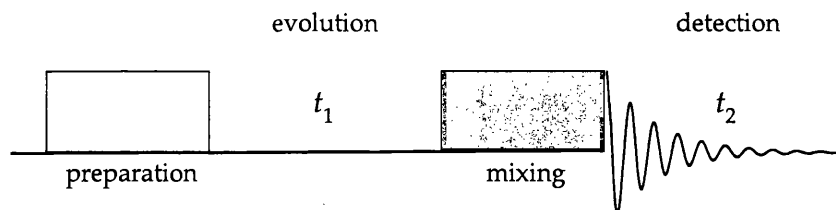


Figure 2.6: The general pulse sequence for a two-dimensional NMR experiment.

of the  $x$  FIDs in the  $t_1$  dimension followed by that of the  $t_2$  dimension, which produces a peak or more, each having intensity and two frequency coordinates.

## 2.2 The Density Matrix Formalism

### 2.2.1 Introduction

In quantum mechanics, the state of a system can be described by a function  $|\Psi\rangle$  known as the wavefunction [2.5] and can be written as a linear combination of a set of orthogonal basis states  $|i\rangle$ :

$$|\Psi\rangle = \sum_i c_i |i\rangle. \quad (2.12)$$

where the  $c_i$  are coefficients that may change over time. When a system is described by a wavefunction, the mean value of the observable quantity is equal to the expectation value of the corresponding operator,  $A$ . The expectation value of  $A$  for a particular  $|\Psi\rangle$  is defined as:

$$\langle \Psi | A | \Psi \rangle = \sum_i \sum_j \overline{c_i^* c_j} \langle j | A | i \rangle . \quad (2.13)$$

Equation (2.13) shows that the expectation value of any observable always depends on the same products,  $c_i^* c_j$ , where \* marks the complex conjugate and the overbar is used to symbolize the ensemble average, which is what will be considered when dealing with an NMR sample. This property leads to the definition of the density operator  $\sigma(t)$ .

The density operator formalism [2.4] is essentially a quantum-mechanical method that helps understanding the behaviour of a spin system during an NMR experiment. It is designed to yield exact and hence far more accurate information than that obtained using the simple vector model discussed earlier. In addition, this approach can deal with more complex NMR experiments that could not be described by using the vector model.

The density operator is most conveniently described using the density matrix,  $\sigma$ . The elements,  $\sigma_{i,j}$ , of the matrix are given by the products of the coefficients of the wavefunction  $|\Psi\rangle$ :

$$\begin{aligned} \sigma_{i,j} &= \langle i | \sigma | j \rangle \\ &= \overline{c_i^* c_j} , \end{aligned} \quad (2.14)$$

It follows that, if the ensemble average is considered and by substituting in Eq. (2.14), Eq. (2.13) becomes:

$$\langle \Psi | A | \Psi \rangle = \sum_{i,j} \langle i | \sigma | j \rangle \langle j | A | i \rangle . \quad (2.15)$$

Using the completeness theorem [2.5], which states that:

$$\sum_n |n\rangle \langle n| = 1 , \quad (2.16)$$

Equation (2.15) can be simplified to:

$$\langle \Psi | A | \Psi \rangle = \sum_i \langle i | \sigma A | i \rangle . \quad (2.17)$$

The right-hand side of Eq. (2.17) corresponds to the trace of the product of the matrix representation of the operator and the density matrix:

$$\text{Tr}\{\sigma A\} . \quad (2.18)$$

### 2.2.2 *The time evolution of the density operator*

In quantum mechanics, the Hamiltonian,  $H$ , represents the observable operator that corresponds to the total energy of the system:

$$H|\Psi\rangle = E|\Psi\rangle . \quad (2.19)$$

Equation (2.19) is the time-independent Schrödinger equation, which is an eigenvalue equation where  $|\Psi\rangle$  and  $E$  are an eigenfunction and an eigenvalue of the operator  $H$ , respectively. In NMR, the Zeeman interaction, given by the Hamiltonian,  $H_Z$ :

$$H_Z = \omega_0 I_z , \quad (2.20)$$

is always the interaction that dominates as all the other interactions that will be discussed in this chapter will be considerably weaker than the Zeeman interaction. The eigenvalues of  $I_z$  as well as the operators corresponding to the  $x$  and  $y$  angular momenta for any spin system can be conveniently written in matrix form. The matrix representations of the spin angular momentum operators are given in Appendix A.

The wavefunction  $|\Psi(t)\rangle$  describes the state of the system at time  $t$  and evolves in time according to the equation:

$$H|\Psi(t)\rangle = i\frac{d}{dt}|\Psi(t)\rangle . \quad (2.21)$$

Equation (2.21) is the time-dependent Schrödinger equation. In this case the Hamiltonian governs the time-evolution behaviour of the quantum states.

The time evolution of the density matrix is given by the well-known Liouville-von Neumann equation [2.6], which can be derived from the time-dependent Schrödinger equation (Eq. (2.21)), which can be written in the form:

$$\sum_k \frac{dc_k(t)}{dt} |k\rangle = -iH(t) \sum_k c_k(t) |k\rangle \quad (2.22)$$

Premultiplying Eq. (2.22) by  $\langle i|$  and assuming an ensemble average:

$$\frac{dc_i(t)}{dt} = -i \sum_k \langle i|H(t)|k\rangle c_k(t) . \quad (2.23)$$

Similarly:

$$\frac{dc_j(t)^*}{dt} = -i \sum_k c_k(t)^* \langle k|H(t)|j \rangle . \quad (2.24)$$

It follows that, by using Eq. (2.14), Eq. (2.24) can be rewritten in terms of the density operator:

$$\frac{d\sigma_{ij}(t)}{dt} = c_i(t) \frac{dc_j(t)^*}{dt} + \frac{dc_i(t)}{dt} c_j(t)^* \quad (2.25)$$

$$= i \sum_k c_i(t) c_k(t)^* \langle k|H(t)|j \rangle - i \sum_k \langle i|H(t)|k \rangle c_k(t) c_j(t)^* \quad (2.26)$$

Again, using the definition of the density operator in Eq. (2.13) and the completeness theorem described by Eq. (2.16):

$$\begin{aligned} \frac{d\sigma_{ij}(t)}{dt} &= i \sum_k \langle i|\sigma(t)|k \rangle \langle k|H(t)|j \rangle - i \sum_k \langle i|H(t)|k \rangle \langle k|\sigma(t)|j \rangle \\ &= i \langle i|\sigma(t) H(t)|j \rangle - i \langle i|H(t) \sigma(t)|j \rangle \\ &= i \langle i|(\sigma(t) H(t) - H(t) \sigma(t))|j \rangle , \end{aligned} \quad (2.27)$$

Hence, the Liouville-von Neumann equation can be given by:

$$\frac{d}{dt} \sigma(t) = -i[H(t), \sigma(t)] , \quad (2.28)$$

where  $H(t)$  is the time-dependent Hamiltonian for the system. For a time-dependent  $H(t)$ , Eq. (2.28) has the solution:

$$\sigma(t) = U(t) \sigma(0) U(t)^{-1} , \quad (2.29)$$

where:

$$U(t) = \exp\{-iHt\}, \quad (2.30)$$

$\sigma(t)$  is the density operator at time  $t$  and  $\sigma(0)$  is the density operator at time zero.

### 2.2.3 Operator formalisms

Calculating the time-evolution density operator for a spin system with  $n$  eigenstates will require the use of  $n \times n$  matrices to describe both the Hamiltonian and the density matrix. Such calculations are very tedious and can be more easily expressed by replacing matrix calculations with an expansion of the density operator into a complete set of base operators,  $B_i$ :

$$\sigma(t) = \sum_i b_i(t) B_i, \quad (2.31)$$

By deriving rules to describe the transformations of  $B_i$  under a pulse or a resonance offset frequency, density operator calculations can become much simpler. In this thesis two basis sets are going to be used: the product operator [2.7] and the tensor operator basis sets [2.8].

*The product operators:* This method [2.7] is a purely quantum-mechanical method that yields exact solutions for the outcome of a multiple-pulse NMR experiment. Product operators are most conveniently used when dealing with spin  $I = 1/2$  nuclei; however, a

selective pulse on the central transition (CT), ( $m = +1/2 \leftrightarrow -1/2$ , refer to Fig. 2.1) of a quadrupolar nucleus can create a pseudo-spin-1/2 system that is suitable for product operator treatment as well.

A description of a NMR experiment using product operators utilizes a few simple rules. A spin system consisting of just one spin with  $I = 1/2$  can be described by four operators:

$$\frac{1}{2}E, I_x, I_y, \text{ and } I_z. \quad (2.32)$$

where  $\frac{1}{2}E$  is half the identity operator while the other three Cartesian spin angular momentum operators correspond to the  $x$ -,  $y$ -, and  $z$ -magnetization of the spin. Evolution of the operator  $I_x$  as a result of the offset frequency  $\Omega$  is given by:

$$\sigma(t) = \exp(-iHt) \sigma(0) \exp(+iHt) \quad (2.33)$$

where:

$$\sigma(0) = I_x \quad (2.34)$$

$$H = \Omega I_z \quad (2.35)$$

Substituting Eqns. (2.34) and (2.35) in Eqn. (2.33):

$$\sigma(t) = I_x \cos \Omega t + I_y \sin \Omega t \quad (2.36)$$

Similarly, evolution of the operator  $I_z$  as a result of a radiofrequency pulse of flip angle  $\beta$  applied along the  $x$ -axis of the rotating frame is given by:

$$\begin{aligned}\sigma(t) &= \exp(-i\beta I_x) I_z \exp(+i\beta I_x) \\ &= I_z \cos\beta - I_y \sin\beta\end{aligned}\tag{2.37}$$

where:

$$\beta = \omega_1 t\tag{2.38}$$

Finally, evolution of the operator  $I_x$  as a result of a weak scalar coupling (discussed in Section 2.5.2) of magnitude  $J$  to another spin  $S$  is given by:

$$\begin{aligned}\sigma(t) &= \exp(-i\theta 2I_z S_z) I_x \exp(+i\theta 2I_z S_z) \\ &= I_x \cos\theta + 2I_y S_z \sin\theta\end{aligned}\tag{2.39}$$

where:

$$\theta = \pi J t\tag{2.40}$$

The product operator formalism loses its appeal as one tries to use it to describe NMR experiments involving spins other than  $I = 1/2$ . Although the effect of pulses remains easy to describe, the evolution under other interactions becomes progressively more cumbersome and complicated as the spin number increases. In addition, the ability to use this method to visualize what is happening to the spins, is lost.

*Irreducible tensor operators:* The tensor operator method [2.8] is another approach to study the effect of pulses and free-precession intervals. This method is particularly useful when dealing with quadrupolar nuclei as each basis operator corresponds to a particular

coherence order. The matrix form of the irreducible spherical tensor operators that will be used to describe spin  $I = 1$  nuclei are given in Appendix B.

The density operator for a single spin with spin quantum number  $I$  can be written:

$$\sigma(t) = \sum_{l=0}^{2I} \sum_{p=-l}^{-l} d_{l,p}(t) T_{l,p} , \quad (2.41)$$

where  $T_{l,p}$  is an irreducible spherical tensor operator with rank  $l$  and coherence order  $p$ . The rank of a tensor is the degree of spin order it represents, and takes values from 0 to  $2I$ . A tensor of rank  $l$  can only take  $p$  values of  $-l$  to  $l$ . When  $p=0$ ,  $p=\pm 1$  and  $p=\pm 2$ , the tensor represents populations, single-quantum coherences, and double-quantum coherences, respectively. A single-quantum in-phase coherence is represented by a first-rank tensor, while the antiphase coherence is represented by a second-rank tensor.

The transformations under radiofrequency pulses can be written as:

$$T_{l,p} \xrightarrow{\beta, \phi} \sum_{p'=-l}^l d_{p',p}^l(\beta) \exp\{-i\phi(p'-p)\} T_{l,p'} , \quad (2.42)$$

The coefficients  $d_{p',p}^l(\beta)$  are the reduced Wigner rotation matrix elements that describe the change of coherence order from  $p$  to  $p'$ .  $\beta$  is the flip angle and  $\phi$  is the phase of the applied pulse. Reduced rotation matrix elements

are defined in such a way that a  $+x$  pulse corresponds to  $\phi = 270^\circ$  and a  $+y$  pulse to  $\phi = 0^\circ$ .

During a free-precession period, the tensor operator is transformed as the magnetization evolves under both the quadrupolar interaction,  $\omega_Q$ , and the resonance offset,  $\Omega$ :

$$T_{l,p} \xrightarrow{\omega_Q t} \sum_{l'} c_{l',l}^p(t) T_{l',p} , \quad (2.43)$$

$$T_{l,p} \xrightarrow{\Omega t} \exp\{-ip\Omega t\} T_{l,p} . \quad (2.44)$$

where  $c_{l',l}^p(t)$  are coefficients describing the evolution of the magnetization and  $t$  is the duration of the free precession period. For a spin  $I = 1$ , the nonzero  $c_{l',l}^p(t)$  coefficients are:

$$c_{1,1}^{-1}(t) = c_{1,1}^1(t) = c_{2,2}^{-1}(t) = c_{2,2}^1(t) = \cos \omega_Q t , \quad (2.45)$$

$$c_{2,1}^{-1}(t) = c_{1,2}^{-1}(t) = -c_{2,1}^1(t) = c_{1,2}^1(t) = i \sin \omega_Q t . \quad (2.46)$$

Tensor operators will be used in the coming chapters to describe NMR experiments used to detect  $^2\text{H}$  nuclei.

#### 2.2.4 The Liouville formalism

As an alternative to the operator formalism, the Liouville operator space can be used. This can be easily described if superoperators are used to define the operator relations in the Liouville space. An example of such

and operator relation is the commutator in the Liouville-von Neumann equation (Eq. (2.28)):

$$[H, \sigma] = H\sigma - \sigma H, \quad (2.47)$$

which can be written in superoperator form:

$$H\sigma \equiv [H, \sigma]. \quad (2.48)$$

The matrix representation of a superoperator has  $n^4$  elements ( $n^2 \times n^2$  matrix), hence to be able to multiply  $H$  by  $\sigma$ ,  $\sigma$  must be arranged as a column vector of length  $n^2$ . The Liouville-von Neumann equation can hence be written as:

$$\frac{d}{dt}\sigma(t) = -iH\sigma, \quad (2.49)$$

and solved:

$$\sigma(t) = \exp(-Ht) \sigma(0). \quad (2.50)$$

It follows that by rewriting Eq. (2.50) in terms of the Liouville superoperator,  $L$ :

$$\sigma(t) = \exp(-Lt) \sigma(0), \quad (2.51)$$

terms for relaxation,  $R$ , and exchange,  $K$ , can be also taken into account:

$$L = -iH + R + K. \quad (2.52)$$

## 2.3 The Nuclear Spin Hamiltonian

### 2.3.1 Introduction

Anisotropic spin interactions in powdered materials can broaden, shift and/or split observed NMR resonances. Modern solid-state NMR techniques, however, not only produce spectra with a resolution close to that of liquid-state spectra, but they also take advantage of the anisotropic interactions to yield quantitative information about structure and dynamics that would otherwise be lost in a liquid-state NMR spectrum.

A second-rank Cartesian tensor,  $\mathbf{A}$ , can be used to describe most interactions present in solid materials when exposed to a magnetic field, using Cartesian coordinates  $x$ ,  $y$  and  $z$  to describe the laboratory frame. In general, the Hamiltonian for a specific interaction,  $H_{\text{int}}$ , can be given by:

$$H_{\text{int}} = \mathbf{I} \cdot \mathbf{A} \cdot \mathbf{X} = (I_x, I_y, I_z) \begin{pmatrix} A_{x,x} & A_{x,y} & A_{x,z} \\ A_{y,x} & A_{y,y} & A_{y,z} \\ A_{z,x} & A_{z,y} & A_{z,z} \end{pmatrix} \begin{pmatrix} X_x \\ X_y \\ X_z \end{pmatrix}, \quad (2.53)$$

where  $\mathbf{X}$  is either another spin angular momentum operator or the magnetic field.

It is possible, and usually more convenient, to define the interaction tensor such that it is represented by a diagonal  $3 \times 3$  matrix. This corresponds to a new axis frame, which is called the principal axis

system, PAS. Unlike the laboratory frame, which is fixed in space, the PAS follows the rotations of the nucleus and hence its orientation depends on the local environment of the nucleus.

### 2.3.2 Free precession

The free precession Hamiltonian is the Zeeman Hamiltonian (Eq. (2.20) defined in the rotating frame:

$$H_Z = \Omega I_z . \quad (2.54)$$

The offset  $\Omega$ , rather than the Larmor frequency  $\omega_0$ , is used in the rotating frame. Solving the time-dependent Schrödinger equation (Eq. 2.21) yields the same result as that obtained using the vector model for free precession in the rotating frame:

$$\langle I_x \rangle = \frac{1}{2} \cos \Omega t , \quad (2.55)$$

$$\langle I_y \rangle = \frac{1}{2} \sin \Omega t , \quad (2.56)$$

$$\langle I_z \rangle = 0 . \quad (2.57)$$

The  $x$ - and  $y$ -magnetizations oscillate at the offset frequency while the  $z$ -magnetization remains the same.

### 2.3.3 Radiofrequency pulses

The Hamiltonian,  $H_p$ , that describes the effect of a on-resonance radiofrequency pulse in the rotating frame is given by:

$$H_p = \omega_1 I_x . \quad (2.58)$$

As in to the case of free precession, the time-dependent Schrödinger equation can be solved. The expectation values of the angular momentum operators are found to be:

$$\langle I_x \rangle = 0 , \quad (2.59)$$

$$\langle I_y \rangle = -\frac{1}{2} \sin \omega_1 t , \quad (2.60)$$

$$\langle I_z \rangle = \frac{1}{2} \cos \omega_1 t . \quad (2.61)$$

As shown previously using the vector model, the magnetization starting along the  $z$ -axis rotates at a frequency  $\omega_1$  around the  $x$ -axis towards the  $-y$ -axis.

It is fairly easy to solve the time-dependent Schrödinger equation for the simple examples discussed in this section; however, it can get very laborious when dealing with complex NMR experiments such as those discussed in this thesis. For this reason, the more compact and convenient operator formalisms introduced in Section 2.2.3 are normally used.

## 2.4 Shielding and Chemical shift

The electrons surrounding the nuclei in a magnetic field produce a secondary field, which will result in the nucleus experiencing an

additional magnetic field. Information about the energy of the system can be obtained by defining the Hamiltonian for this interaction:

$$\begin{aligned} H &= \gamma I \cdot (1 - \sigma) \cdot \mathbf{B}_0 \\ &= H_z + H_\sigma, \end{aligned} \tag{2.62}$$

so:

$$H_\sigma = \gamma I \cdot \sigma \cdot \mathbf{B}_0 \tag{2.63}$$

where  $\mathbf{B}_0$  is the applied magnetic field at a nucleus with a shielding tensor,  $\sigma$  in the laboratory frame. The shielding tensor  $\sigma$ , takes into account the difference in magnetic field a bare nucleus would experience and can be represented by a  $3 \times 3$  matrix [2.9], hence  $\mathbf{B}_{\text{loc}}$  can be given by:

$$\begin{aligned} \mathbf{B}_{\text{loc}} &= \sigma \cdot \mathbf{B}_0 \\ &= \begin{pmatrix} \sigma_{xx} & \sigma_{xy} & \sigma_{xz} \\ \sigma_{yx} & \sigma_{yy} & \sigma_{yz} \\ \sigma_{zx} & \sigma_{zy} & \sigma_{zz} \end{pmatrix} \cdot \begin{pmatrix} 0 \\ 0 \\ B_0 \end{pmatrix} \\ &= \begin{pmatrix} \sigma_{xz} B_0 \\ \sigma_{yz} B_0 \\ \sigma_{zz} B_0 \end{pmatrix}, \end{aligned} \tag{2.64}$$

given that the applied field  $B_0$  in the laboratory frame is aligned along the z-axis. Thus, if the secular approximation is made, i.e., if only the terms in the Hamiltonian that affect the energy of the system but not the wavefunction are retained, Eq. (2.63) can be given by [2.10]:

$$H_\sigma = \gamma \sigma_{zz} B_0 I_z. \tag{2.65}$$

It is convenient to use  $\sigma$  in the PAS frame and therefore define it as a diagonalized matrix with  $\sigma_{XX}$ ,  $\sigma_{YY}$  and  $\sigma_{ZZ}$  as its diagonal elements, also called principal values (note that the subscripts of these diagonal elements are written in capital letters to distinguish between the laboratory frame and PAS). In solid-state NMR, both the isotropic,  $\sigma$ , and anisotropic,  $\Delta$ , components of the shielding tensor are present and these can be defined in terms of the principal values of  $\sigma$  in the PAS:

$$\sigma_{\text{iso}} = \frac{1}{3}(\sigma_{XX} + \sigma_{YY} + \sigma_{ZZ}), \quad (2.66)$$

$$\Delta = \sigma_{ZZ} - \sigma_{\text{iso}}. \quad (2.67)$$

The chemical shift,  $\delta$ , is a much more convenient parameter to measure than the shielding parameter. It is usually given relative to a reference resonance frequency,  $\omega_{\text{ref}}$ :

$$\delta = \frac{(\omega - \omega_{\text{ref}})}{\omega_{\text{ref}}}, \quad (2.68)$$

where  $\omega$  is the frequency of the nucleus of interest given by:

$$\omega = \gamma(1 - \sigma_{\text{iso}})B_0. \quad (2.69)$$

Thus:

$$\delta_{\text{iso}} \approx \sigma_{\text{iso}}^{\text{ref}} - \sigma_{\text{iso}}. \quad (2.70)$$

As with the shielding tensor, the chemical shift also has an anisotropic component, which is known as chemical shift anisotropy (CSA) and can

be described in the same manner as it was described for the shielding anisotropic component:

$$\Delta = \delta_{ZZ} - \delta_{iso} . \quad (2.71)$$

Most of the experiments discussed in this thesis will deal with quadrupolar nuclei in powdered solids investigated under magic-angle spinning (MAS) conditions. This means that apart from the fact that the CSA will always be much smaller than the quadrupolar interaction, MAS refocuses the CSA over the course of a rotor period; hence, the effect it would have on the acquired spectrum is suppressed.

## 2.5 Spin-Spin Coupling: Dipolar and Scalar Interactions

### 2.5.1 Introduction

There are two primary mechanisms by which one nuclear magnetic moment may interact with another: the direct dipolar or dipole-dipole interaction and the indirect spin-spin interaction also known as  $J$  coupling. The dipolar coupling describes the direct through-space interaction between two NMR-active nuclear spins, where its magnitude is directly proportional to the inverse cube ( $1/r^3$ ) of the separation between the two spins. On the other hand,  $J$  coupling takes place through the electrons making up the chemical bond, hence making it a through-bond interaction. Consequently, its magnitude,  $J$ , does not simply depend

on distance; it depends greatly on the electronic structure of a molecule. In addition,  $J$  coupling is not restricted to nuclei coupled by a single bond, it can also occur between nuclei separated by two bonds or more, for example  $J$  coupling between two protons separated by a carbon (i.e., H-C-H). A two-bond interaction between two different nuclei, as found in an Al-O-P bond, is what allows the acquisition of  $J$ -correlation experiments such as the heteronuclear correlation ( $J$ -HETCOR) experiment that will be discussed in more detail in Chapter 6. In this case, polarization transfer from  $^{27}\text{Al}$  to  $^{31}\text{P}$  nuclei via a two-bond  $J$  coupling is used to obtain information about the structure and framework of an Al-O-P network structure.

### 2.5.2 Dipolar coupling

The dipolar interaction is described by a traceless rank two tensor, as the sum of the diagonal elements of its matrix is zero. Therefore, in solution, dipolar interactions are averaged to their isotropic values due to rapid tumbling of the molecules, while in solids the strength of this interaction is proportional to  $1/r^3$  and the orientation of the crystallite relative to the applied magnetic field,  $B_0$ . However, by rapidly spinning the powdered sample at an angle of  $54.74^\circ$  with respect to  $B_0$ , broadening due to anisotropic chemical shielding and direct dipolar interactions can be largely removed.

Classically, the energy of the interaction of two dipoles can be written in terms of the magnetic moments  $\mu_I$  and  $\mu_S$ , and the distance  $r$ :

$$E_D = \frac{\mu_0}{4\pi} \left( \frac{\boldsymbol{\mu}_I \cdot \boldsymbol{\mu}_S}{r^3} - 3 \frac{(\boldsymbol{\mu}_I \cdot \mathbf{r})(\boldsymbol{\mu}_S \cdot \mathbf{r})}{r^5} \right), \quad (2.72)$$

where  $\mu_0$  is the permeability of free space,  $4\pi \times 10^7 \text{ NA}^{-2}$ . If the two dipoles have the same orientation with respect to  $r$ , then Eq. (2.72) becomes:

$$E_D = \frac{\mu_0}{4\pi} \frac{\boldsymbol{\mu}_I \cdot \boldsymbol{\mu}_S}{r^3} (1 - 3 \cos^2 \theta), \quad (2.73)$$

where  $\theta$  is the angle between the direction of the two  $\boldsymbol{\mu}_I$  and  $\boldsymbol{\mu}_S$ , and the vector  $r$  which separates them. Recalling Eq. (2.4) and combining Eqs. (2.72) and (2.73), the dipolar coupling Hamiltonian in the PAS,  $H_D^{\text{PAS}}$ , between two spins  $I$  and  $S$  is obtained:

$$H_D^{\text{PAS}} = -\gamma_I \gamma_S \hbar \left( \frac{\mathbf{I} \cdot \mathbf{S}}{r^3} - 3 \frac{(\mathbf{I} \cdot \mathbf{r})(\mathbf{S} \cdot \mathbf{r})}{r^5} \right) \frac{\mu_0}{4\pi}, \quad (2.74)$$

which after expansion of the spherical tensors and reorientation into the laboratory frame, can be written as:

$$\begin{aligned} H_D = -d & \left[ (3 \cos^2 \theta - 1) \left[ I_z S_z - \frac{1}{2} I_+ S_- + I_- S_+ \right] \right. \\ & + \frac{3}{4} \sin 2\theta \left[ (I_z S_+ + I_+ S_z) \sin \theta \cos \theta \exp(+i\phi) \right] \\ & \left. + \frac{3}{4} \sin^2 \theta \left[ I_+ S_+ \exp(+i2\phi) + I_- S_- \exp(+i2\phi) \right] \right]. \end{aligned} \quad (2.75)$$

where  $d$  is the dipolar coupling constant measured in  $\text{rad s}^{-1}$ :

$$d = \frac{\gamma_I \gamma_S \hbar \mu_0}{r^3 4\pi}. \quad (2.76)$$

Here,  $I_{\pm} = I_x \pm iI_y$  where  $I_+$ ,  $S_+$  and  $I_-$ ,  $S_-$  are the raising and lowering operators, respectively, acting on spins  $I$  and  $S$ .

To determine fully the dipolar interaction of the system, each dipolar Hamiltonian of every pair of nuclei needs to be taken into account. Considering two spin  $I = 1/2$  nuclei  $I$  and  $S$ , the total Hamiltonian of the system is:

$$H = H_Z^I + H_Z^S + H_D^{IS}, \quad (2.77)$$

where:

$$H_Z^I + H_Z^S = \frac{1}{2} \begin{pmatrix} \omega_0^I + \omega_0^S & 0 & 0 & 0 \\ 0 & \omega_0^I - \omega_0^S & 0 & 0 \\ 0 & 0 & -\omega_0^I + \omega_0^S & 0 \\ 0 & 0 & 0 & -\omega_0^I - \omega_0^S \end{pmatrix}, \quad (2.78)$$

Since the Zeeman Hamiltonian is always much greater than the spin-spin interactions, the non-secular terms that do not commute with the Zeeman Hamiltonian may be discarded [2.11]. The simplified homonuclear,  $H_D^{\text{homo}}$ , can be given by:

$$H_D^{\text{homo}} = -d(3\cos^2\theta - 1) \left[ I_z S_z - \frac{1}{2} I_+ S_- + I_- S_+ \right] \quad (2.79)$$

$$= \frac{1}{2} \begin{pmatrix} d & 0 & 0 & 0 \\ 0 & -d & -d & 0 \\ 0 & -d & -d & 0 \\ 0 & 0 & 0 & d \end{pmatrix},$$

Homonuclear dipolar coupling is the result of an interaction between identical nuclides, i.e.,  $\omega_0^I = \omega_0^S$ . On the other hand, if the interaction is between two different nuclides, heteronuclear dipolar coupling, the difference in their Larmor frequencies is likely to be much greater than the dipolar coupling between them, then  $\omega_0^I - \omega_0^S \gg d$ . In this case, the shift in energy of the spin eigenstates can be treated as a perturbation of the Zeeman splitting. Hence the heteronuclear Hamiltonian,  $H_D^{\text{hetero}}$ , is simply given by:

$$H_D^{\text{hetero}} = -d(3\cos^2\theta - 1)I_z S_z . \quad (2.80)$$

A very important phenomenon that is mediated by direct spin-spin interactions is 'spin diffusion'. Spin diffusion is a mechanism by which spin order at a location in a material is transported to other locations. In general terms, spin diffusion occurs via the  $I_+ S_- + I_- S_+$  or 'flip-flop' transitions in the dipole-dipole coupling Hamiltonian (Eq. (2.79)). This is only allowed when the transition is energy conserving, hence radiationless.

In solids, this phenomenon was first observed by Bloembergen [2.12] while investigating spin-lattice relaxation in crystalline materials doped with paramagnetic impurities. Dipolar coupling between the paramagnetic centre and the electronic spin leads to spin-lattice relaxation,  $T_1$ , with a rate given by:

$$\frac{1}{T_1(r)} = \frac{C}{r^6} , \quad (2.81)$$

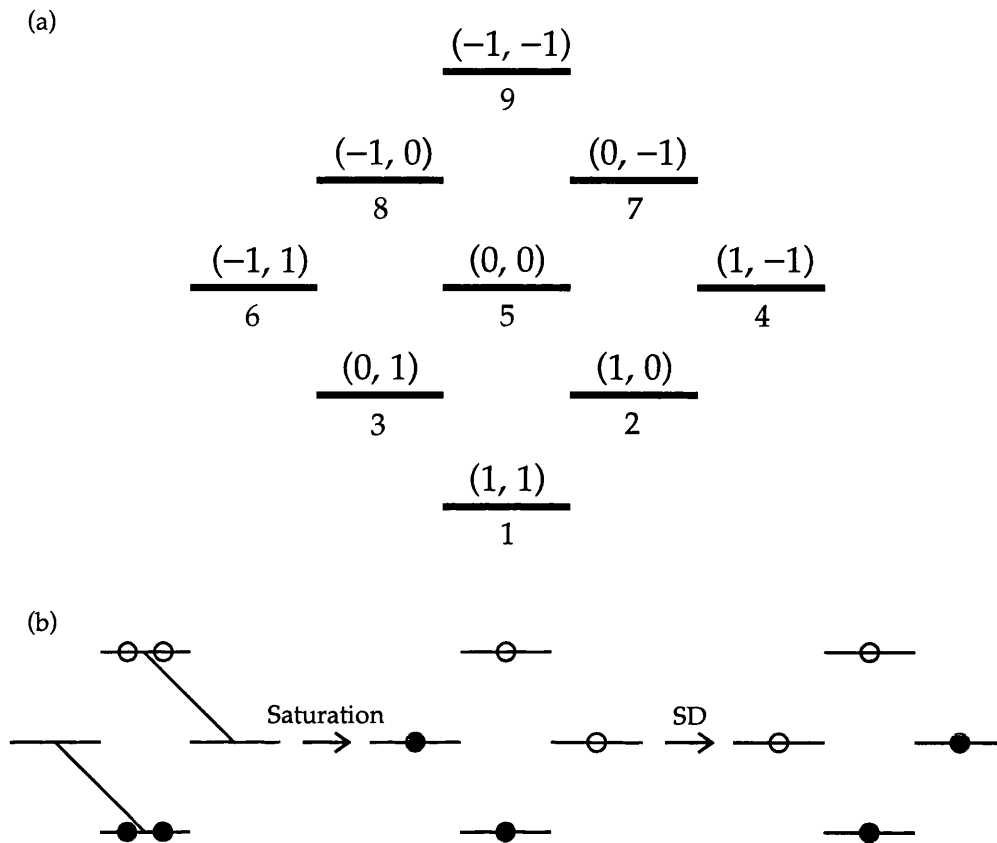


Figure 2.7: (a) Energy-level diagram for a two dipolar-coupled spin  $I = S = 1$ . (b) Any four of the energy levels in (a) showing the population state after saturation and then after spin diffusion (SD), where the filled and unfilled circles represent an excess and deficit of population, respectively.

where  $C$  is a constant. However, the  $T_1$  value calculated using the above equation, was far longer than that found by experiment. It was explained that only spin diffusion could have transported the magnetization to the vicinity of the paramagnetic site making the whole system relax faster than predicted.

Since this first observation, spin diffusion has played an extensive part in the NMR of solid materials and will be used to explain the phenomenon observed in Chapter 5, where discrepancies in  $T_1$  times of

deuterated solids are discussed. Spin diffusion in deuterated systems has been discussed by Alla *et al.* [2.13], Suter *et al.* [2.14] and Gan *et al.* [2.15]. Figure 2.7a shows the energy-level diagram for a pair of homonuclear dipolar-coupled spins  $I = S = 1$ , where  $\omega_0^I = \omega_0^S$ . Figure 2.7b represents any four energy levels shown in Fig. 2.7a, which are populated according to the Boltzmann distribution. Saturation equalizes the populations, which allows for spin diffusion to occur. After spin diffusion, the spin populations of the degenerate levels have exchanged spontaneously via an energy-conserving transition as shown. Spin diffusion is a two-way process; therefore the reverse process will also take place.

### 2.5.3 Scalar ( $J$ ) coupling

Indirect spin-spin coupling, also known as  $J$  coupling, is mediated by chemical bonds and is very useful when determining framework topology of materials. In Section 2.5.2, it was shown that the dipolar interaction is averaged in liquids, hence no broadening is observed. However, the  $J$  coupling tensor is not traceless, hence, even in solution,  $J$  coupling is observed as its isotropic component cannot be averaged away. This results in NMR spectra containing complicated multiplet patterns. The Hamiltonian describing scalar coupling of the spins  $I$  and  $S$  in the laboratory frame is given by [2.16]:

$$\begin{aligned}
H_J^{IS} = & 2\pi J_{IS} \mathbf{I} \cdot \mathbf{S} + 4\pi \frac{\Delta J_{IS}}{3} \left[ \frac{1}{2} (3 \cos^2 \theta - 1) \left[ 3I_z S_z - \frac{1}{2} \mathbf{I} \cdot \mathbf{S} \right] \right] \\
& + \frac{3}{4} \sin 2\theta \left[ (I_z S_+ - I_+ S_z) \exp(-i\phi) + (I_z S_- - I_- S_z) \exp(+i\phi) \right] \\
& + \frac{3}{4} \sin^2 \theta \left[ I_+ S_+ \exp(-i2\phi) + I_- S_- \exp(+i2\phi) \right].
\end{aligned} \tag{2.82}$$

Equation (2.82) shows the tensor described as the sum of an isotropic component,  $J_{IS}$ , and an anisotropic component,  $\Delta J_{IS}$ . The latter however, can be ignored, especially under magic angle spinning conditions, due to its second-rank orientational dependence of its diagonal matrix elements.

Hence,  $H_J^{IS}$  is normally written in its simplified form:

$$H_J^{IS} = 2\pi J_{IS} \mathbf{I} \cdot \mathbf{S} . \tag{2.83}$$

$\mathbf{I} \cdot \mathbf{S}$  can be expanded as the sum of three terms and, consequently, the scalar coupling Hamiltonian,  $H_J^{IS}$ , can be written in matrix form as follows:

$$\begin{aligned}
H_J^{IS} = & 2\pi J_{IS} (\mathbf{I}_x \mathbf{S}_x + \mathbf{I}_y \mathbf{S}_y + \mathbf{I}_z \mathbf{S}_z) \\
= & 2\pi J_{IS} \begin{pmatrix} \frac{1}{4} & 0 & 0 & 0 \\ 0 & -\frac{1}{4} & \frac{1}{2} & 0 \\ 0 & \frac{1}{2} & -\frac{1}{4} & 0 \\ 0 & 0 & 0 & \frac{1}{4} \end{pmatrix} .
\end{aligned} \tag{2.84}$$

In recent years,  $J$  coupling has become of greater interest to solid-state NMR. Previously  $J$  couplings were rarely used in solids as they were always overpowered by the non-averaged dipolar couplings and chemical shift anisotropies present. However, important advances have been made in this area and, as a result, information obtained from  $J$

coupled nuclei is being used to shed light on through-bond connectivities in both organic and inorganic solids.

Most studies use  $J$  couplings to transfer coherences between nuclei and generate homonuclear or heteronuclear through-bond correlations [2.17–2.26]. In the last chapter of this thesis,  $J$  coupling will be used to investigate the framework topography of aluminophosphates, by using the heteronuclear scalar couplings present between  $^{27}\text{Al}$  and  $^{31}\text{P}$ . Polarization transfer between heteronuclei was achieved by using the INEPT schemes as well as the HMQC experiment, which will be discussed in detail in Chapter 6.

## 2.6 Quadrupolar Interaction

### 2.6.1 Introduction

About 75% of all NMR-active nuclei have  $I > 1/2$ . In addition to interacting with the applied and local magnetic fields, as all spin  $I = 1/2$  nuclei do, these nuclei also possess an electric quadrupole moment,  $eQ$ , which interacts with the electric field gradient (EFG) tensor  $V$ . The quadrupolar Hamiltonian,  $H_Q$ , can be written as follows [2.27]:

$$H_Q = I \cdot Q \cdot I, \quad (2.85)$$

where:

$$\mathbf{Q} = \frac{eQ}{2I(2I-1)\hbar} \mathbf{V}. \quad (2.86)$$

$e$  is the magnitude of the electron charge,  $I$  is the nuclear spin angular momentum vector and  $Q$  is the nuclear electric quadrupole moment. Parameters often used when describing a quadrupolar nucleus are the quadrupolar coupling constant,  $C_Q$ , and the quadrupolar asymmetry parameter,  $\eta_Q$ :

$$C_Q = \frac{e^2qQ}{h}, \quad (2.87)$$

$$\eta_Q = \frac{V_{XX} - V_{YY}}{V_{ZZ}}, \quad (2.88)$$

where  $eq = V_{zz}$  and  $V_{\alpha\alpha}$  ( $\alpha\alpha = XX$  or  $YY$  or  $ZZ$ ) are the principal values of  $\mathbf{V}$ . By convention:

$$|V_{ZZ}| \geq |V_{YY}| \geq |V_{XX}|, \quad (2.89)$$

while:

$$V_{XX} + V_{YY} + V_{ZZ} = 0, \quad (2.90)$$

meaning that the EFG tensor is traceless. The quadrupolar Hamiltonian in the PAS,  $H_Q^{\text{PAS}}$ , can be expressed as:

$$H_Q^{\text{PAS}} = \omega_Q^{\text{PAS}} \left[ I_Z^2 - \frac{1}{3}I(I+1) + \frac{1}{6}\eta_Q(I_X^2 - I_Y^2) \right], \quad (2.91)$$

or in matrix and spherical tensor form for a spin  $I = 3/2$ :

$$\begin{aligned}
H_Q^{\text{PAS}} &= \omega_Q^{\text{PAS}} \begin{pmatrix} 1 & 0 & \frac{\eta}{\sqrt{3}} & 0 \\ 0 & -1 & 0 & \frac{\eta}{\sqrt{3}} \\ \frac{\eta}{\sqrt{3}} & 0 & -1 & 0 \\ 0 & \frac{\eta}{\sqrt{3}} & 0 & 1 \end{pmatrix} \\
&= 2\omega_Q^{\text{PAS}} \left[ T_{2,0} + \frac{\eta}{\sqrt{6}} (T_{2,2} + T_{2,-2}) \right],
\end{aligned} \tag{2.92}$$

where:

$$\omega_Q^{\text{PAS}} = \frac{3\pi C_Q}{2I(2I-1)}, \tag{2.93}$$

and  $T_{l,p}$  are spherical tensor operators (discussed in Section 2.2.3). The matrix form of the irreducible spherical tensor operators that will be used to describe spin  $I = 1$  nuclei are given in Appendix B. Like all the other interactions discussed in this chapter, the quadrupolar interaction is often small compared to the Zeeman interaction and can be viewed as a perturbation of the latter.

Consider the sum of the Zeeman Hamiltonian,  $H_z$  and the quadrupolar Hamiltonian,  $H_Q$ . Since  $H_z$  always dominates  $H_Q$  and the eigenstates,  $|i\rangle$ , and the energies  $E_i^0$ , of  $H_z$  are known:

$$H_z |i\rangle = E_i^0 |i\rangle, \tag{2.94}$$

then time-independent perturbation theory can be applied. The energy of an individual state,  $E_i$ , is given as:

$$E_i = E_i^0 + E_i^1 + E_i^2 + E_i^3 + \dots , \quad (2.95)$$

where  $E_i^0$  is the energy arising from the Zeeman interaction and  $E_i^n$  are the first-, second-, third-order, and so on, corrections due to the quadrupolar interaction,  $H_z$  given by:

$$E_i^1 = \langle i | H_z | i \rangle , \quad (2.96)$$

$$E_i^2 = \sum_{j \neq i} \frac{\langle i | H_z | j \rangle \langle j | H_z | i \rangle}{E_i^0 - E_j^0} . \quad (2.97)$$

Second-order and larger corrections need only be taken into account if the quadrupolar interaction is large; otherwise the first-order, or secular, approximation would be sufficient. The perturbation manifests itself in a shift in frequency of the original  $2I$  transitions of the Zeeman energy levels discussed in Section 2.1.1.

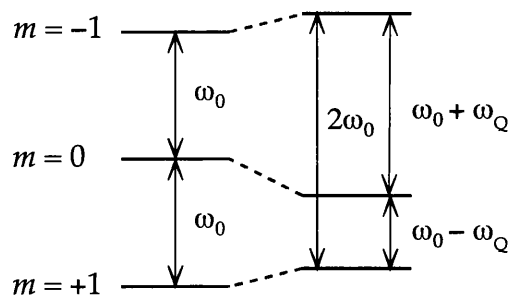
### 2.6.2 First-order quadrupolar broadening for spin $I = 1$ nuclei

The Hamiltonian for this perturbation in the laboratory frame is given by:

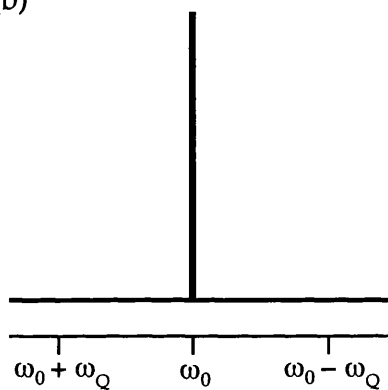
$$H_Q = \omega_Q^{\text{PAS}} \left[ D_{0,0}^2(\alpha, \beta, \gamma) + \frac{\eta_Q}{\sqrt{6}} \{ D_{0,2}^2(\alpha, \beta, \gamma) + D_{0,-2}^2(\alpha, \beta, \gamma) \} \right] T_{2,0} , \quad (2.98)$$

where  $D_{m',m}^l(\alpha, \beta, \gamma)$  are Wigner rotation matrix elements with  $\alpha, \beta$ , and  $\gamma$  being Euler angles describing the transformation from the principal axis system to the laboratory frame and given by [2.28]:

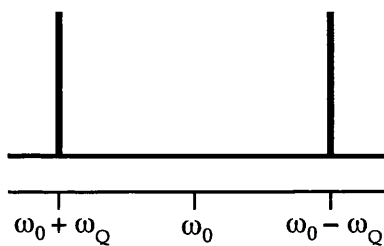
(a)



(b)



(c)



(d)

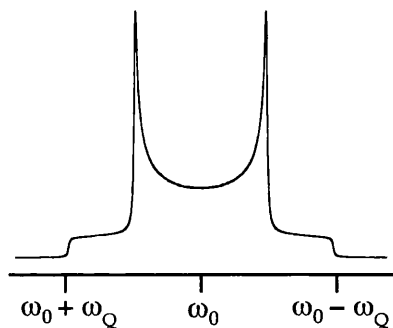


Figure 2.8: (a) First-order perturbation of the Zeeman energy levels of a spin  $I = 1$  nucleus by the quadrupolar interaction. Schematic representation of the resulting spectra (b) without and (c) with first-order quadrupolar interaction. (b) shows one resonance at the Larmor frequency  $\omega_0$  and (c) shows a quadrupolar doublet with splitting  $2\omega_Q$ . (d) Computer-simulated 'Pake doublet' powder lineshape.

$$D_{m',m}^l(\alpha, \beta, \gamma) = \exp\{-im'\alpha\} d_{m',m}^l(\beta) \exp\{-im\gamma\}, \quad (2.99)$$

where  $d_{m',m}^l(\beta)$  are reduced Wigner rotation matrix elements.

Recall Fig. 2.1: the energy level diagram for a spin  $I = 1$  exhibits two allowed transitions with frequency  $\omega_0$ , also known as single-quantum (SQ) transitions. The perturbation of the Zeeman energy levels to a first order approximation, for a spin  $I = 1$  nucleus, splits these transitions by  $2\omega_Q$  where  $\omega_Q$  the quadrupolar splitting parameter corresponds to a particular crystallite orientation and is given by:

$$\omega_Q = \frac{\omega_Q^{\text{PAS}}}{2} (3 \cos^2 \beta - 1 + \eta \sin^2 \beta \cos 2\gamma), \quad (2.100)$$

where the angles  $\beta$  and  $\gamma$  describe the orientation of the PAS of the EFG with respect to  $B_0$ . Figure 2.8a shows the first-order perturbation of the Zeeman energy levels for a spin  $I = 1$ . The transition marked  $2\omega_0$  in Fig. 2.8a, also known as a double-quantum (DQ) transition, is not affected by the quadrupolar interaction to first order. Hence, a single resonance at  $\omega_0$  will be observed while in the absence of the first-order interaction (Fig. 2.8b), when it is present, this resonance will split into two peaks spaced by  $2\omega_Q$  (Fig. 2.8c). However, a powdered or polycrystalline material is composed of many crystallites that may have any orientation with respect to  $B_0$ . Each orientation will produce a different splitting which results in a 'Pake doublet' lineshape as shown in Fig. 2.8d.

2.6.3 *First- and second-order quadrupolar broadenings for half-integer spin nuclei*

For spin  $I = 3/2$ , the first-order quadrupolar corrections to the energies of the Zeeman eigenstates,  $|i\rangle$ , are given by:

$$E_{3/2}^1 = E_{-3/2}^1 = \omega_Q \quad (2.101)$$

$$E_{1/2}^1 = E_{-1/2}^1 = -\omega_Q$$

where  $\omega_Q$  takes the same definition as in Eq. (2.100).

It is essential to consider the second-order contribution if the quadrupolar interaction is large, as the first-order correction will be insufficient to describe the perturbation of the energy levels. For a general energy level energy,  $E_i^2$ , and a nucleus with spin quantum number  $I$  the second-order correction is given by:

$$E_i^2 = E_{-i}^2 = \frac{(\omega_Q^{\text{PAS}})^2}{2\omega_0} \left\{ \begin{array}{l} A^0(I, m)Q^0(\eta_Q) + A^2(I, m)Q^2(\alpha, \beta, \gamma, \eta_Q) \\ + A^4(I, m)Q^4(\alpha, \beta, \gamma, \eta_Q) \end{array} \right\}, \quad (2.102)$$

where  $A^l(I, m)$  are the coefficients of the zeroth- ( $l = 0$ ), second- ( $l = 2$ ) and fourth-rank ( $l = 4$ ) contributions; they are given for nuclei with spin  $I = 3/2$  and  $5/2$  in Table 0.1. The zeroth-, second- and fourth-rank orientational dependent functions,  $Q^n$ , in Eq. (2.102) are given by:

$$Q^0(\eta_Q) = \left( 1 + \frac{\eta_Q^2}{3} \right), \quad (2.103)$$

Table 0.1: Coefficients for zeroth-, second- and fourth-rank Wigner rotation matrix elements in Eq. (2.102) for eigenstates of spin  $I = 3/2$  and  $5/2$  nuclei.

$I$	$m$	$A^0(I, m)$	$A^2(I, m)$	$A^4(I, m)$
3/2	$\pm 1/2$	$-2/5$	$-8/7$	$54/35$
	$\pm 3/2$	$6/5$	$0$	$-6/5$
5/2	$\pm 1/2$	$-16/15$	$-64/21$	$144/35$
	$\pm 3/2$	$-4/5$	$-40/7$	$228/35$
	$\pm 5/2$	$20/3$	$40/21$	$-60/7$

$$Q^2(\alpha, \beta, \gamma, \eta_Q) = \left(1 + \frac{\eta_Q^2}{3}\right) D_{0,0}^2(\alpha, \beta, \gamma) - \frac{\sqrt{2}}{\sqrt{3}} \eta_Q \{D_{0,2}^2(\alpha, \beta, \gamma) + D_{0,-2}^2(\alpha, \beta, \gamma)\}, \quad (2.104)$$

$$Q^4(\alpha, \beta, \gamma, \eta_Q) = \left(1 + \frac{\eta_Q^2}{18}\right) D_{0,0}^4(\alpha, \beta, \gamma) + \frac{\sqrt{10}}{6} \eta_Q \{D_{0,2}^4(\alpha, \beta, \gamma) + D_{0,-2}^4(\alpha, \beta, \gamma)\} + \frac{35}{18\sqrt{70}} \eta_Q^2 \{D_{0,4}^4(\alpha, \beta, \gamma) + D_{0,-4}^4(\alpha, \beta, \gamma)\}. \quad (2.105)$$

Figure 2.9a shows the effect of the first- and second-order quadrupolar interactions on the energy levels of a spin  $I = 3/2$  nucleus. After the first-order correction is made, a distinction between the central transition (CT),  $m = +1/2 \leftrightarrow -1/2$ , with frequency  $\omega_0$  and the two

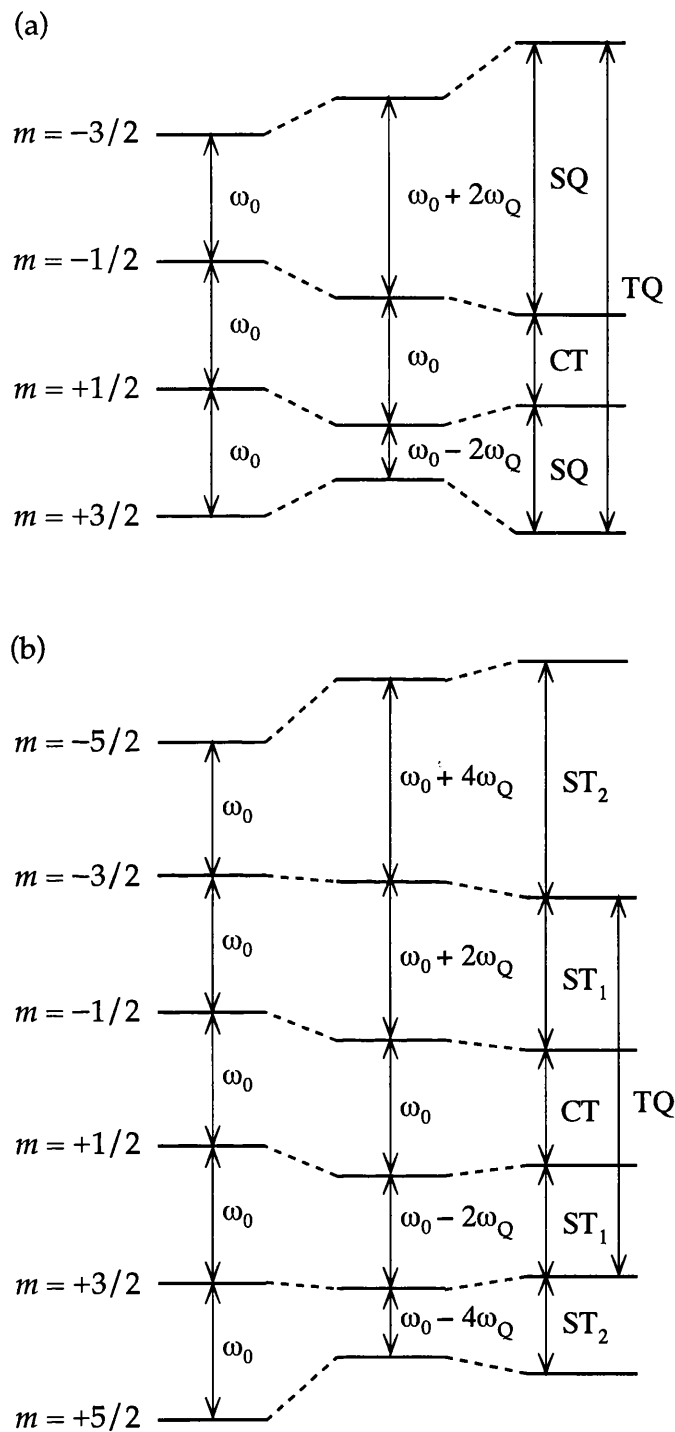


Figure 2.9: First-order and second-order perturbation of the Zeeman energy levels of a spin  $I = 3/2$  and (b)  $I = 5/2$  nucleus by the quadrupolar interaction.

satellite transitions (ST),  $m = \pm 3/2 \leftrightarrow \pm 1/2$ , with frequencies  $\omega_0 + 2\omega_Q$  and  $\omega_0 - 2\omega_Q$  can be observed. Only the satellite transitions are affected by the first-order quadrupolar interaction, while both central and triple-quantum transitions (TQ),  $m = +3/2 \leftrightarrow -3/2$ , are not. This is not true after the second-order perturbation has been taken into account. Equation (2.102) clearly illustrates that all transitions are now affected by the second-order quadrupolar interaction.

Figure 2.9b shows the energy level diagram for a spin  $I = 5/2$  nucleus affected by both first- and second-order quadrupolar

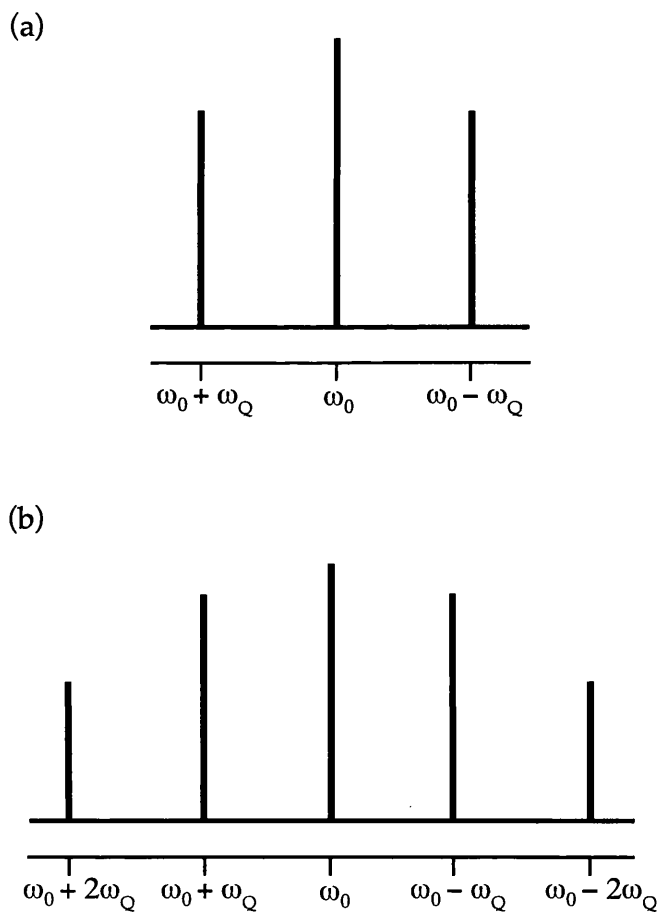


Figure 2.10: Schematic representation of resulting spectra for spin (a)  $I = 3/2$  and  $I = 5/2$  when affected by first-order quadrupolar interaction.

interactions. In addition to what was said about a spin  $I = 3/2$  nucleus, a spin  $I = 5/2$  nucleus also has the outer satellite transitions ( $ST_2$ ),  $m = \pm 5/2 \leftrightarrow \pm 3/2$ . Consequently, the NMR spectrum of a spin  $I = 5/2$  nucleus consists of signal corresponding to the CT, the inner satellite transitions ( $ST_1$ ),  $m = \pm 3/2 \leftrightarrow \pm 1/2$ , and the outer satellite transitions.

Figure 2.10 shows schematic spectra for spin  $I = 3/2$  and spin  $I = 5/2$  respectively, when affected by the first-order quadrupolar interaction, where the resulting peaks for both spins are separated by  $2\omega_Q$ .

---

## Chapter 3

---

# Essential Techniques for Solid-State NMR

---

### 3.1 Introduction

The anisotropic nuclear spin interactions discussed in Chapter 2 result in anisotropically broadened spectra in powdered solids. Consequently, a lot of work has gone into devising and optimizing techniques with the aim of suppressing such broadenings while maintaining high resolution and sensitivity, which is indispensable when studying materials. Consequently, quantitative information from the study of, for example, internal dynamics, spin diffusion, anisotropy, exchange processes etc., is obtained. Some of the techniques that have been developed over the years are going to be discussed here and will be used throughout this thesis.

### 3.2 Coherence Selection

It is important to introduce the concept of coherence selection, before any NMR experiment is described, as it is important due to the

inability of a pulse to discriminate between required and unwanted signal. For example, if one selects a  $90^\circ$  pulse, all possible coherences are generated and hence a very cluttered spectrum will be obtained, hiding the signal that is needed [3.1]. For this reason, in NMR experiments, a coherence transfer pathway always accompanies a pulse sequence, as will be shown throughout this thesis.

In solid-state NMR, the most common way of choosing the required coherences over those unwanted is to use phase cycling [3.2]. This is done as part of the NMR experiment where the phases of the pulses are shifted as the experiment is repeated. When the phase of a pulse is shifted by an angle  $\phi$ , then the coherence that experiences a change in coherence order of  $\Delta p$  experiences a phase shift of:

$$\phi_i = -\phi\Delta p . \quad (3.1)$$

The next step is to set the receiver phase:

$$\phi_R = -\phi\Delta p , \quad (3.2)$$

which ensures that the corresponding pathway is selected. By the end of the phase cycle, all the other coherence pathways will sum up to zero hence only the wanted pathway is observed.

It is also possible to choose more than one coherence pathway at the same time. Consider a phase cycle being shifted by  $360^\circ/N$  where  $N$  is the number of times the pulse phase is changed. Hence as well as  $\Delta p$ ,

$\Delta p \pm nN$  coherence pathways will also be detected, where  $n$  is an integer.

All the other pathways will be suppressed.

### 3.3 Spin-Echo Pulse Sequences

Broad lines are a common feature in NMR spectra of powdered solids. These broad lines are the result of a very rapidly decaying (short) FID. The spectrometer always allows for a short period of time (the 'dead time') between the execution of the pulse and the beginning of acquisition to allow for pulse-ringdown effects to die away. Also during the dead time, transverse magnetization evolves under the spin interactions present, which means that each homogeneous component of the resonance would have built up a frequency-dependent phase by the time the first sampling point is acquired. Hence in addition to looking at a small part of the FID, a large 'first-order' phase correction, i.e., a frequency-dependent linear combination of the real and imaginary components, is needed to correct this phase error. However, this method of correction is only an approximation, and only an echo pulse sequence will provide an undistorted spectrum.

Figure 3.1 shows the pulse sequence for a spin-echo experiment, also known as the Hahn [3.3] or Carr-Purcell (Method A) echo [3.4]. This experiment is considered to be a fundamental NMR experiment, which allows the magnetization to end up along the same axis no matter what

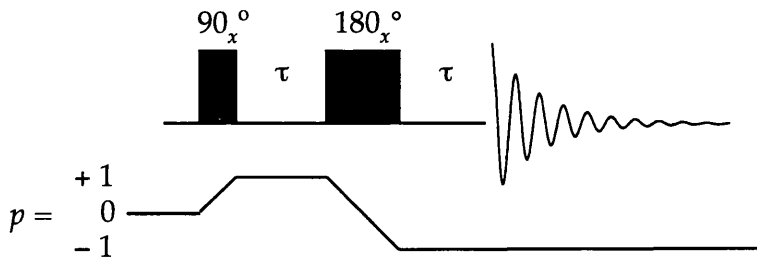


Figure 3.1: Pulse sequence for the spin-echo experiment.

the values of the free precession period,  $\tau$ , and resonance offset,  $\Omega$ , are. Apart from being a very useful experiment, the spin-echo sequence is also widely used as a component of more complex experiments, as will be shown in the following chapters. Starting from magnetization along the  $z$ -axis,  $I_z$ , the product operator calculation using the equations discussed in Section 2.2.3 is:

$$\begin{aligned}
 I_z &\xrightarrow{90_x^\circ} -I_y \\
 &\xrightarrow{\Omega\tau} -I_y \cos \Omega\tau + I_x \sin \Omega\tau \\
 &\xrightarrow{180_y^\circ} -I_y \cos \Omega\tau - I_x \sin \Omega\tau \\
 &\xrightarrow{\Omega\tau} -I_y \cos^2 \Omega\tau + I_x \cos \Omega\tau \sin \Omega\tau - I_x \cos \Omega\tau \sin \Omega\tau - I_y \sin^2 \Omega\tau \\
 &= -I_y .
 \end{aligned} \tag{3.3}$$

The  $90^\circ$  pulse places the magnetization along the  $-y$ -axis, from where it then precesses for a time period  $\tau$  acquiring a phase  $\Omega\tau$ , where  $\Omega$  is the offset frequency. The  $180^\circ$  pulse rotates the magnetization vector by  $180^\circ$  about  $x$ . A second  $\tau$  period allows the magnetization to be refocused along the  $y$ -axis. The  $180^\circ$  pulse is commonly called the 'refocusing pulse' as it causes the evolution during the first free-precession interval to be undone during the second. Looking at the result, it is immediately

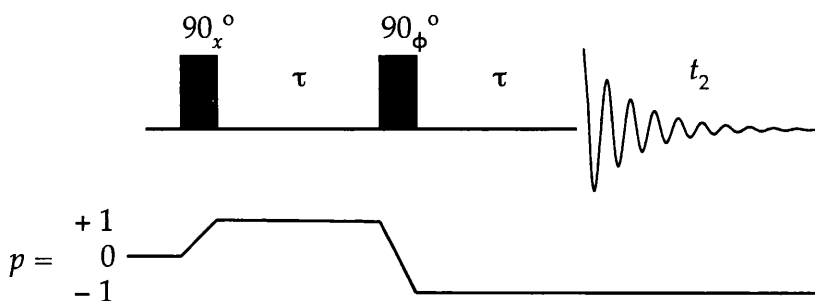


Figure 3.2: Quadrupolar-echo pulse sequence and coherence transfer pathway of an Exorcycled quadrupolar echo.

evident that what the spin-echo does is yield the same result that one would get immediately after a  $90^\circ$  pulse.

Figure 3.2 shows another echo sequence, called the quadrupolar, solid or dipolar echo method [3.5, 3.6], where a  $90^\circ$  pulse replaces the  $180^\circ$  pulse in the spin-echo sequence. The choice of echo sequence depends on the broadening present in a particular material. The Hahn echo is used when the broadening arises from chemical shift anisotropy or heteronuclear dipole-dipole coupling, while the solid echo deals with broadening originating from first-order quadrupolar coupling or homonuclear dipole-dipole coupling. In a quadrupolar-echo experiment, the echo is created by a  $90^\circ$  pulse as explained using tensor operators below. The initial state after the first  $90_x^\circ$  pulse is given by:

$$\sigma(0) = -I_y = -\frac{i[T_{1,-1} + T_{1,+1}]}{\sqrt{2}}, \quad (3.4)$$

and after taking into account the free precession of this initial state under the influence of the offset Hamiltonian and the first-order quadrupolar

Hamiltonian for a period  $\tau$ , the new density operator in the rotating frame is given by:

$$\begin{aligned} \sigma(\tau) = & \frac{i}{\sqrt{2}} \left[ T_{1,-1} \cos(\omega_Q \tau) + T_{1,+1} \cos(\omega_Q \tau) \right] \\ & + T_{2,-1} \sin(\omega_Q \tau) - T_{2,+1} \sin(\omega_Q \tau) . \end{aligned} \quad (3.5)$$

The second  $90^\circ$  pulse (phase-cycled to select  $\Delta p = -2$ , as shown in Fig. 3.2) is applied to form an echo following the free precession interval  $\tau$ :

$$\sigma(2\tau) = -\frac{i \left[ T_{1,-1} \right]}{\sqrt{2}} , \quad (3.6)$$

Only the  $p = -1$  coherences are retained, as these are the only operators observed during the FID. Both the quadrupolar splitting parameter  $\omega_Q$  and the offset  $\Omega$  were eliminated as a result of the coherence transfer pathway shown in Fig. 3.2 [3.7]. This echo sequence is known as the Exorcycled quadrupolar-echo, and will be used throughout this thesis.

## 3.4 Magic Angle Spinning (MAS)

### 3.4.1 Theory

Magic angle spinning is the term used to describe an NMR experiment performed while a sample placed in a rotor is spun (usually at tens of kHz) at an angle of  $54.74^\circ$  with respect to  $B_0$  [3.8, 3.9]. Figure 3.3

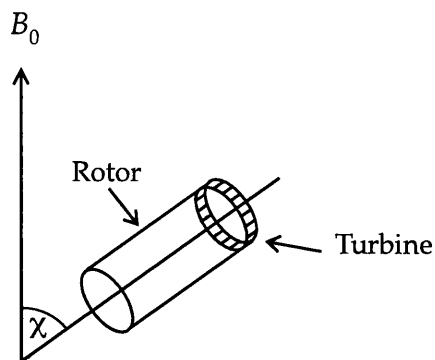


Figure 3.3: Magic angle spinning. Under MAS conditions,  $\chi$  would take the value of  $54.74^\circ$ .

illustrates this technique, which is used extensively in the work described in this thesis. Spinning at the magic angle averages to zero orientation-dependent terms, such as dipolar coupling that are described by an expression containing the term  $(3\cos^2\theta - 1)/2$ :

$$\begin{aligned}
 (3\cos^2\theta - 1)/2 &= 0 \\
 \cos^2\theta &= 1/3 \\
 \theta &= \cos^{-1}(1/\sqrt{3}) \\
 \theta &= 54.74^\circ .
 \end{aligned}
 \tag{3.7}$$

Consequently, MAS is the most widely used technique to produce narrower lines and hence high-resolution solid-state NMR. Commercially available MAS probes are capable of spinning rates of up to 70 kHz, with 30 kHz being nowadays routinely used on a modern spectrometer.

MAS tries to imitate what happens in solution-state NMR, where the effects of dipolar coupling and chemical shift anisotropy, amongst others, are rarely observed because of the rapid isotropic tumbling

molecules experience when in the liquid state. However, MAS can only completely suppress the first-order quadrupolar broadening, while it only removes the rank  $l = 2$  term of the second-order quadrupolar broadening. Hence, MAS alone is not enough to yield high-resolution spectra of most quadrupolar nuclei, as the second-order approximation also needs to be taken into account.

For most half-integer nuclei, it is necessary to consider the second-order perturbation and this remains true even under MAS conditions. The quadrupolar contributions to the energy levels were described in terms of Wigner rotation matrix elements described in Eq. (2.99), where the three Euler angles defined the rotation from the PAS to the LAB frame. When a sample is spun, the description of this transformation is made simpler by breaking it down into two parts: (i) the rotation from the PAS onto the sample (rotor) frame described using  $\beta'$  and  $\gamma'$ ; (ii) the rotation from the sample frame onto the LAB frame, described by angles  $\chi$  and  $-\nu_{\text{MAS}}t + \xi$ , where  $\chi$  takes the value of the magic angle, while  $\nu_{\text{MAS}}$  is the spinning frequency and  $\xi$  is the initial phase of an individual crystallite relative to the rotor. The Wigner rotation matrix elements can be expanded:

$$D_{0,n}^l(\alpha, \beta, \gamma) = \sum_{m=-l}^l D_{0,m}^l(0, \chi, -\nu_{\text{MAS}}t + \xi) D_{m,n}^l(0, \beta', \gamma'). \quad (3.8)$$

Substituting the expression for the second-order energy correction,  $E_i^2$ , given in Eqs. (2.102-2.105):

$$E_i^2 = -E_i^2 = \frac{(\omega_Q^{\text{PAS}})^2}{2\omega_0} \left\{ \begin{array}{l} A^0(L, m)Q^0(\eta_Q) \\ + A^2(L, m)d_{0,0}^2(\chi)Q^2(\beta', \gamma', \eta_Q) \\ + A^4(L, m)d_{0,0}^4(\chi)Q^4(\beta', \gamma', \eta_Q) \end{array} \right\}, \quad (3.9)$$

Equation (3.9) describes the second-order quadrupolar interaction averaged over one rotor period. The  $Q^0(\eta_Q)$  term is a purely isotropic term (Eq. (2.103)) and hence not effected by MAS, while the second- and fourth-rank terms are orientationally dependent:

$$Q^2(\beta', \gamma', \eta_Q) = \left(1 - \frac{\eta_Q^2}{3}\right)d_{0,0}^2(\beta') - \frac{\sqrt{8}}{\sqrt{3}}\eta_Q\{d_{2,0}^2(\beta')\cos 2\gamma'\}, \quad (3.10)$$

$$Q^4(\beta', \gamma', \eta_Q) = \left(1 + \frac{\eta_Q^2}{18}\right)d_{0,0}^4(\beta') + \frac{\sqrt{10}}{3}\eta_Q d_{2,0}^4(\beta')\cos 2\gamma' \\ + \frac{35}{9\sqrt{70}}\eta_Q d_{4,0}^4(\beta')\cos 4\gamma'. \quad (3.11)$$

Thus, for a single crystallite spinning at the magic angle, there is an isotropic shift of the central transition and anisotropic shifts of the second- and fourth-rank. Spherical averaging over the angles  $\beta'$  and  $\gamma'$  in a solid material gives rise to second- and fourth-rank inhomogeneous broadening. The reduced Wigner rotation matrix elements are given by:

$$d_{0,0}^2(\chi) = \frac{1}{2}(3\cos^2\chi - 1), \quad (3.12)$$

$$d_{0,0}^4(\chi) = \frac{1}{8}(35\cos^4\chi - 30\cos^2\chi + 3). \quad (3.13)$$

If  $\chi = 54.74^\circ$ , Eq. (3.12) will become equal to 0, while Eq. (3.13) will not.

The  $d_{0,0}^4(\chi)$  term equals zero when  $\chi = 30.56^\circ$  or  $70.12^\circ$ .

### 3.4.2 Experimental example

Examples of the spectra obtained when a powdered material is observed while spinning at the magic angle are shown in Fig. 3.4 using  $^{27}\text{Al}$  (spin  $I = 5/2$ ) MAS NMR of aluminium acetylacetonate ( $\text{C}_{15}\text{H}_{21}\text{AlO}_6$ ). Aluminium acetylacetonate consists of a single aluminium site with quadrupolar parameters of  $C_Q = 3.06$  MHz and  $\eta_Q = 0.15$ . MAS splits the broad powder pattern obtained when the material is observed under static conditions, into a series of spinning sidebands separated by the spinning rate as shown in Fig. 3.4a and more closely in Fig. 3.4ai. This only happens when the MAS rate is smaller than the anisotropic interactions. The spectrum shows a narrow high-intensity resonance originating from the central transition (CT), which is only affected by the second-order quadrupolar interaction (Fig. 3.4aii). The CT does not split into spinning sidebands, as the MAS rate (20 kHz) is larger than the anisotropy of its second-order quadrupolar perturbation. However, both satellite transitions  $\text{ST}_1$  and  $\text{ST}_2$  will resolve into a series of spinning sidebands.

The spinning sidebands are the frequency-domain equivalent of a series of echoes in the time-domain data, referred to as 'rotational echoes' in solid-state NMR [3.10]. When spinning at the magic angle, every crystallite in the sample will acquire a different orientation with respect to  $B_0$  and hence its evolution frequency varies. However, when the sample returns to its starting position, the evolution frequency returns back to its equilibrium position. This cycle is repeated several times. This

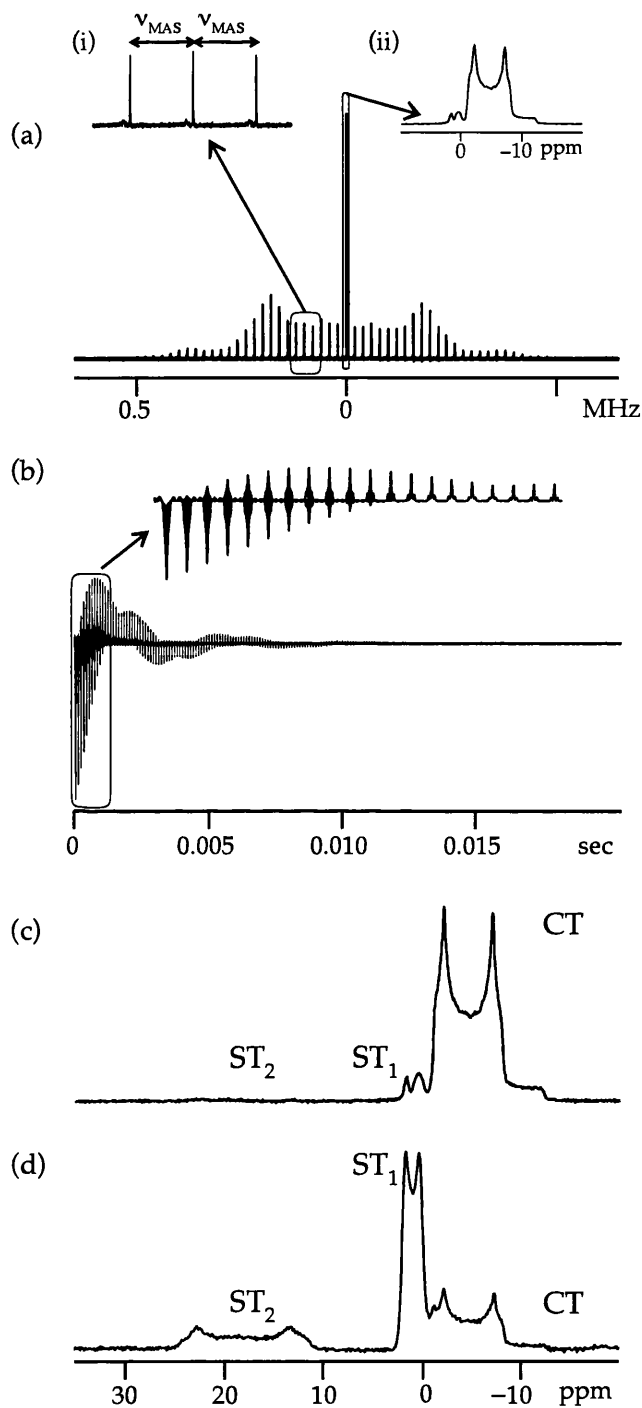


Figure 3.4:  $^{27}\text{Al}$  MAS NMR spectra of aluminium acetylacetonate. The spectra are the result of averaging (a, c) 2048 transients, acquired using a spectral width of 2 MHz and 20 kHz respectively, and (d) 4096 transients with a recycle interval of 1 s. The spectrum in (d) was recorded with rotor synchronization. The MAS rate was 20 kHz. (b) The FID of a MAS spectrum showing rotational echoes.

is what produces the rotational echoes in the FID of a spectrum acquired using MAS as shown in Fig. 3.4b. The separation of each spinning sideband is equal to the spinning frequency  $\nu_{\text{MAS}}$  as illustrated in Fig. 3.4a(i) and, therefore, the faster the spinning, the fewer the number of spinning sidebands observed as the separation between each spinning sideband increases.

### 3.4.3 Rotor synchronization

Occasionally, spinning sidebands are not desirable. This is mainly for reasons of resolution, but also for practical reasons as it is often cumbersome to process large datasets like those created when two-dimensional (or higher) spectra are acquired under MAS conditions. Figure 3.4c shows that it is possible to obtain just the centreband simply by acquiring over a narrower spectral width. Modern spectrometers automatically alter the width of the audiofrequency filter to make it match the spectral width chosen, implying that any resonances that fall outside this filter width will be lost [3.11]. The spectrum in Fig. 3.4c is dominated by the CT, as most of the intensity of the satellite transitions is in the spinning sidebands, which are not recorded. Consequently, this means that all the information outside the width of the audiofrequency filter is ignored and hence all the information previously carried by the spinning sidebands is now unavailable.

Rotor-synchronized acquisition is possible simply by setting the spectral width equal to  $\nu_{\text{MAS}}$ . This results in the 'aliasing' or 'folding', of all

the spinning sidebands onto the centreband as a consequence of the Nyquist theorem [3.12], hence producing just a single set of peaks, as shown in Fig. 3.4d. Many parameters need to be taken into account when rotor synchronizing, such as: the MAS rate is required to be very stable as any fluctuations in the spinning rate will result in the broadening of the signal, and the audiofrequency filter width must also be set to a value larger than the magnitude of the anisotropic interactions [3.11].

Comparing Fig. 3.4c with 3.4d, it is immediately evident that after rotor synchronization, the centrebands of the resonances,  $ST_1$  and  $ST_2$  gain intensity from the aliased spinning sidebands. This was achieved by using a spectral width of 20 kHz matching the MAS frequency, together with a 2 MHz audiofrequency filter width.

### 3.5 Heteronuclear Decoupling

The line-narrowing effects of MAS alone are sometimes not enough to produce sufficient spectral resolution. This is especially true when dealing with abundant nuclei such as  $^1\text{H}$ ,  $^{31}\text{P}$ , etc. [3.13]. Consider glycine, the chemical formula of which is shown in Fig. 3.5a. This material contains two environmentally distinct carbon sites: a carboxyl and a methylene carbon. Figure 3.5b shows the  $^{13}\text{C}$  MAS NMR spectrum of glycine. This spectrum is clearly made up of only one peak, at frequency 176.4 ppm, corresponding to the carboxyl carbon [3.14]. The

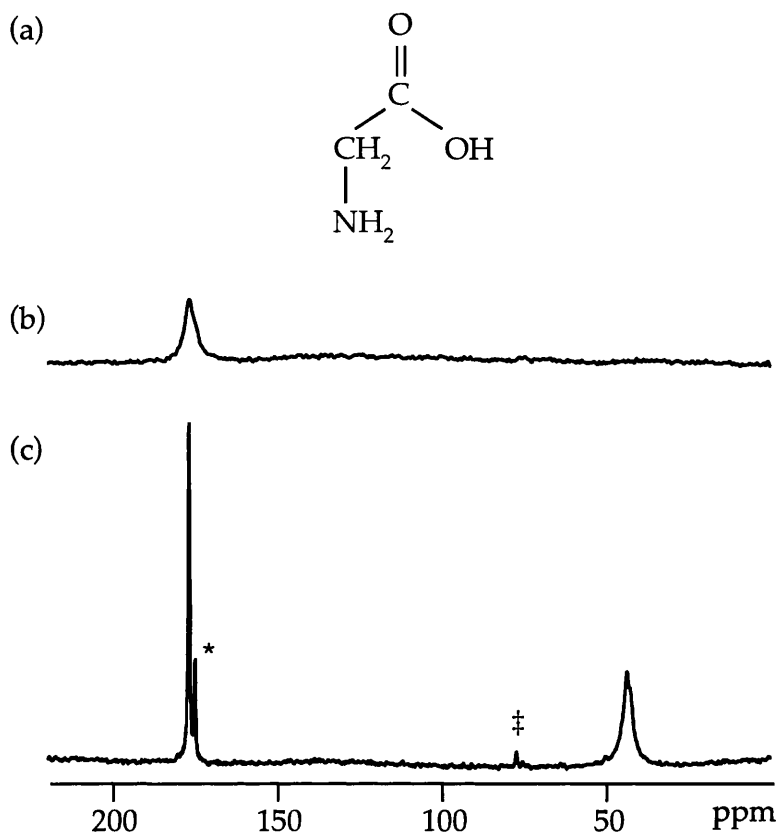


Figure. 3.5: (a) Chemical formula of glycine.  $^{13}\text{C}$  MAS NMR spectra of glycine (b) without and (c) with CW  $^1\text{H}$  decoupling. Both spectra were recorded using a MAS rate of 10 kHz and are the result of averaging 1024 transients while using a 30 s relaxation interval. \* marks an impurity in the sample and ‡ shows a spinning sideband of the carboxyl peak.

broadening is caused by heteronuclear dipolar coupling between the  $^1\text{H}$  nuclear spins and the detected  $^{13}\text{C}$ . Typically, the coupling constant of a  $^1\text{H}$ - $^{13}\text{C}$  pair is  $\sim 30$  kHz. Heteronuclear decoupling eliminates the effect of  $^1\text{H}$  nuclei on the  $^{13}\text{C}$  spectrum by manipulating the  $^1\text{H}$  spins in such a way that, when averaged over time their effect on the  $^{13}\text{C}$  nucleus will be equal to zero.

The simplest heteronuclear decoupling scheme involves high power, continuous wave (CW) on-resonance irradiation of the nucleus not being

observed during the detection. In other words, if a  $^{13}\text{C}$  spectrum is being recorded, the protons need to be irradiated in order to detect a decoupled  $^{13}\text{C}$  NMR spectrum such as that shown in Fig. 3.5c. In contrast to the spectrum in Fig. 3.5b, this consists of the expected two peaks corresponding to the distinct C sites in glycine. The carboxyl peak is eight times narrower after decoupling, and hence it is acceptable to assume that the absence of the methylene peak in Fig. 3.5b is due to its broadness when  $^1\text{H}$  decoupling is not implemented.

### 3.6 Inensitive Nuclei Enhance by Polarization Transfer (INEPT)

Originally, the INEPT experiment was designed to transfer magnetization from high- $\gamma$  nuclei, such as  $^1\text{H}$ , to enhance the weak NMR signals of low- $\gamma$  nuclei, such as  $^{13}\text{C}$ . Scalar ( $J$ ) coupling discussed in Section 2.5.3, is what makes the magnetization transfer between spins  $I$  and  $S$  possible. Here, the refocused-INEPT pulse sequence shown in Fig. 3.6, is going to be described using product operators discussed in Section 2.2.3.

The free precession interval  $\tau$  is set to approximately  $1/4J$  where  $J$  is the coupling constant between the two spins  $I$  and  $S$ . Consider an experiment where  $^{31}\text{P}$  and  $^{27}\text{Al}$  are spins  $I$  and  $S$  respectively. In this case,  $^{27}\text{Al}$  is going to be treated as a pseudo-spin  $I = 1/2$  nucleus as only the central transition is going to be taken into account as explained in Section

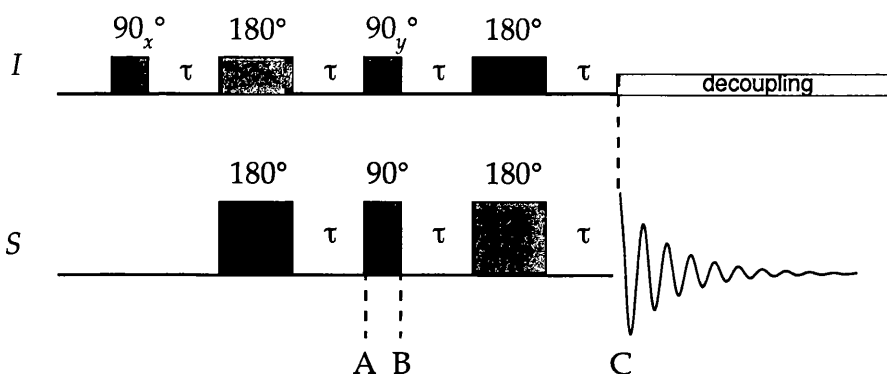


Figure 3.6: Pulse sequence for the refocused INEPT experiment.

2.2.3. After the  $90^\circ$  pulse on the  $^{31}\text{P}$  ( $I$  spin),  $I_z$  is transformed to  $-I_y$  while the  $S$  spin operators is not affected:

$$aI_z \xrightarrow{(90^\circ)_I} -aI_y. \quad (3.14)$$

where  $a$  is a parameter which gives the overall size of the equilibrium magnetization on spin  $I$ . The next step in the INEPT pulse sequence is a spin echo on both the  $I$  spins, and hence, as explained in Section 3.3, this refocuses the offset  $\Omega_I$  and hence can be ignored. The first  $180^\circ$  pulse on the  $S$  spin ensures that the heteronuclear  $J$  coupling  $J_{IS}$  continues to evolve throughout the first  $2\tau$  period. The resulting expression describing the spin system at A is given by:

$$\sigma_A(2\tau) = -aI_y \cos 2\pi J\tau + a2I_x S_z \sin 2\pi J\tau. \quad (3.15)$$

generating an anti phase state on the  $I$  spins. Substituting  $\tau$  with  $1/4J$  and applying the last  $90^\circ$  pulse on each spin, the expression in Eq. (3.15) becomes:

$$\sigma_B(\tau) = -a2I_z S_y. \quad (3.16)$$

Therefore, these two pulses have transformed the anti phase state from the  $I$  spin to the  $S$  spin. The standard INEPT experiment stops here; however it is very common to let anti phase magnetization evolve to an in phase state by applying two additional  $180^\circ$  pulses, one on each spin. This is known as refocused INEPT. The final state before acquisition can be expressed by:

$$\sigma_c(\tau) = aS_x . \quad (3.17)$$

Equation (3.17) shows that the refocused INEPT pulse-sequence produces a purely in-phase  $S$  spectrum. This sequence also allows for broadband  $I$ -spin decoupling during acquisition as shown in Fig. 3.6.

### 3.7 Multiple-Quantum Magic Angle Spinning (MQMAS)

As explained in Section 2.6.3, the CT is not affected by the quadrupolar interaction to a first-order approximation; however it is broadened to second-order. The rank  $l = 2$  contribution is removed when spinning at the magic angle, leaving only the isotropic and the scaled fourth-rank anisotropic terms. The latter is the term refocused in the MQMAS spectrum by correlating multiple-quantum (MQ) coherences in the  $t_1$  evolution period with the central-transition (CT) coherences in the  $t_2$  acquisition period as shown by Fig. 3.7a [3.15]. From Eq. (3.9) it follows that, for a spin  $I = 5/2$ , the second-order quadrupolar correction to the energy levels relevant to the triple-quantum transition is given by:

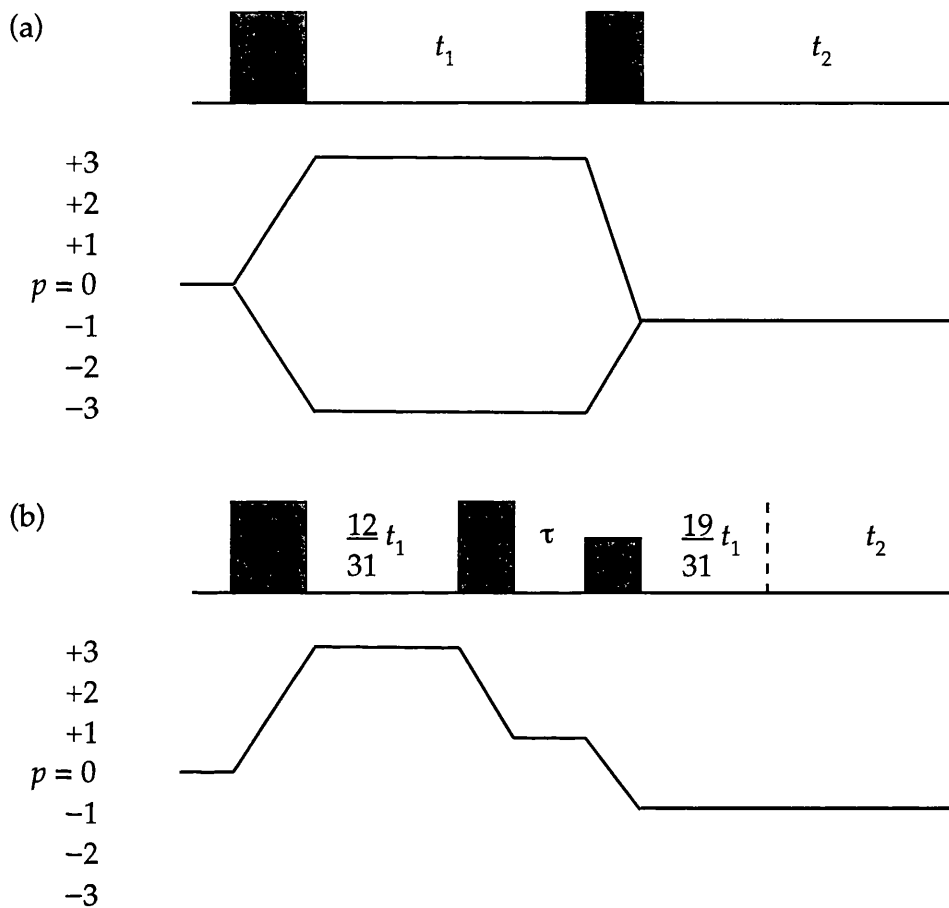


Figure 3.7: Pulse sequence and coherence transfer pathway diagram for (a) a typical MQMAS experiment and (b) a split- $t_1$  triple-quantum MAS experiment for a spin  $I = 5/2$  nucleus.

$$E_{3/2}^2 = E_{-3/2}^2 = \frac{(\omega_Q^{\text{PAS}})^2}{2\omega_0} \left\{ \begin{array}{l} A^0(5/2, 3/2)Q^0(\eta_Q) \\ + A^4(5/2, 3/2)Q^4(\alpha, \beta, \gamma, \eta_Q) \end{array} \right\}. \quad (3.18)$$

Hence that the time-domain signal for a triple-quantum MAS experiment on a spin  $I = 5/2$  nucleus can be expressed as:

$$\begin{aligned}
s(t_1, t_2) = & \exp\left(-i \frac{(\omega_Q^{\text{PAS}})^2}{\omega_0} \left\{ \begin{array}{l} -4/5 Q^0(\eta_Q) \\ +228/35 Q^4(\alpha, \beta, \gamma, \eta_Q) t_1 \end{array} \right\}\right) \\
& \times \exp\left(-i \frac{(\omega_Q^{\text{PAS}})^2}{\omega_0} \left\{ \begin{array}{l} -16/15 Q^0(\eta_Q) \\ +144/35 Q^4(\alpha, \beta, \gamma, \eta_Q) t_2 \end{array} \right\}\right).
\end{aligned} \tag{3.19}$$

The triple-quantum coherences are allowed to precess during the  $t_1$  period of the experiment before being converted to observable single-quantum, as seen by the pulse sequence and coherence transfer pathway in Fig. 3.7a. If  $t_2 = (228/144)t_1 = (-19/12)t_1$ , the orientationally-dependent fourth-rank term will be refocused, whilst the isotropic term will remain intact.

Since the introduction of this technique, much work has been carried out with the aim of optimizing this method. Three forms of the same experiment have been reported [3.16–3.18]. The form that will be used throughout this thesis is the so-called split- $t_1$  whole-echo MQMAS experiment introduced by Brown *et al.* [3.18, 3.19]. The pulse sequence and coherence transfer pathway is shown in Fig. 3.7b. As the name implies, the experiment splits the total  $t_1$  duration between the evolution period of the triple-quantum transition and the central-transition coherences. The ratio of the two parts of the  $t_1$  time for a triple-quantum MQMAS experiment for a spin  $I = 5/2$  is shown in the pulse-sequence. The phase cycling used ensures that only  $p = +3$  coherences are selected during the first part of  $t_1$ , while the final pulse ensures absorption-mode lineshapes as it produces a spin-echo like signal during  $t_2$ .

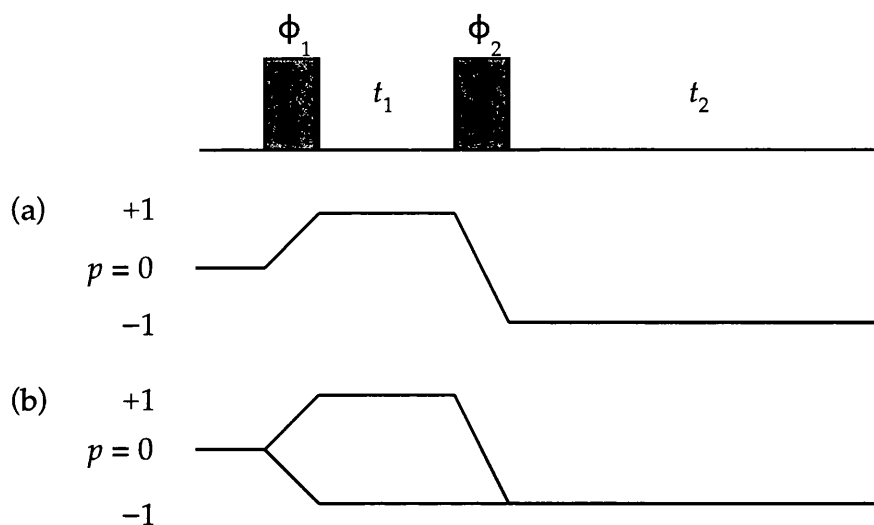


Figure 3.8: Pulse sequence for a simple two-dimensional experiment with two possible coherence transfer pathways. The resulting signal is (a) phase-modulated and (b) amplitude modulated with respect to  $t_1$ .

### 3.8 Frequency Discrimination in Two-Dimensional Experiments

Figure 3.8 shows the two types of coherence transfer pathways that can be used when acquiring a two-dimensional experiment, known as a (a) 'phase modulated' and (b) 'amplitude modulated'. Consider the coherence transfer pathway in Fig. 3.8a, where a single pathway is selected. In this case, a typical time-domain data set can be expressed by:

$$s(t_1, t_2) = \exp(-i\Omega t_1) \exp(-t_1/T_2) \exp(+i\Omega t_2) \exp(-t_2/T_2) . \quad (3.20)$$

A complex Fourier transformation in the  $t_2$  dimension gives:

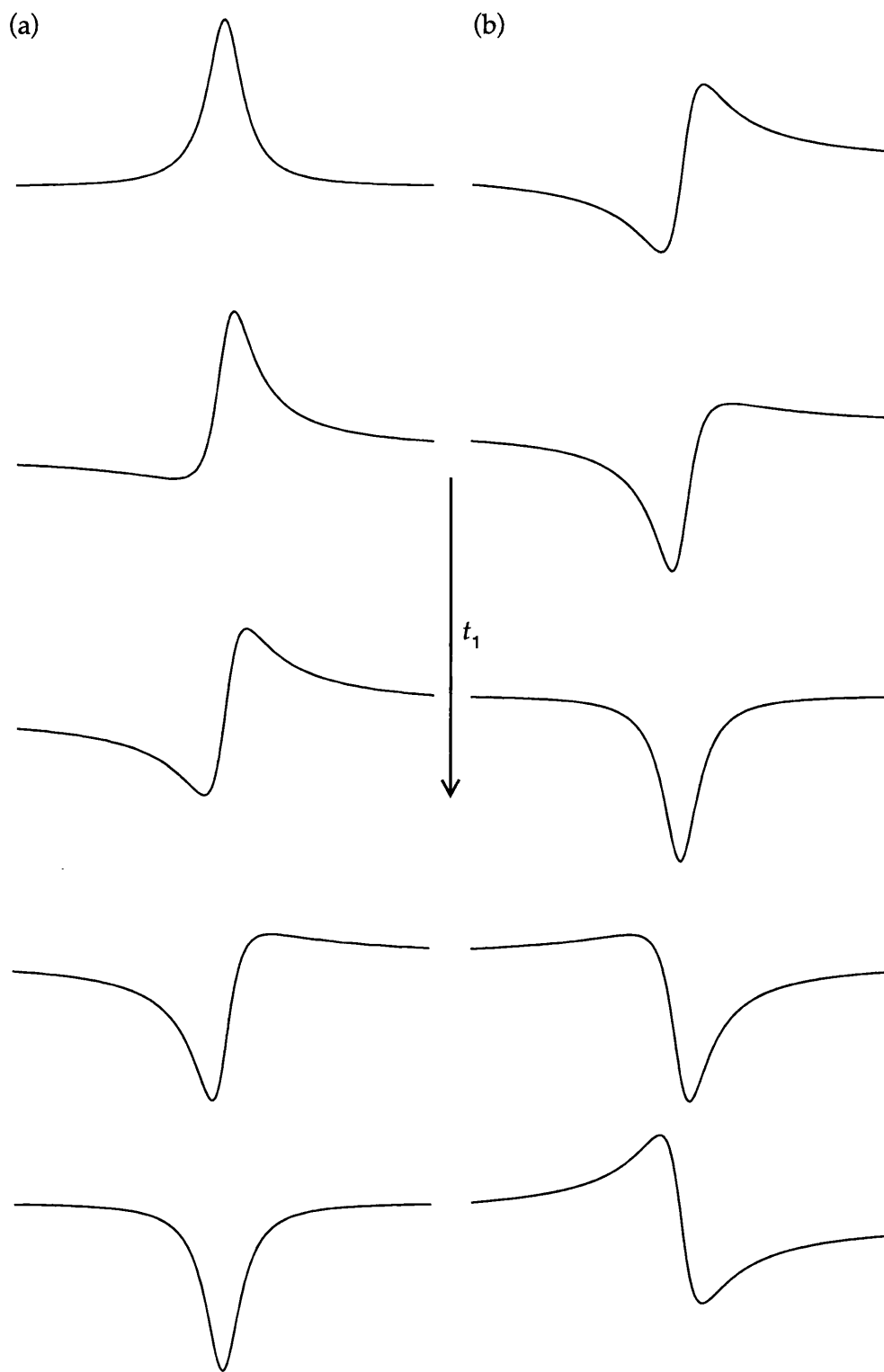


Figure. 3.9: (a) The real and (b) imaginary parts of one-dimensional spectra resulting from a complex Fourier transform with respect to  $t_2$  of selected rows, with increasing  $t_1$  as labelled, of a two-dimensional time-domain data set simulated for a single resonance with a small resonance offset, using the experiment in Fig. 3.8a. The spectra show phase-modulation behaviour with respect to  $t_1$ .

$$S(t_1, \omega_2) = \exp(-i\Omega t_1) \exp(-t_1/T_2) [A_2(+\Omega) - iD_2(+\Omega)], \quad (3.21)$$

where  $A_2(+\Omega)$  and  $iD_2(+\Omega)$  represent one-dimensional absorptive and dispersive Lorentzian lineshapes centred at a frequency  $\Omega$  in the  $\omega_2$  dimension (recall Eqs. (2.10) and (2.11)). Equation (3.21) implies that the phase of the lineshape in the  $\omega_2$  dimension varies as a function of  $t_1$ , as shown in Fig. 3.9, hence such a data set is known as 'phase-modulated' with respect to  $t_1$ . If a complex Fourier transform is subsequently performed in the  $t_1$  dimension, the resulting frequency domain spectrum will be given by:

$$\begin{aligned} S(\omega_1, \omega_2) &= [A_1(-\Omega) - iD_1(-\Omega)] \times [A_2(+\Omega) - iD_2(+\Omega)] \\ &= [A_1(-\Omega)A_2(+\Omega) - D_1(-\Omega)D_2(+\Omega)] \\ &\quad - i[A_1(-\Omega)D_2(+\Omega) + D_1(-\Omega)A_2(+\Omega)]. \end{aligned} \quad (3.22)$$

It is hence immediately obvious that the resulting spectra would be made up of both absorptive and dispersive components.

The coherence transfer pathway in Fig. 3.8b, on the other hand, illustrates that both  $p = +1$  and  $p = -1$  coherences are selected during  $t_1$ . The time-domain data of such experiment can be expressed by:

$$\begin{aligned} s(t_1, t_2) &= (\exp(-i\Omega t_1) + \exp(+i\Omega t_1)) \exp(-t_1/T_2) \exp(+i\Omega t_2) \exp(-t_2/T_2) \\ &= 2 \cos(+\Omega t_2) \exp(-t_1/T_2) \exp(+i\Omega t_2) \exp(-t_2/T_2). \end{aligned} \quad (3.23)$$

A complex Fourier transformation in the  $t_2$  dimension gives:

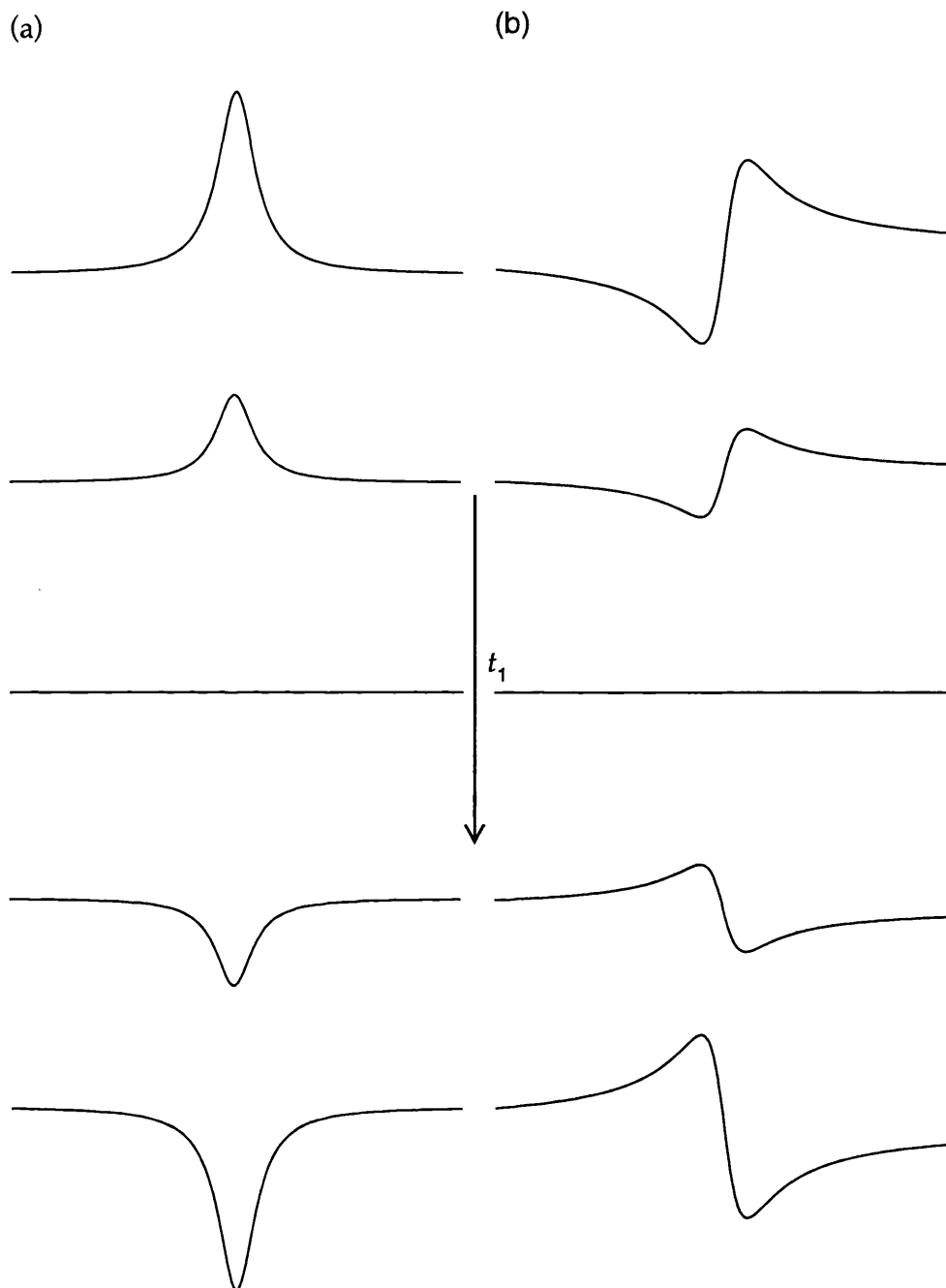


Figure. 3.10: (a) The real and (b) imaginary parts of one-dimensional spectra resulting from a complex Fourier transform with respect to  $t_2$  of selected rows, with increasing  $t_1$  as labelled, of a two-dimensional time-domain data set simulated for a single resonance with a small resonance offset, using the experiment in Fig. 3.8b. The spectra show amplitude-modulation behaviour with respect to  $t_1$ .

$$S(t_1, \omega_2) = 2 \cos(+\Omega t_1) \exp(-t_1/T_2) [A_2(+\Omega) - iD_2(+\Omega)]. \quad (3.24)$$

In contrast to Eq. (3.21), Eq. (3.24) shows that varying  $t_1$  alters the amplitude of the resonances, not the phase, as shown in Fig. 3.10. It follows, that this kind of data set is known as 'amplitude-modulated' with respect to  $t_1$ . To obtain pure-absorptive lineshapes, a complex Fourier transform in  $t_1$  needs to be performed on the real and imaginary parts of Eq. (3.24). This procedure is known as a hypercomplex Fourier transform. Considering only the real part, Eq. (3.24) becomes:

$$\begin{aligned} S(t_1, \omega_2) &= 2 \cos(+\Omega t_1) \exp(-t_1/T_2) A_2(+\Omega) \\ &= [\exp(-i\Omega t_1) + \exp(i\Omega t_1)] \exp(-t_1/T_2) A_2(+\Omega). \end{aligned} \quad (3.25)$$

Complex Fourier transformation in the  $t_1$  dimension then yields:

$$\begin{aligned} S(\omega_1, \omega_2) &= [A_1(-\Omega)A_2(-\Omega) + A_1(+\Omega)A_2(+\Omega)] \\ &\quad - i[D_1(-\Omega)A_2(+\Omega) + D_1(+\Omega)A_2(+\Omega)]. \end{aligned} \quad (3.26)$$

One disadvantage of this experiment is that the spectrum it produces is not frequency discriminated in  $t_1$ : modulation in  $t_1$  at a frequency  $\Omega$  will produce two peaks, one at  $+\Omega$  and one at  $-\Omega$ . However, since an amplitude-modulated experiment results in  $\cos(\Omega t_1)$  functions, and:

$$\cos(-\Omega t_1) \equiv \cos(+\Omega t_1), \quad (3.27)$$

then, a modulation at  $+\Omega$  is indistinguishable from a modulation at  $-\Omega$ . There are several ways of overcoming this problem, one of which is called the States-Haberkorn-Ruben or simply the States method [3.21].

One can obtain cosine- and sine-modulated data by repeating the two-dimensional pulse sequence with the phase of the first pulse shifted by  $90^\circ$  hence changing the modulation from  $\cos(\Omega t_1)$  to  $\sin(\Omega t_1)$ . The States method then uses that real part of the signal obtained after Fourier transforming the cosine-modulated data set with respect to  $t_2$  and adds it to the imaginary part of the Fourier transformed sine-modulated data set, hence creating a new data set:

$$\begin{aligned}
 S_{\text{States}}(t_1, \omega_2) &= S_c(t_1, \omega_2) + i S_s(t_1, \omega_2) \\
 &= [\cos(\Omega_A t_1) + i \sin(\Omega_A t_1)] \exp(-t_1/T_2) A_2(\Omega_B) \\
 &= \exp(i \Omega_A t_1) \exp(-t_1/T_2) A_2(\Omega_B),
 \end{aligned} \tag{3.28}$$

where the subscripts 'c' and 's' refer to cosine and sine, respectively, and  $\Omega_A$  and  $\Omega_B$  refer to the modulation frequencies in  $t_1$  and  $t_2$ , respectively. Fourier transformation with respect to  $t_1$  of Eq. (3.28) produces a purely absorptive two-dimensional data set:

$$\begin{aligned}
 S(\omega_1, \omega_2) &= [A_1(\Omega_A) - i D_1(\Omega_A)] A_2(\Omega_B) \\
 &= A_1(\Omega_A) A_2(\Omega_B) - i D_1(\Omega_A) A_2(\Omega_B).
 \end{aligned} \tag{3.29}$$

The term  $A_1(\Omega_A) A_2(\Omega_B)$  is the required double-absorption lineshape in the real spectrum.

# **$^2\text{H}$ Double-Quantum MAS NMR Spectroscopy as a Probe of Dynamics on the Microsecond Timescale**

---

### 4.1 Introduction

Reorientational dynamics in solids has attracted a huge interest, especially during the past twenty years. This arises from the realization that the properties of any solid material are dependent on how mobile the crystal structure of a material is, for example, the flexibility of the backbone of a polymer and the rapidity with which a water molecule flips about its  $C_2$  axis. Of course, only restricted mobility is expected to be experienced by a solid; however, investigating and measuring this motion gives an essential insight into the chemical and physical properties of a material.

Deuterium ( $^2\text{H}$ ) NMR spectroscopy is one of the most extensively used techniques to investigate motion in solids [4.1–4.3]. Examples in the literature go back to 1976 when Davis *et al.* [4.1] discussed the use of the quadrupolar echo in their investigation of the behaviour of the liquid

crystal nature of phospholipids hydrocarbon chains. Since then, numerous studies were published discussing dynamics using  $^2\text{H}$  NMR.

$^2\text{H}$  is a spin  $I = 1$  nucleus that exhibits relatively small quadrupole coupling constants, typically of the order of  $\sim 10^5$  Hz. As a result,  $^2\text{H}$  line-broadening is sensitive to motion on the microsecond timescale, making  $^2\text{H}$  NMR spectroscopy a very useful technique as it bridges the gap between two other NMR techniques used to study motion on the two time extremes: the second (very slow) timescale, and the nanosecond (very fast) timescale. Two-dimensional, or higher, exchange spectroscopy, is used to detect motion at the slow limit [4.4, 4.5]. Such techniques allow for the monitoring of the strength of the nuclear spin interaction during the  $t_1$  period, while allowing for reorientational dynamics to occur during the mixing period. At the other, fast motions extreme, spin-lattice relaxation time measurements are used [4.6, 4.7]. Spin-lattice relaxation time studies will be discussed in greater detail in Chapter 5.

The conventional way of using  $^2\text{H}$  NMR spectroscopy to investigate motion in solids is to record the spectra under static conditions [4.1]. The  $^2\text{H}$  quadrupolar-echo discussed in Section 3.3 is employed to acquire the spectra, which are then fitted with a computer-generated static lineshape. Parameters such as  $C_Q$  and the rate constant  $k$ , can be determined as a function of temperature to give an activation energy,  $E_A$  for the system [4.3, 4.4, 4.8]. Having been used for at least 30 years, static  $^2\text{H}$  NMR spectroscopy has proven to be a very robust and

popular method, although it is hampered by the shortcomings that are commonly associated with solid-state NMR spectra, such as low sensitivity and site resolution. As a result, there is increased interest in techniques that employ magic angle spinning (MAS) to study dynamics in solids, mainly because of the increase in resolution that is gained [4.3, 4.9–4.14].

As discussed in Section 3.4, magic angle spinning is used in solid-state NMR to refocus the effects of anisotropic interactions, such as dipolar coupling, chemical shift anisotropy and quadrupolar coupling, allowing high-resolution spectra to be recorded. However, as Maricq and Waugh discussed back in 1979 [4.8], MAS can fail in the presence of internal dynamics, causing linewidths to increase. At slow spinning rates, the MAS spectrum consists of a manifold of spinning sidebands, the envelope of which imitate the static quadrupolar lineshape. In addition, the removal of CSA, dipolar and first-order quadrupolar broadening by MAS may resolve environmentally distinct  $^2\text{H}$  sites in the material, permitting an independent analysis of each. As for the quadrupolar-echo method, NMR parameters can be obtained by recording  $^2\text{H}$  MAS NMR experiments and fitting the experimental spectra with computer-generated spectra.

The use of MAS has some disadvantages. Firstly, MAS probeheads have a smaller temperature range than static NMR probeheads, hence limiting the temperature investigation. The limitation arises due to the fact that the gas that is used to spin the sample flows at high speeds,

making it difficult to heat or cool efficiently as required. In addition, there is a danger that the gas may liquefy at low temperatures. Secondly, simulating MAS lineshapes is less straightforward than simulating static lineshapes and therefore greater computational sophistication is required. When dealing with static lineshapes, the Hamiltonian describing a given crystallite is time-independent, while for an MAS experiment, the Hamiltonian must be time-dependent, implying that for every one crystallite, it has to be calculated multiple times during every rotor period, hence making the computer program more laborious.

In this chapter, a novel approach to using  $^2\text{H}$  MAS NMR to study internal dynamics in deuterated solids will be demonstrated. As already done in other studies [4.9–4.13], the fact that the  $^2\text{H}$  MAS linewidths broaden if dynamic reorientation of the  $^2\text{H}$  quadrupole tensor occurs on the  $\mu\text{s}$ -timescale is used. However, information about the rate constant  $k$  of the dynamics present in the system is yielded by measuring the linewidths, rather than fitting the lineshapes. Consequently, by using a two-dimensional double-quantum MAS NMR experiment, where single-quantum coherences are correlated with double-quantum coherences, it will be shown that broadening is either absent or negligible in the double-quantum spectrum compared to that in the single-quantum spectrum. Hence, comparison of the linewidths of the peaks in the two dimensions of the  $^2\text{H}$  double-quantum MAS NMR experiment will yield information about the dynamics present in materials.

For accurate linewidth measurements, well-resolved lineshapes are essential: to facilitate this, rotor-synchronization is used. As mentioned in Section 3.4.3, rotor-synchronization in  $t_2$  produces a single set of peaks, as it aliases all the spinning sidebands present in the MAS NMR spectrum onto their centrebands, thereby also boosting the sensitivity. The  $t_1$  dimension is also rotor-synchronized as ' $t_1$  noise' [4.15] manifests itself in the form of spinning sidebands in the indirect frequency dimension, arising from 'reconversion rotor encoding' [4.16].  $t_1$  noise arises due to the sensitivity of the NMR signal to the fluctuations in the environment surrounding the material being investigated. Sources for  $t_1$  noise can be several, for example, fluctuations arising from an unstable magnetic field  $B_0$  and irreproducibility of the phase of radiofrequency pulses. To achieve rotor-synchronization in both dimensions of the two-dimensional experiment, a small spectral width is selected (equal to the MAS rate) in both dimensions while maintaining a wide audiofrequency filter width so that many fewer data points are needed across the lineshape while still guaranteeing high resolution in both  $\delta_1$  and  $\delta_2$  dimensions of the two-dimensional double-quantum MAS experiment.

## 4.2 Literature Review

In this section, selected papers that investigate dynamics in solids using  $^2\text{H}$  NMR are going to be outlined with the aim of showing the natural progression that led to the study discussed in this chapter. The

first paper that discussed  $^2\text{H}$  MAS NMR as a potential probe into dynamics was published in the early nineties by Kristensen *et al.* [4.17]. This paper presented a general method for calculating  $^2\text{H}$  MAS NMR spectra influenced by dynamic processes. The work in this paper was further elaborated in the later extensive work published by the same group in 1998 [4.10], which discussed the investigation of multiaxial dynamic processes. The stochastic Liouville equation is used as the basis for the evaluation of the effects of discrete random reorientation in the deuterated solid. In this publication, the authors present theoretical spectra and use them to demonstrate the applicability of  $^2\text{H}$  MAS NMR spectroscopy for investigating dynamics in solid materials. Their theory is confirmed by applying it to variable temperature  $^2\text{H}$  MAS NMR spectra of thiourea- $d_4$ , which are in turn compared to their corresponding quadrupolar echo lineshapes. They conclude that studying MAS spectra to investigate dynamics is highly viable, as it brings with it several advantages over the standard quadrupolar echo method, such as higher resolution and signal-to-noise ratio, as well as better sensibility to the presence of both slow and fast molecular dynamics.

In contrast, the quest of analysing motion in solids has taken Duer *et al.* [4.9] on a different route in which they too used MAS NMR spectra rather than the quadrupolar echo, but they utilised a  $^2\text{H}$  double-quantum NMR experiment to achieve their aim. The experiment presented in their 1997 paper, excites double-quantum coherence across different molecular sites as well as across different crystallite orientations, hence allowing for an accurate quantification of the particular motions present in the

material. They show how DQ peaks are narrower than their SQ counterparts, and suggest that a DQ MAS technique is potentially a technique that should be considered to probe motion in the future.

### 4.3 The Effect of Dynamics on Quadrupolar Lineshapes

Keeping in mind that dynamics in solids is very restricted when compared to the tumbling present in liquids, the simplest way to explain how solid materials behave in the presence of motion, is to start from understanding how liquid materials act in similar situations.

The easiest way to explain the mechanism of dynamic equilibria in liquid materials is to employ the widely used model known as the symmetrical two-site exchange [4.18]. Consider the molecule dimethylnitrosamine, where the nitroso group undergoes  $180^\circ$  rotation, allowing two conformations of equal energy labelled A and B in Fig. 4.1a. The transformation from form A to form B is a process called 'chemical exchange'. A symmetrical two-site exchange involves two equally populated sites with a difference in resonance frequencies of the two sites,  $\nu_A$  and  $\nu_B$ , respectively. The reorientation of the nitroso group induces a jump from frequency  $\nu_A$  to  $\nu_B$ , with a rate constant  $k$ . The evolution of the magnetisation of these two sites is described by the stochastic Liouville matrix,  $\mathbf{L}$  (refer to Eq. (2.52) and (2.53)):

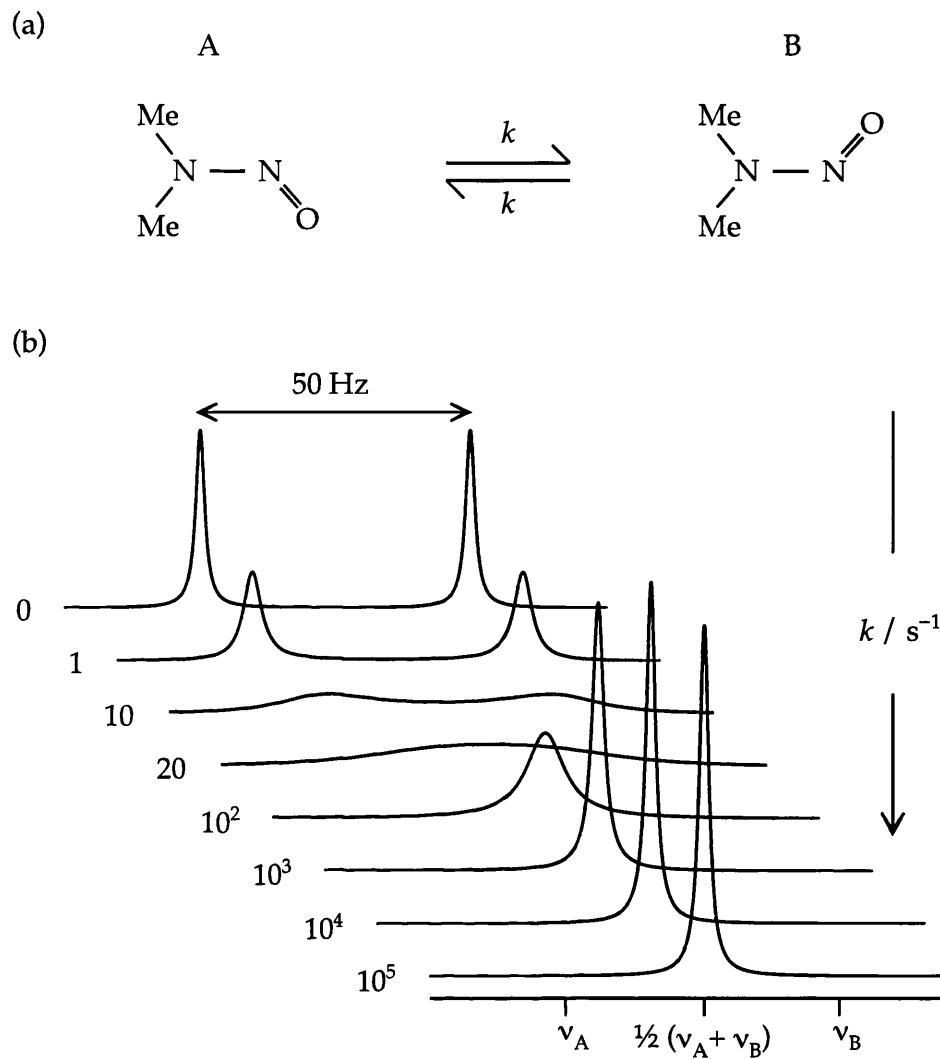


Figure 4.1: (a) Dimethylnitrosamine as an example of symmetrical two-site exchange. (b) Calculated NMR spectra for the exchange for two sites A and B separated by a frequency difference of 50 Hz.

$$\mathbf{L} = \begin{pmatrix} i2\pi\nu_A - k & k \\ k & i2\pi\nu_B - k \end{pmatrix}, \quad (4.1)$$

The time-dependent density operator that describes the magnetisation of the two sites undergoing symmetrical two-site exchange is given by:

$$\sigma(t) = \exp\left[ \begin{pmatrix} i2\pi\nu_A - k & k \\ k & i2\pi\nu_B - k \end{pmatrix} t \right] \sigma(0) \quad (4.2)$$

Or simply:

$$\mathbf{M}(t) = \mathbf{M}(0)\exp(\mathbf{L} t) . \quad (4.3)$$

Fourier transformation of Eq. (4.3) will give the analytical form of the frequency-domain lineshape function:

$$\begin{aligned} S(\nu) &= (1 \quad 1) \int_{-\infty}^{+\infty} \exp\left(\begin{pmatrix} i2\pi\nu_A - k & k \\ k & i2\pi\nu_B - k \end{pmatrix} t\right) \exp(-i2\pi\nu t) dt \begin{pmatrix} 1 \\ 1 \end{pmatrix} \\ &= \text{Re} \left( (1 \quad 1) \begin{pmatrix} i2\pi\nu_A - k - i2\pi\nu & k \\ k & i2\pi\nu_B - k - i2\pi\nu \end{pmatrix}^{-1} \begin{pmatrix} 1 \\ 1 \end{pmatrix} \right) . \end{aligned} \quad (4.4)$$

$$S(\nu) = \frac{k(\nu_A + \nu_B)(\nu_A - \nu_B)}{(-k(\nu_A - \nu_B) + \nu k)^2 + 4\pi^2(-\nu_A \nu_B + (\nu_A + \nu_B)\nu - \nu^2)^2} . \quad (4.5)$$

Equation (4.5) gives the exact solution for the lineshape of the curves in Fig. 4.1b, which shows simulated NMR spectra for conformations A and B undergoing symmetrical two-site exchange for a range of values of the exchange rate constant  $k$ . The spectra were simulated using a difference in resonance frequencies of the two sites of 50 Hz and a homogeneous linewidth in the absence of exchange,  $R_0/\pi$ , of 1 Hz. In the slow motional regime, i.e.  $k \ll |\nu_A - \nu_B|$ , two equally intense narrow peaks at frequencies  $\nu_A$  and  $\nu_B$  are observed. As  $k$  increases, the two peaks start to broaden, but remain at the same frequencies. As  $k$  increases further, first the two resonances merge into one broad peak centred at  $(\nu_A + \nu_B)/2$ , then it sharpens, until when  $k \gg |\nu_A - \nu_B|$ , where its width approaches the value of the homogeneous inherent linewidth.

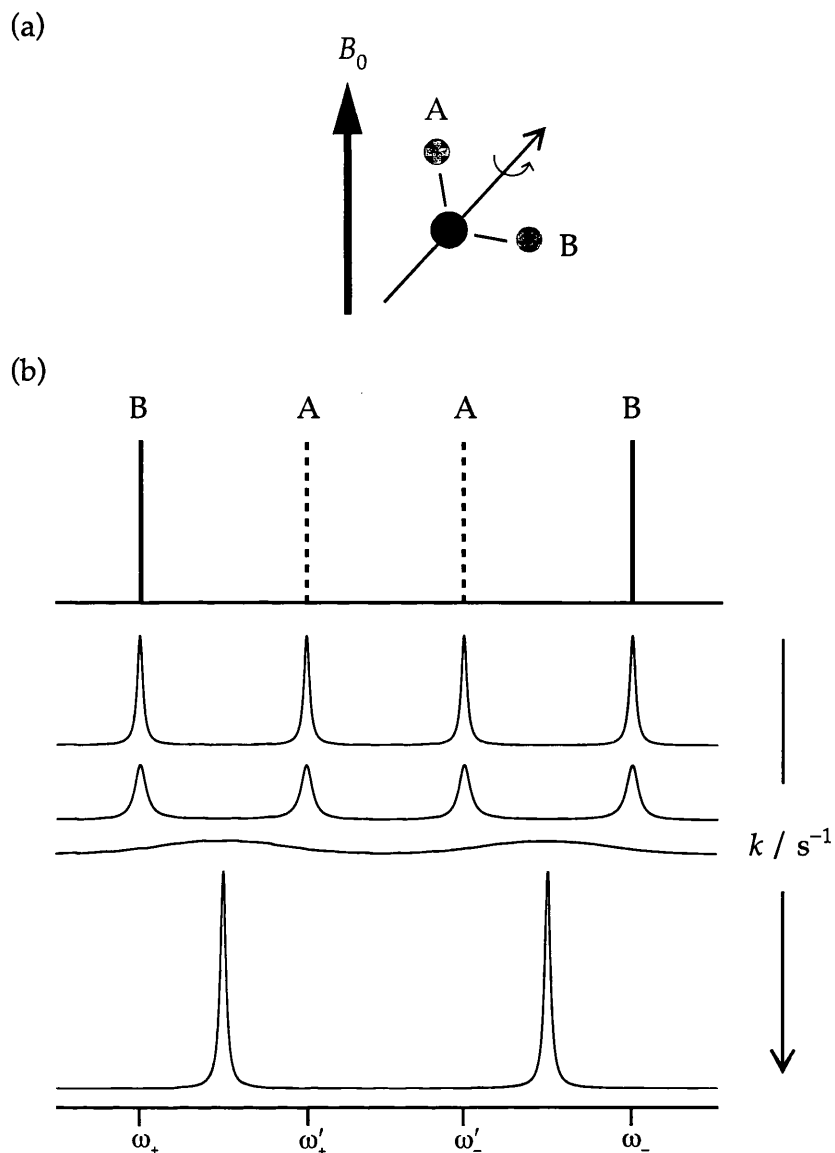


Figure 4.2: (a) Water molecule in a magnetic field  $B_0$ , (b) Schematic  $^2\text{H}$  NMR spectra of a molecule undergoing reorientation with a rate constant  $k$ .

In the solid state, the same approach can be used. Consider the simple example of a material containing deuterated water of crystallization, where a  $180^\circ$  reorientation of the water molecule is taking place about the  $C_2$  axis with a rate constant  $k$ . As shown in Fig. 4.2a, the two deuterium nuclei can now be identified with the sites A and B in the two-site exchange model. As mentioned in Section 2.6.2, each unique

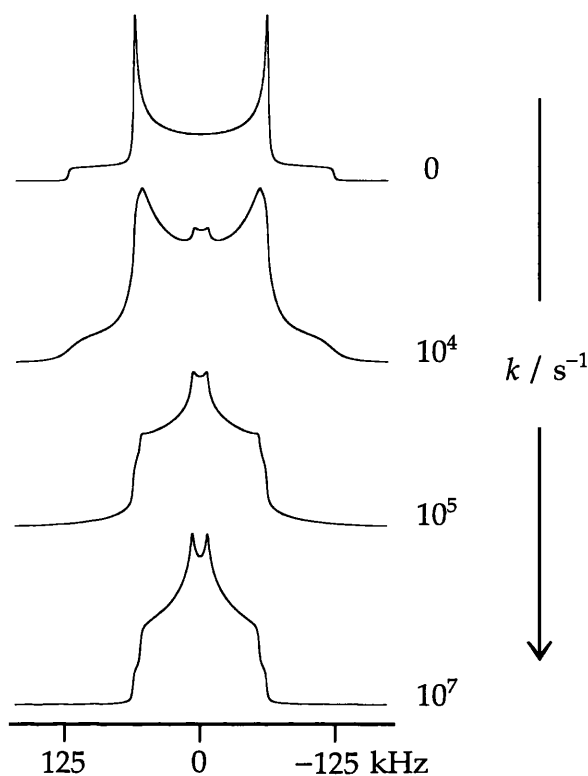


Figure 4.3: Simulated single-quantum  $^2\text{H}$  NMR spectra for a static powdered solid containing a water molecule undergoing  $180^\circ$  flips about the  $C_2$  axis with a rate constant  $k$ , quadrupolar coupling constant  $C_Q$  of 125 kHz, an  $\eta$  of 0 and DOD angle of  $104.5^\circ$ .

orientation produces a  $^2\text{H}$  doublet centred at  $\omega_0$  with the two resonances at  $\omega_+ = \omega_0 + \omega_Q$  and  $\omega_- = \omega_0 - \omega_Q$ . Therefore, each site will produce its own doublet, one arising from orientation A at  $\omega'_+ = \omega_0 + \omega'_Q$  and  $\omega'_- = \omega_0 - \omega'_Q$ , and the other arising from orientation B at  $\omega_+$  and  $\omega_-$ . Figure 4.2b shows how the four peaks (two from each site) behave as the rate constant increases. If only the high frequency side of the diagram is considered, i.e., taking one peak from A and another from B, it is immediately obvious that these behave as the symmetrical two-site exchange shown in Fig. 4.1b. In other words, as the rate constant  $k$  increases, the sharp peaks broaden, until they coalesce and merge into

one peak. Hence the two doublets that are produced when the rate constant is very small, transform into two sharp peaks when the  $k \gg |\nu_A - \nu_B|$ .

Therefore, the simple two-site exchange model can be used to explain the effect of exchange on  $^2\text{H}$  Pake doublet spectra. 'Powder averaging' over the large amount of crystallographically distinct deuterium nuclei produces a  $^2\text{H}$  Pake doublet (refer to Fig. 2.8d), and varying the rate constant  $k$  results in a variation of the  $^2\text{H}$  powder lineshape, as shown in Fig. 4.3.

#### 4.4 Theory of Motional Broadening in Solids Under MAS

##### 4.4.1 Introduction

Motional broadening experienced by NMR lineshapes acquired under MAS conditions raised the interest of many. Maricq and Waugh in their 1979 paper [4.8] briefly discussed this phenomenon. They point out that while dynamics manifests itself as distortions of a powder pattern lineshape in stationary samples, it is even more prominent in spinning samples as it causes the rotational echo trains to decay. Since this paper, several articles discussing different aspects of motional dynamics were written [4.19, 4.20]. More recently however, it has been shown by Ashbrook *et al.* [4.21] that broadening observed in the isotropic

dimension of  $^{17}\text{O}$  peaks in satellite-transition (ST) MAS spectra [4.22–4.24] of chondrodite and clinohumite, arises from dynamic reorientation. It was shown that motion on the microsecond timescale could be probed and linewidths predicted using the relatively simple motional broadening model. In this section, this simple model, here referred to as the 'spin-echo' model, is going to be discussed. It will also be compared to exact simulations, performed by M. J. Thrippleton, to confirm the validity of this method as a model to quantify motional broadening in solids [4.25].

#### 4.4.2 $^2\text{H}$ MAS NMR

The typical magnitude of a  $^2\text{H}$  first-order quadrupolar broadening is  $\sim 250$  kHz hence, as explained in Section 3.4, if a MAS rate of 10 kHz is used, the  $^2\text{H}$  MAS NMR spectrum obtained will consist of a series of spinning sidebands separated by 10 kHz. Spinning sidebands in the frequency-domain are the result of a train of sharp rotary echoes, separated by  $\tau_{\text{MAS}} = 1/\nu_{\text{MAS}}$ , in the time domain.

When motion is present, a dynamics-induced reorientation of the  $^2\text{H}$  quadrupole tensor during the rotor period will produce a large 'jump' in the single-quantum precession frequencies, with a typical magnitude of  $\sim 100$  kHz. This jump will interfere with the formation of the echo at the end of the period, attenuating successive rotary echoes and resulting in motionally-broadened spinning sidebands. In contrast, the  $^2\text{H}$  double-quantum transition does not exhibit this kind of behaviour, as it is not

affected by first-order quadrupolar broadening. The double-quantum linewidth in a static solid is dominated by weaker interactions such as the chemical shift anisotropy and dipolar couplings, which both have a very small magnitude compared to the first-order quadrupolar coupling. Consequently, any dynamics-induced jump will be much smaller than the MAS rate, and will not produce a significant motionally-broadened line.

#### 4.4.3 The spin-echo model

The spin-echo model is once again based on the symmetrical two-site exchange, where two equally populated 'sites', A and B, such as the two deuterons in a water ( $D_2O$ ) molecule, are exchanging due to a dynamic reorientation ( $D_2O$  molecule flipping about its  $C_2$  axis) [4.21, 4.25, 4.26]. For simplicity, this model describes MAS as a series of spin echoes with a  $180^\circ$  pulse in every rotor period ( $\tau_{MAS}$ ), rather than a train of rotary echoes. During the first half of the echo period, i.e.,  $t = 0$  to  $\tau_{MAS}/2$ , the magnetizations  $M_A(t)$  and  $M_B(t)$  of the two sites evolve under the Liouvillian  $L^-$  and, during the second half of the period,  $t = \tau_{MAS}/2$  to  $\tau_{MAS}$ , under the Liouvillian  $L^+$ , given by:

$$L^\pm = \begin{pmatrix} -R_0 \pm 2\pi i\nu_A - k & k \\ k & -R_0 \pm 2\pi i\nu_B - k \end{pmatrix}, \quad (4.6)$$

where  $\nu_A$  and  $\nu_B$  are the resonance frequencies of sites A and B,  $k$  is the first-order rate constant for the dynamic process and  $R_0$  is the homogeneous decay constant of the peaks in the absence of dynamics. An

average Liouvillian,  $\bar{\mathbf{L}}$ , can be calculated from  $\mathbf{L}^-$  and  $\mathbf{L}^+$  for a rotor period:

$$\mathbf{M}(\tau_{\text{MAS}}) = \mathbf{M}(0)\exp(\bar{\mathbf{L}}\tau_{\text{MAS}}), \quad (4.7)$$

where

$$\exp(\bar{\mathbf{L}}\tau_{\text{MAS}}) = \exp\left(\frac{\mathbf{L}^+\tau_{\text{MAS}}}{2}\right)\exp\left(\frac{\mathbf{L}^-\tau_{\text{MAS}}}{2}\right). \quad (4.8)$$

The resulting spectrum is the sum of two Lorentzian lines, with linewidths directly proportional to the eigenvalues of  $-\bar{\mathbf{L}}$ , which correspond to the homogeneous decay rate constant,  $R$ , of the peaks in the presence of dynamics.  $R$  can be approximated by a single analytical formula because the two Lorentzian lines produced have nearly identical linewidths:

$$R = -\frac{1}{\pi\tau_{\text{MAS}}}\ln\left(\frac{C-2kBD}{E}\right) + R_0, \quad (4.9)$$

where:

$$A = -\sqrt{4k^2 - \Delta v_{\text{jump}}^2}, \quad (4.10)$$

$$B = -1 + \exp\left(\frac{1}{2}\tau_{\text{MAS}}A\right), \quad (4.11)$$

$$C = 2B^2k^2 + A^2\exp\left(\frac{1}{2}\tau_{\text{MAS}}A\right), \quad (4.12)$$

$$D = \sqrt{B^2k^2 + A^2\exp\left(\frac{1}{2}\tau_{\text{MAS}}A\right)}, \quad (4.13)$$

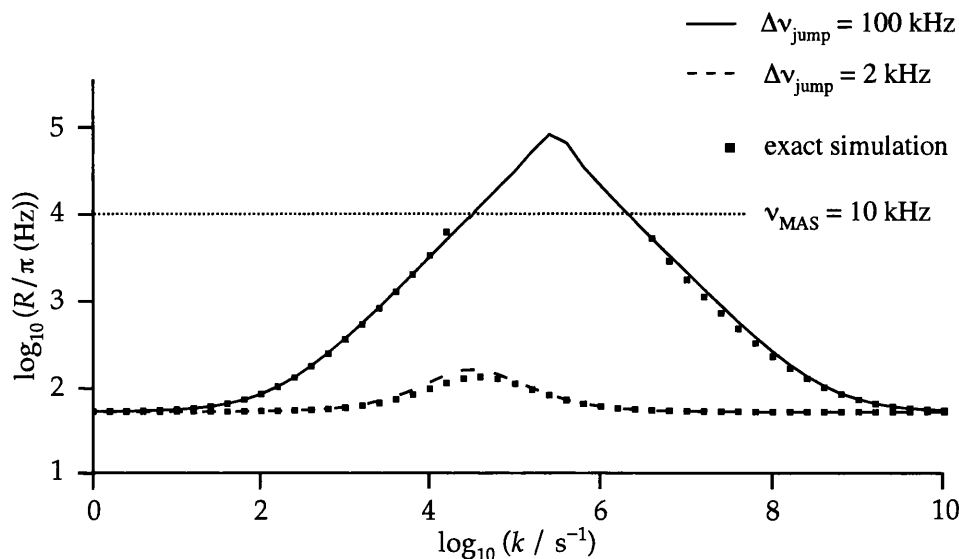


Figure 4.4:  $\log_{10}$  of the full single-quantum ( $\Delta\nu_{\text{jump}} = 100$  kHz) and double-quantum ( $\Delta\nu_{\text{jump}} = 2$  kHz) MAS linewidths at half height in Hz,  $(R/\pi)$ , as a function of  $\log_{10}$  of the rate constant  $k$  as predicted by the spin-echo model for deuterium atoms in  $\text{D}_2\text{O}$  molecules. The MAS rate was 10 kHz (marked with a dotted horizontal line) and the dynamics-free linewidth  $R_0/\pi$  was 50 Hz.

$$E = A^2 \exp\left(\frac{1}{2} \tau_{\text{MAS}} (2k + A)\right). \quad (4.14)$$

where  $\Delta\nu_{\text{jump}} = |\nu_A - \nu_B|$ .

This model describes motionally broadened MAS linewidths under all motional regimes. A plot of the full linewidth at half-height measured in Hz,  $R/\pi$ , against the dynamic rate constant  $k$  on a  $\log_{10}$ - $\log_{10}$  scale as shown in Fig. 4.4 for a MAS rate of  $\nu_{\text{MAS}} = 10$  kHz, a dynamics-free full linewidth of  $R_0/\pi = 50$  Hz, and for frequency jumps  $\Delta\nu_{\text{jump}} = 100$  kHz (typical  $^2\text{H}$  single-quantum transition) and  $\Delta\nu_{\text{jump}} = 2$  kHz (typical  $^2\text{H}$  double-quantum transition). It is very clear from the graph that the maximum linewidth of the single-quantum  $^2\text{H}$

MAS sidebands is nearly three orders of magnitude greater than the maximum linewidth of the double-quantum  $^2\text{H}$  MAS transition.

In the limit  $k \ll \Delta\nu_{\text{jump}}$  and  $k \ll \nu_{\text{MAS}}$ , the linewidth for the single-quantum transitions (i.e., when  $\Delta\nu_{\text{jump}} \gg \nu_{\text{MAS}}$ ) may be expressed:

$$\frac{R}{\pi} = \frac{k}{\pi} + \frac{R_0}{\pi}, \quad (4.15)$$

and for the double-quantum ( $\Delta\nu_{\text{jump}} \ll \nu_{\text{MAS}}$ ):

$$\frac{R}{\pi} = \frac{\pi(\Delta\nu_{\text{jump}})^2 k}{24(\nu_{\text{MAS}})^2} + \frac{R_0}{\pi}. \quad (4.16)$$

In the limit  $k \gg \Delta\nu_{\text{jump}}$  and  $k \gg \nu_{\text{MAS}}$ , both single- and double-quantum linewidths are given by the same expression:

$$\frac{R}{\pi} = \frac{\pi(\Delta\nu_{\text{jump}})^2}{2k} + \frac{R_0}{\pi}. \quad (4.17)$$

For the case shown in Fig. 4.4, i.e. when  $\nu_{\text{MAS}} = 10$  kHz and a single-quantum frequency jump of 100 kHz is considered, the model predicts that over nearly two orders of magnitude of  $k$ , from  $\log_{10}(k/s^{-1}) = 4.5$  to  $\log_{10}(k/s^{-1}) = 6.2$ , the linewidth of the single-quantum transition would exceed the spinning speed and hence the peaks would not be observable. Duer *et al.* [4.9] and Kristensen *et al.* [4.10, 4.11] have observed this same behaviour in the exact simulations carried out on  $^2\text{H}$  NMR as part of their work to investigate dynamics in solids.

It must be noted that the spin-echo model breaks down when the value of  $k$  approaches  $\sim 2\pi\nu_0$ . In this limit, non-secular parts of the quadrupolar Hamiltonian may no longer be neglected and the dynamics within the material become rapid enough to induce  $\Delta m_l = \pm 1$  and  $\pm 2$  transitions, resulting in the broadening of both single-quantum and double-quantum transitions by the quadrupolar interaction.

The validity of the simple spin-echo model was discussed by Thrippleton *et al.* in Ref. [4.25], where this model is compared with exact numerical simulations to confirm that the predictions of the model are well-founded. As seen from Fig. 4.4, linewidths from the exact simulation plot (squares) are very similar to those predicted by the spin-echo model (solid and dashed lines), especially in the slow-spinning regime. Thrippleton *et al.* go on to discuss the agreement of the spin-echo method with other earlier linewidth prediction methods [4.8, 4.20].

## 4.5 Experimental Procedures

### 4.5.1 *The double-quantum MAS NMR experiment*

Figure 4.5 shows the pulse sequence and coherence transfer pathway diagram [4.27, 4.28] used to record two-dimensional  $^2\text{H}$  double-quantum MAS NMR spectra. The first pulse in the double-quantum MAS

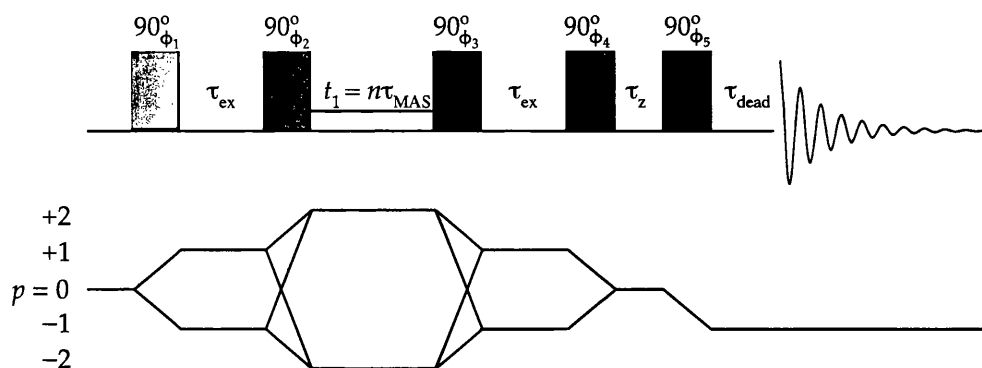


Figure 4.5: Pulse sequence and coherence transfer pathway diagram used to record two-dimensional  $^2\text{H}$  double-quantum MAS NMR spectra. The coherence pathway was selected with a 16-step phase-cycle:  $\phi_1 = \phi_2 = 0^\circ 90^\circ 180^\circ 270^\circ$ ;  $\phi_3 = \phi_4 = 0^\circ$ ;  $\phi_5 = \{0\} \times 4 \{90^\circ\} \times 4 \{180^\circ\} \times 4 \{270^\circ\} \times 4$ ;  $\phi_R = 0^\circ 180^\circ 0^\circ 180^\circ 90^\circ 270^\circ 90^\circ 270^\circ 180^\circ 0^\circ 180^\circ 0^\circ 270^\circ 90^\circ 270^\circ 90^\circ$ , where  $\phi_i$  is the phase of the  $i$ th pulse and  $\phi_R$  is the phase of the receiver.

pulse sequence generates single-quantum coherences ( $p = \pm 1$ ). The initial state immediately after the  $90^\circ$  pulse is given by:

$$\sigma(0) = -\frac{i[T_{1,-1} + T_{1,+1}]}{\sqrt{2}}, \quad (4.18)$$

where  $T_{n,p}$  are tensor operators defined in Appendix B. After taking into account the first-order quadrupolar Hamiltonian as explained in Section 3.3, for a period  $\tau_{ex}$ , the density operator is given as follows:

$$\begin{aligned} \sigma(\tau_{ex}) = & \frac{i}{\sqrt{2}} [ T_{1,-1} \cos(\omega_Q \tau_{ex}) + T_{1,+1} \cos(\omega_Q \tau_{ex}) ] \\ & + T_{2,-1} \sin(\omega_Q \tau_{ex}) - T_{2,+1} \sin(\omega_Q \tau_{ex}). \end{aligned} \quad (4.19)$$

In this experiment,  $\tau_{ex}$  is very short compared to the rotor period. Consequently, the effect of MAS was not taken into account. The second

90° pulse is used to excite double-quantum coherences ( $p = \pm 2$ ), and phase-cycling ensures that only these are selected after this pulse:

$$\sigma(t_1 = 0) = i[T_{2,-2} - T_{2,+2}] \sin(\omega_Q \tau_{\text{ex}}). \quad (4.20)$$

During the  $t_1$  period, the spins precess under the free precession Hamiltonian,  $H_z = \Omega I_z$  (refer to Eq. 2.20).  $H_Q$  need not be taken into account in this step as only double-quantum coherences are selected by the phase-cycling in this period, and these are not affected by the quadrupolar interaction:

$$\begin{aligned} \sigma(t_1) = & -i \sin(\omega_Q \tau_{\text{ex}}) \left[ T_{2,+2} (-\cos(2\Omega t_1) + i \sin(2\Omega t_1)) \right. \\ & \left. + T_{2,-2} (\cos(2\Omega t_1) + i \sin(2\Omega t_1)) \right]. \end{aligned} \quad (4.21)$$

The third 90° pulse takes the double-quantum coherences back to antiphase single-quantum coherences:

$$\sigma(t_1 + t_{90}) = \cos(2\Omega t_1) \sin(\omega_Q \tau_{\text{ex}}) [T_{2,1} - T_{2,-1}], \quad (4.22)$$

which in turn evolves under the influence of  $H_Q$  to produce in-phase single-quantum magnetization:

$$\begin{aligned} \sigma(\tau_{\text{ex}}) = & \cos(2\Omega t_1) \sin(\omega_Q \tau_{\text{ex}}) \left[ (T_{2,1} - T_{2,-1}) \cos(\omega_Q \tau_{\text{ex}}) \right. \\ & \left. - \frac{i(T_{1,1} + T_{1,-1})}{\sqrt{2}} \sin(\omega_Q \tau_{\text{ex}}) \right]. \end{aligned} \quad (4.23)$$

The fourth 90° pulse converts the  $\pm 1$  coherences into populations ( $p = 0$ ):

$$\sigma(\tau_z) = -T_{1,0} \cos(2\Omega t_1) \sin^2(\omega_Q \tau_{\text{ex}}), \quad (4.24)$$

while the last  $90^\circ$  pulse converts this into observable coherence ( $p = -1$ ):

$$\sigma(t_2 = 0) = i\sqrt{2} T_{1,-1} \cos(2\Omega t_1) \sin^2(\omega_Q \tau_{ex}). \quad (4.25)$$

The free-precession period,  $\tau_{ex}$ , allows in-phase and anti phase single-quantum coherences to interconvert and hence its duration is set to be approximately equal to the inverse of the width of the  $^2\text{H}$  static powder lineshape. A  $4 \mu\text{s}$   $\tau_{ex}$  was used in all the experiments presented here. The interval  $\tau_z$  is limited only by the time required for clean phase shifting of the pulses, which in this case was only  $2 \mu\text{s}$ .

Since rotor-synchronization in  $t_2$  is being used, the pre-acquisition interval  $\tau_{dead}$  was optimized carefully such that the first data point of the FID was acquired precisely at the peak of the first rotary echo. Since linewidths are the source of information in this experiment, stable spinning rate is also essential: instability causes inaccurate aliasing of the spinning sidebands, causing increased peak broadening. The  $t_1$  evolution period was also rotor-synchronized [4.29], with  $t_1$  equal to  $n\tau_{MAS}$  and incrementing  $n = 1, 2, 3$ , etc.

Using a symmetric excitation-reconversion scheme [4.30] and the z-filter [4.31] ensures that the spinning sidebands detected in the acquisition period  $t_2$  are in phase, thereby permitting rotor-synchronization. As a result of the z-filter, this experiment is amplitude-modulated; and in order to obtain pure-absorption two-dimensional lineshapes, the States-Haberhorn-Ruben (States) method of  $\delta_1$  sign discrimination was used (refer to Section 3.8).

#### 4.5.2 *Experimental details*

$^2\text{H}$  MAS NMR spectra were obtained at a Larmor frequency of 61.4 MHz on a Bruker Avance 400 spectrometer, equipped with a widebore 9.4 T magnet. Powdered deuterated samples were packed into 4-mm diameter  $\text{ZrO}_2$  rotors. The radiofrequency field strength ( $\nu_1 = \gamma B_1 / 2\pi$ ) used was approximately 100 kHz, corresponding to a  $90^\circ$  pulse length of 2.5  $\mu\text{s}$ . The spinning angle was adjusted to be as close as possible to the magic angle by minimizing the linewidth of the carboxyl  $^2\text{H}$  resonance in oxalic acid dihydrate- $d_6$ . Chemical shifts are recorded in parts per million relative to oxalic acid dihydrate- $d_6$ , which is used as a secondary reference (COOD peak at 17 ppm) [4.32].

### 4.6 Results

#### 4.6.1 *Introduction*

As a test of the novel  $^2\text{H}$  double-quantum MAS NMR method, a series of deuterated materials were investigated. The examples presented in this section illustrate various extents of reorientational dynamics on the microsecond timescale in solids. For each material, the DQMAS experiment was performed at various temperatures to obtain a greater insight on the behaviour of the internal dynamics of a system and hence allow for the measurement of parameters such as the rate constant  $k$  and

the activation energy. Each material and respective results obtained will be discussed in their relevant section later on in this chapter. Unless otherwise stated, all materials used were deuterated by crystallization from D<sub>2</sub>O solution (99.9 at.% <sup>2</sup>H, Aldrich) to enhance the <sup>2</sup>H abundance from its natural level of 0.015% to ~100%.

#### 4.6.2 Oxalic acid dihydrate-*d*<sub>6</sub>

Oxalic acid dihydrate-*d*<sub>6</sub>, (COOD)<sub>2</sub>·2D<sub>2</sub>O (deuterated from oxalic acid dihydrate, 99.5% SIGMA) contains units of two chemically distinct deuterium sites: the carboxyl and the water deuterons. Consequently, its <sup>2</sup>H MAS NMR spectrum consists of two peaks: a sharp carboxyl deuteron peak (full linewidth at half height of 50 Hz) and a broad water deuteron peak (full linewidth at half height of 900 Hz). Figure 4.6a shows the <sup>2</sup>H MAS NMR spectrum recorded with a wide spectral width and using a MAS rate of 10 kHz, producing a spectrum made up of a series of spinning sidebands located 10 kHz apart. After rotor synchronization (Fig. 4.6b), just the two expected peaks are observed (refer to Section 3.4.3). Figure 4.6c shows the two-dimensional <sup>2</sup>H double-quantum MAS NMR spectrum recorded using rotor synchronization in the *t*<sub>1</sub> period, but using conventional (not rotor synchronized) acquisition in the *t*<sub>2</sub> period. This shows the MAS sideband spectra of the carboxyl and water deuterons in the δ<sub>2</sub> dimension, separated by their double-quantum frequencies in the δ<sub>1</sub> dimension.

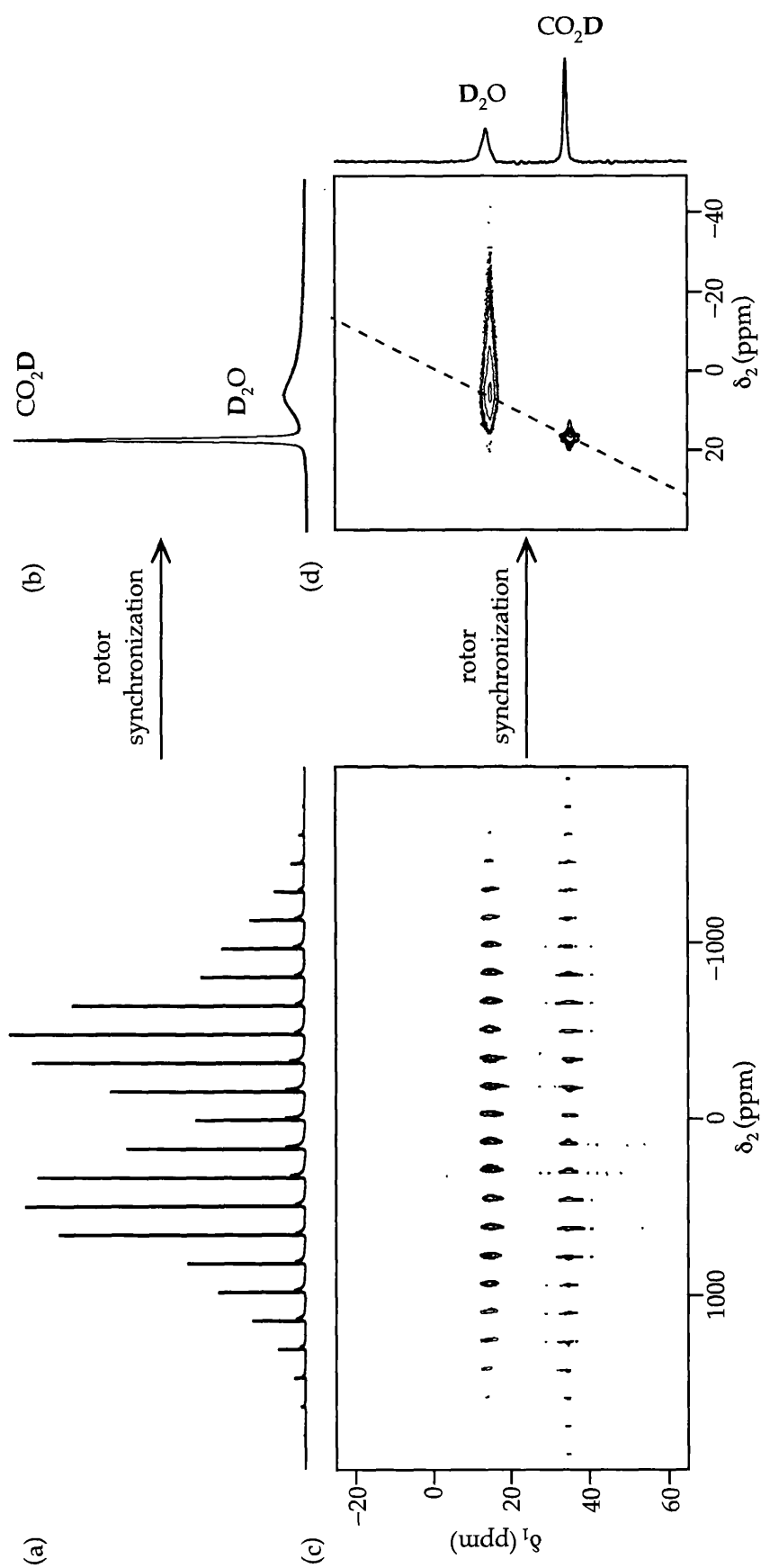


Figure 4.6:  $^2\text{H}$  NMR spectra of oxalic acid dihydrate- $d_6$ . One-dimensional  $^2\text{H}$  MAS NMR spectra recorded using (a) conventional and (b) rotor-synchronized acquisition. Two-dimensional  $^2\text{H}$  MAS NMR spectra (and  $\delta_1$  projection) recorded using rotor-synchronized acquisition in the  $t_1$  period and using (c) conventional and (d) rotor-synchronized acquisition in the  $t_2$  period. The dashed line in (d) shows the axis  $\delta_1 = 2\delta_2$  along which all the two-dimensional peaks lay. 128 transients were acquired for each of 512 rotor-synchronized  $t_1$  increments in both two-dimensional experiments. A relaxation interval of 0.15 s was used.

When rotor-synchronized in both  $\delta_1$  and  $\delta_2$ , the spectrum in Fig. 4.6d is obtained, showing only one peak per  $^2\text{H}$  site in this material. As outlined in the Section 4.1, the higher sensitivity and the ease with which linewidths are measured when the experiment is rotor-synchronized in both dimensions, makes this version of the experiment a much more appealing one to use for investigating molecular-scale dynamics.

It is immediately obvious from Figs. 4.6b and 4.6d, that the linewidth of the water deuteron peak in the single-quantum ( $\delta_2$ ) dimension is much greater than that in the double-quantum ( $\delta_1$ ) dimension. There are several mechanisms that could cause the MAS line to broaden:  $B_0$  inhomogeneity, heterogeneity of the sample, dipolar couplings, etc., but all these should not only effect both transitions, but the  $^2\text{H}$  double-quantum transition should be twice as sensitive as the single-quantum transition. These are clearly not the dominant mechanisms present in our experiment and for this reason it was concluded that the greater single-quantum MAS linewidth for the water peak is evidence of motion on the  $\mu\text{s}$ -timescale as described in Section 4.2. This deduction is supported by the fact that the molecular dynamics due to the  $180^\circ$  flips of the water molecule about the  $C_2$  axis is well known in this type of hydrate [4.32].

In contrast, the carboxyl peak linewidth is virtually identical in both dimensions of the two-dimensional double-quantum MAS spectrum indicating an absence of  $\mu\text{s}$ -timescale dynamics for this deuteron. Further confirmation that the  $^2\text{H}$  site in the water molecule experiences rapid

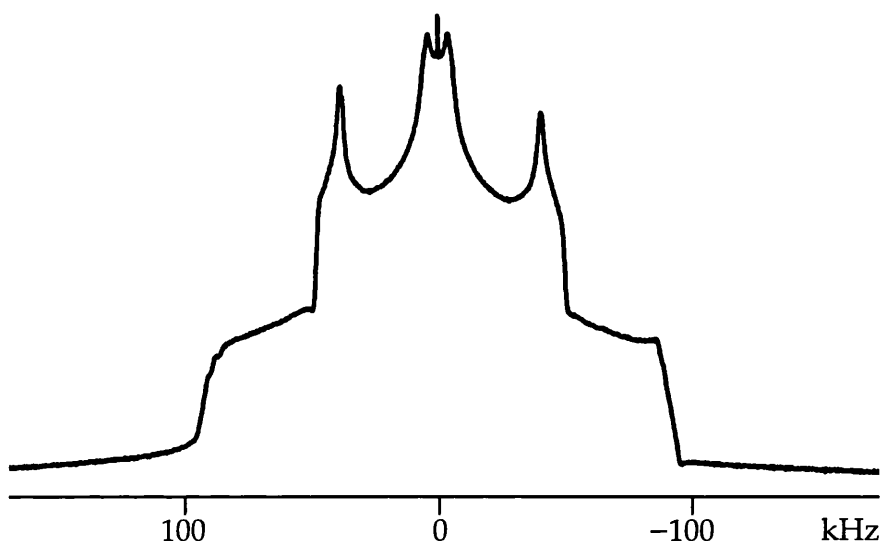


Figure 4.7 (e) One-dimensional static  $^2\text{H}$  NMR spectrum of oxalic acid recorded using the Exorcycled quadrupolar-echo pulse sequence. A relaxation interval of 0.15 s was used.

molecular motion is shown in the quadrupolar-echo spectrum of this material shown in Fig. 4.7 (Sections 2.6.2, 3.3 and 4.4), where the static  $^2\text{H}$  NMR spectrum is clearly made up of the sum of two Pake doublets, one of which is motionally averaged.

Variable-temperature experiments were conducted to investigate how linewidths of the respective peaks change as the temperature is raised and hence the rate constant  $k$  increased. Table 4.1 shows the results obtained as temperature was increased from room temperature to 350 K. It must be noted that when spinning at 10 kHz, the temperature experienced by the spinning sample is approximately 5 K more than the temperature displayed by the spectrometer, which is that of the bearing gas used to spin the sample. The temperatures quoted in this chapter try to reflect the true temperature the material is experiencing in the rotor by adding 5 K correction (for 10 kHz MAS) to the bearing gas reading.

The linewidth measurements in Table 4.1 show that the single-quantum D<sub>2</sub>O peak linewidths narrow as the temperature increases. However, they still remain significantly larger than their counterparts in the double-quantum dimension. As temperature increases, the difference between the  $\delta_2$  and the  $\delta_1$  dimension linewidths of the D<sub>2</sub>O site decrease, with those at the highest temperature differing by only ~100 Hz. An Arrhenius-type plot of the natural log of the single-quantum linewidth values of the D<sub>2</sub>O site against the inverse of the temperature, suggests an activation energy of 27.7 kJ mol<sup>-1</sup>, a value which is consistent with activation energy values determined previously from solid-state <sup>1</sup>H NMR [4.33]. In contrast, the carboxyl peak single- and double-quantum linewidths remained very similar for every given temperature, but increased steadily as the temperature was raised. This implies that even in the absence of reorientational dynamics on the  $\mu$ s-timescale for this

Table 4.1: Carboxyl (COOD) and water (D<sub>2</sub>O) deuteron linewidths obtained from rotor-synchronized two-dimensional double-quantum MAS NMR experiments run at various temperatures.

Temperature / K	Linewidth at half-height / Hz			
	COOD		D <sub>2</sub> O	
	$\delta_2$	$\delta_1$	$\delta_2$	$\delta_1$
300	59	49	900	127
310	59	59	610	127
320	68	78	450	156
330	112	117	385	186
340	210	205	385	244
350	390	400	420	312

deuterium site, the increase in temperature is inducing a change in the rate of the dynamic process taking place in the system, and consequently broadening the carboxyl lines in both direct and indirect dimensions.

This process can be explained by the fact that the dominant intermolecular interactions in oxalic acid dihydrate are the hydrogen bonds [4.34] that connect the proton on each carboxyl group to a water molecule. Zheng *et al.* [4.32] found that hydrogen-bonded sites are associated with rapid proton exchange. They used partly deuterated oxalic acid to illustrate the proton exchange taking place in this material,



Since the rate of the proton exchange increases as the temperature increases, the rise in temperature changes the rate of  $^2\text{H}$  exchange between the carboxyl and the water deuterons, which must affect the rate of the dynamic reorientation of the water molecule. According to the spin-echo model (refer to Fig. 4.4), at room temperature, the water molecule in oxalic acid dihydrate- $d_6$  has a rate constant  $k$  of the order of  $10^7 \text{ s}^{-1}$ , which keeps increasing as the single-quantum linewidth decreases. On the other hand, the COOD site is virtually stationary at room temperature but its rate constant increases steadily to the order of  $10^4 \text{ s}^{-1}$  as the temperature increases to 350 K.

#### 4.6.3 Sodium tetrathionate dihydrate- $d_4$

As shown in Fig. 4.4, one of the predictions of the spin-echo model of motional broadening under MAS is that the linewidth can exceed the  $^2\text{H}$  MAS rate with the result that no peaks are observed in the MAS NMR spectrum. Sodium tetrathionate dihydrate- $d_4$ , ( $\text{Na}_2\text{S}_4\text{O}_6 \cdot 2\text{D}_2\text{O}$ ) (deuterated from sodium tetrathionate dihydrate,  $\geq 98\%$  SIGMA) is an example of such behaviour.  $\text{Na}_2\text{S}_4\text{O}_6 \cdot 2\text{D}_2\text{O}$  is expected to yield one peak, arising from the deuterons in the water of hydration, in its  $^2\text{H}$  MAS NMR spectrum. However, when this spectrum is acquired at room temperature, the peak is too broad to be visible. Figure 4.8a shows  $^2\text{H}$  MAS NMR spectra of this material recorded at 297, 330, and 350 K. It is clear that at 297 K there is very little intensity in the MAS spectrum. The small sidebands that do appear arise because although most crystallites in the powder have large frequency jumps ( $\Delta\nu_{\text{jump}}$ ), there is also a small fraction of crystallites oriented such that they have small frequency jumps and hence exhibit narrow single-quantum MAS linewidths. The sharp spike in the middle of the static powder pattern shown in Fig. 4.9 confirms this observation. As the temperature and hence rate constant are increased, the linewidths of the MAS peaks get narrower and therefore the sideband intensity starts increasing.

Variable-temperature experiments were also performed using the  $^2\text{H}$  two-dimensional double-quantum MAS NMR experiment pulse sequence. Figure 4.8b shows the fully rotor-synchronized double-quantum MAS spectrum of  $\text{Na}_2\text{S}_4\text{O}_6 \cdot 2\text{D}_2\text{O}$  recorded at 330 K. Similar to

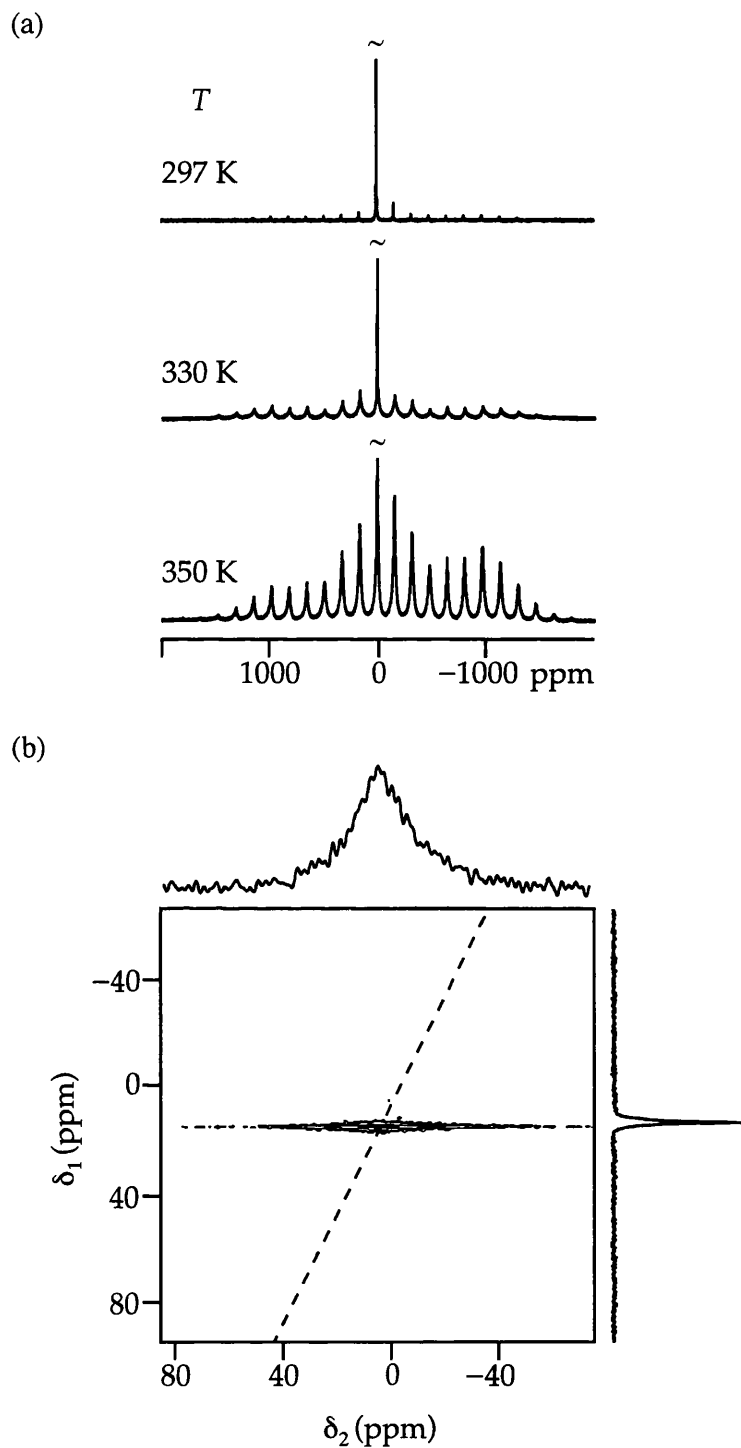


Figure 4.8:  $^2\text{H}$  NMR of sodium tetrathionate dihydrate- $d_4$ . (a) Conventional  $^2\text{H}$  MAS spectra at temperatures of 297, 330 and 350 K, showing narrowing of motionally broadened sidebands as  $T$  increases. (b) Two-dimensional  $^2\text{H}$  double-quantum MAS NMR spectrum (and  $\delta_1$  and  $\delta_2$  projections) recorded at 330 K, with 640 transients acquired for each of 256 rotor-synchronized  $t_1$  increments. The dashed line in (b) shows the axis  $\delta_1 = 2\delta_2$ . A relaxation interval of 0.2 s was used.

what has already been seen from the oxalic acid dihydrate- $d_6$  results, the water peak has a very broad linewidth in the single-quantum ( $\delta_2$ ) dimension while the peak is narrower in the double-quantum ( $\delta_1$ ) dimension. As shown by Fig. 4.8b, this material is an extreme example of motional broadening under MAS, with the single-quantum full linewidth at half height (2100 Hz) at a temperature of 330 K, being almost two orders of magnitude broader than the double-quantum linewidth (45 Hz). As the temperature is increased, the single-quantum linewidth decreases, while the double-quantum linewidth increases slightly as seen from Table 4.2.

The rate constant  $k$  for the water molecule in sodium tetrathionate dihydrate- $d_4$  can be fairly easily estimated by referring to the spin-echo model in Fig. 4.4, and reading the value of  $k$  for the point where the MAS linewidth gets narrow enough for the peaks to start being visible again, e.g., at 330 K,  $\log_{10}(k/s^{-1}) \approx 6.5 - 7.5$ . This particular material was studied

Table 4.2: Water ( $D_2O$ ) deuteron linewidths in  $Na_2S_4O_6 \cdot 2D_2O$  obtained from rotor-synchronized two-dimensional double-quantum MAS NMR experiments run at various temperatures.

Temperature / K	Linewidth at half-height / Hz	
	$\delta_2$	$\delta_1$
297	-	-
320	-	-
330	2100	44
340	1950	51
350	1560	59

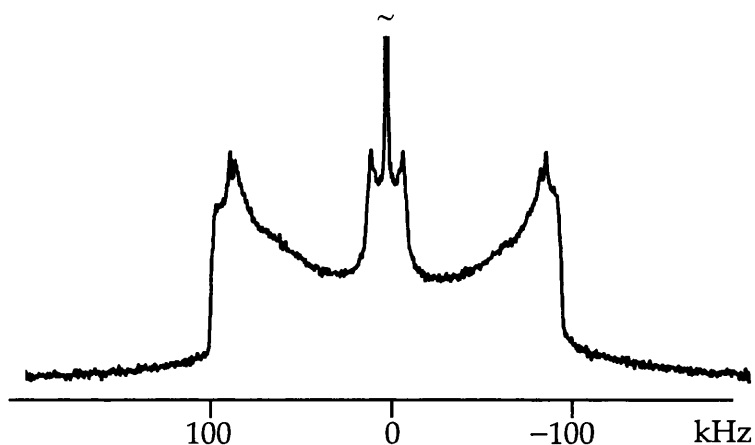


Figure 4.9: One-dimensional static  $^2\text{H}$  NMR spectrum of sodium tetrathionate dihydrate- $d_4$ , recorded using the Exorcypled quadrupolar-echo pulse sequence. A relaxation interval of 0.2 s was used.

in further depth by Thrippleton *et al.* in Ref. 4.25, where the rate constant predicted by the spin-echo model was compared to that obtained by fitting the single-quantum lineshape using exact numerical simulations as well as that obtained by the conventional method of fitting static lineshapes. The activation energy for the reorientation of the water molecule calculated using results from the spin-echo model and plotting an Arrhenius-type plot, was found to be  $31.1 \text{ kJ mol}^{-1}$ .

The  $\text{Na}_2\text{S}_4\text{O}_6 \cdot 2\text{D}_2\text{O}$  Pake doublet is shown in Fig. 4.9. As expected, the lineshape differs greatly from the conventional Pake doublets seen so far. Referring back to Fig. 4.3, one can very easily associate this peculiar lineshape with the one in the mid- $\mu\text{s}$  regime, which in turn confirms the result obtained from the spin-echo model.

#### 4.6.4 Calcium sulfate dihydrate- $d_4$

$\text{CaSO}_4 \cdot 2\text{D}_2\text{O}$  (deuterated from calcium sulfate hemihydrate  $\geq 99\%$  SIAL), better known as gypsum, consists of one environmentally distinct  $^2\text{H}$  site, the  $^2\text{H}$  in the water molecule. After the results discussed in Sections 4.6.2 and 4.6.3, one would expect that one peak, broad in  $\delta_2$  and narrow in  $\delta_1$  would be observed in the fully rotor-synchronized two-dimensional  $^2\text{H}$  double-quantum MAS spectrum of this material. As seen in the spectrum in Fig. 4.10a, this is not the case. Instead, a peak with very similar linewidths in both dimensions was obtained.

The linewidths at half-height for the water peak in gypsum at various temperatures are listed in Table 4.3. Despite the remarkable similarity, the linewidths of both peaks narrow as temperature increases,

Table 4.3: Water ( $\text{D}_2\text{O}$ ) deuteron linewidths in  $\text{CaSO}_4 \cdot 2\text{D}_2\text{O}$  obtained from rotor-synchronized two-dimensional double-quantum MAS NMR experiments run at various temperatures.

Temperature / K	Linewidths / Hz	
	$\text{D}_2\text{O}$	
	$\delta_2$	$\delta_1$
230	166	132
310	132	127
320	117	122
330	103	112
340	102	98
350	98	98

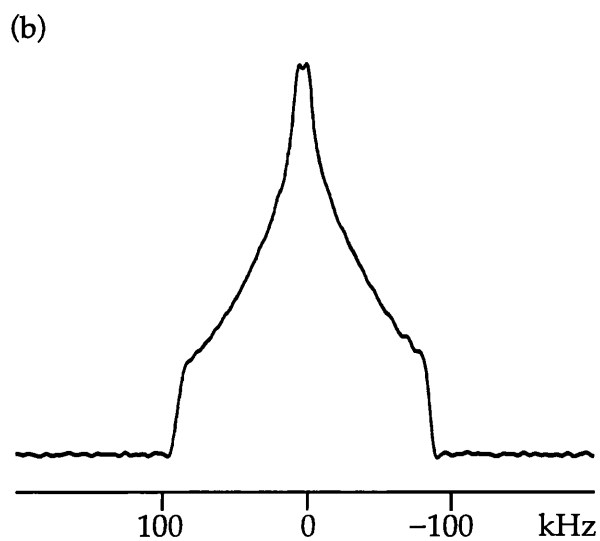
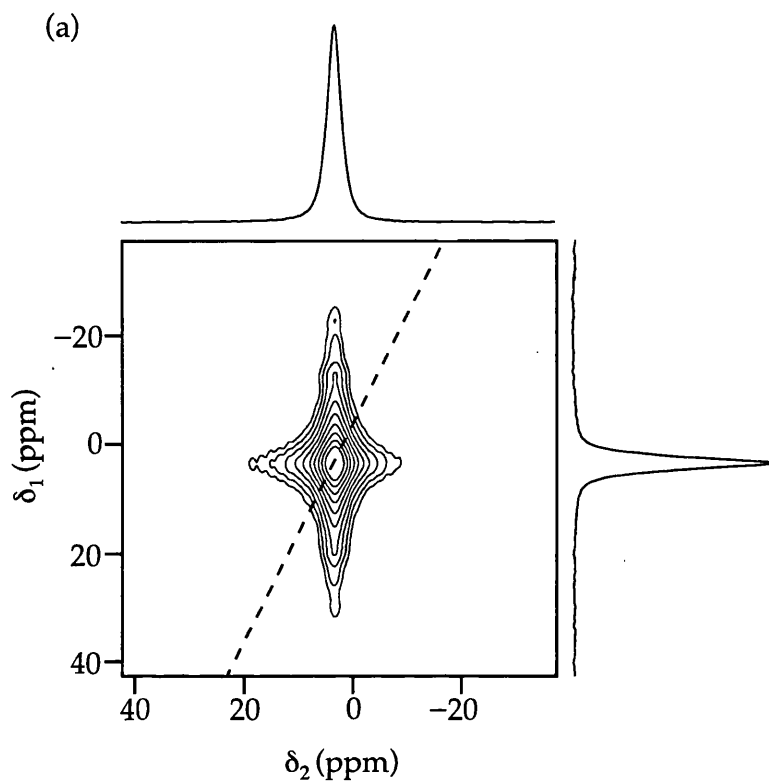


Figure 4.10: (a) Two-dimensional  $^2\text{H}$  double-quantum MAS NMR spectrum (and  $\delta_1$  and  $\delta_2$  projections) of calcium sulfate dihydrate- $d_4$ , recorded with 160 transients acquired for each of 256 rotor-synchronized  $t_1$  increments. (b) One-dimensional static  $^2\text{H}$  NMR spectrum recorded using the Exorcypled quadrupolar-echo pulse sequence. A relaxation interval of 0.5 s was used.

implying that the rate constant  $k$  for the dynamics in this material must lie on the right-hand side of the  $\log_{10}$ - $\log_{10}$  plot in Fig. 4.4. In addition, the Pake doublet shown in Fig. 4.10b unmistakably shows a motionally-narrowed static lineshape (refer to Fig. 4.3), implying that the water molecule in gypsum is undergoing very fast molecular dynamics. After plotting an Arrhenius-type plot for this material, an activation energy of  $10.5 \text{ kJ mol}^{-1}$  was obtained.

#### 4.6.5 Poly(methyl methacrylate- $d_3$ ) – PMMA

This fully deuterated synthetic polymer was donated to the group by Mr Adrian Brunson (Bruker, UK). Each structural unit of PMMA, shown in Fig. 4.11a, consists of three distinct  $^2\text{H}$  sites: a methylene ( $\text{CD}_2$ ) group on the backbone of the polymer, as well as a methyl ( $\text{CD}_3$ ) group

Table 4.4:  $\text{OCD}_3$ ,  $\text{CD}_2$  and  $\text{CD}_3$  deuteron linewidths in PMMA obtained from rotor-synchronized two-dimensional double-quantum MAS NMR experiments run at various temperatures.

Temperature / K	Linewidths / Hz					
	$\text{OCD}_3$		$\text{CD}_2$		$\text{CD}_3$	
	$\delta_2$	$\delta_1$	$\delta_2$	$\delta_1$	$\delta_2$	$\delta_1$
296	98	78	337	131	137	151
310	103	63	381	131	142	127
320	107	73	420	127	151	112
330	122	73	450	127	156	107
340	137	68	527	122	175	98
350	156	63	576	117	176	98

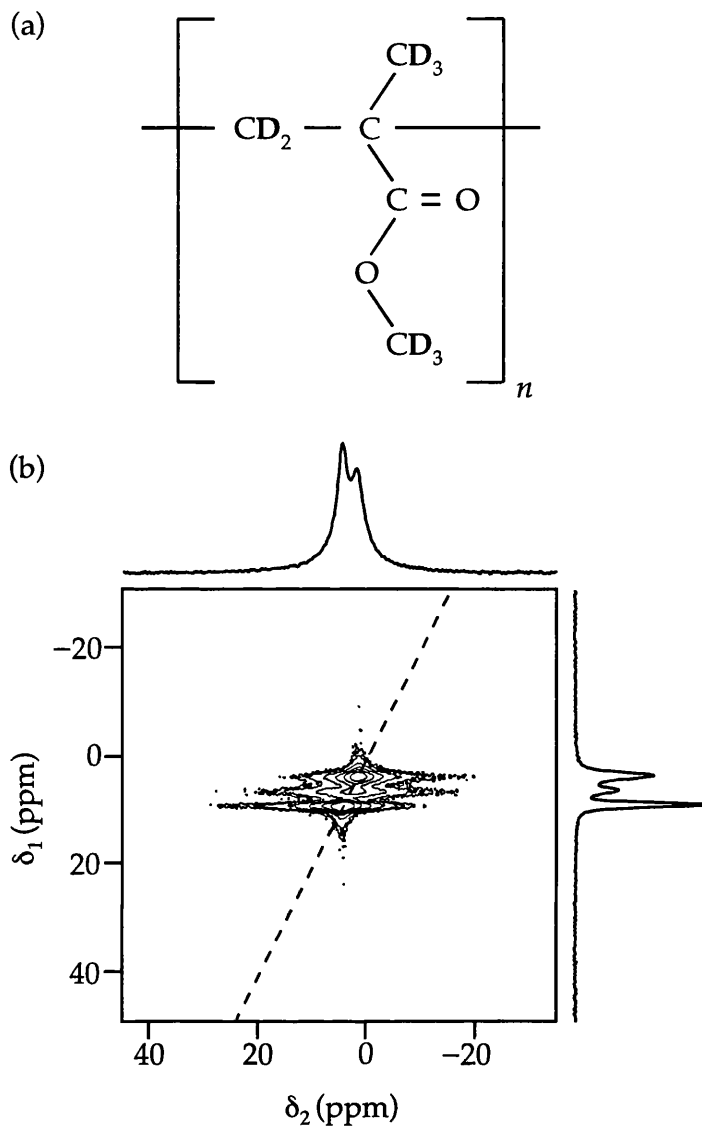


Figure 4.11: (a) Chemical structure of poly(methyl methacrylate- $d_8$ ). (b) Two-dimensional  $^2\text{H}$  double-quantum MAS NMR spectrum of PMMA recorded at  $T = 330$  K using 96 transients acquired for each of 256 rotor-synchronized  $t_1$  increments. The dashed line in (b) shows the axis  $\delta_1 = 2\delta_2$ . A relaxation interval of 3 s was used.

and a methoxy ( $\text{OCD}_3$ ) group as sidechains. The two-dimensional double-quantum MAS NMR spectrum of PMMA is shown in Fig. 4.11b. The single-quantum ( $\delta_2$ ) projection of the two-dimensional spectrum reveals just two resolved peaks. However, the double-quantum ( $\delta_1$ ) projection in Fig. 4.11b, reveals three peaks, one for each distinct

deuterium site in the polymer. The increased resolution in the  $\delta_1$  dimension originates, partly from the doubling of the chemical shift dispersion in the double-quantum spectrum, but mainly from the absence of motional-broadening effects in the double-quantum transition peaks.

The increased resolution in  $\delta_1$  makes it possible to extract  $\delta_2$  cross-sections, corresponding to the single-quantum MAS spectra of each  $^2\text{H}$  site in PMMA, and hence accurately measure the linewidths of the three peaks in both the single and double-quantum dimensions. As seen from Table 4.4 and Fig. 4.12, the greatest linewidth change is observed for the  $\text{CD}_2$  deuterons on the polymer backbone, where the broadness of the single-quantum linewidths (337–576 Hz) compared to the double-quantum linewidths (131–117 Hz) over the same temperature range indicates  $\mu\text{s}$ -timescale dynamics. As the temperature is raised, the linewidths of the other two groups broaden as well, implying that all the sites in PMMA experience molecular dynamics to some extent. In addition, it can be concluded that the  $\text{CCD}_3$  and  $\text{OCD}_3$  groups have very similar type and magnitude of dynamics. This prediction is also confirmed by the static lineshape of PMMA shown in Fig. 4.13. Only two distinct Pake doublets are visible in the static pattern (simulations of which are also shown), implying that two of the sites are undergoing very similar dynamics and hence their respective Pake doublets overlap. The spin-echo model predicts a rate constant  $k$  of around  $10^4 \text{ s}^{-1}$  for the kind of linewidths obtained for the  $\text{CD}_2$  site in PMMA and an Arrhenius-type analysis of the single-quantum linewidths suggests an activation energy of  $8.6 \text{ kJ mol}^{-1}$ .

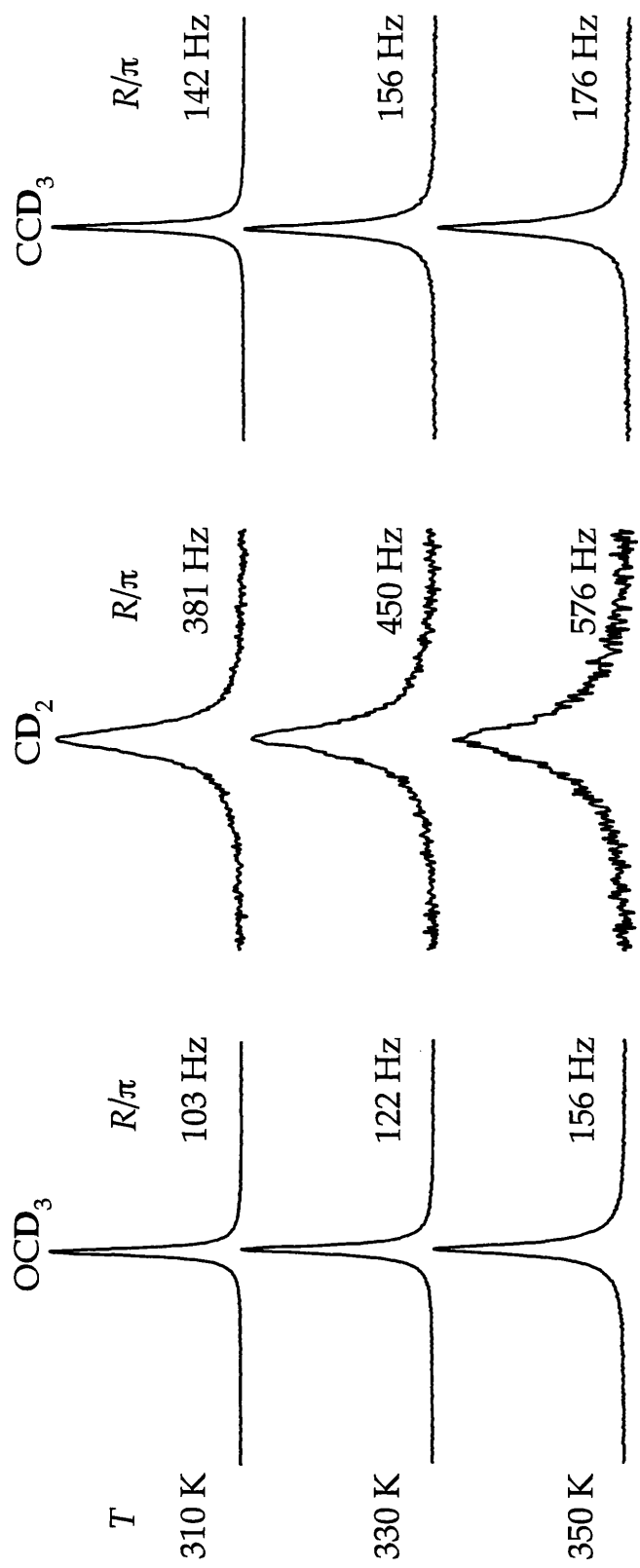


Figure 4.12:  $\delta_2$  cross-sections through the three two-dimensional peaks in Fig. 4.11 (b) and full linewidths at half height at temperature of 310, 330 and 350 K.

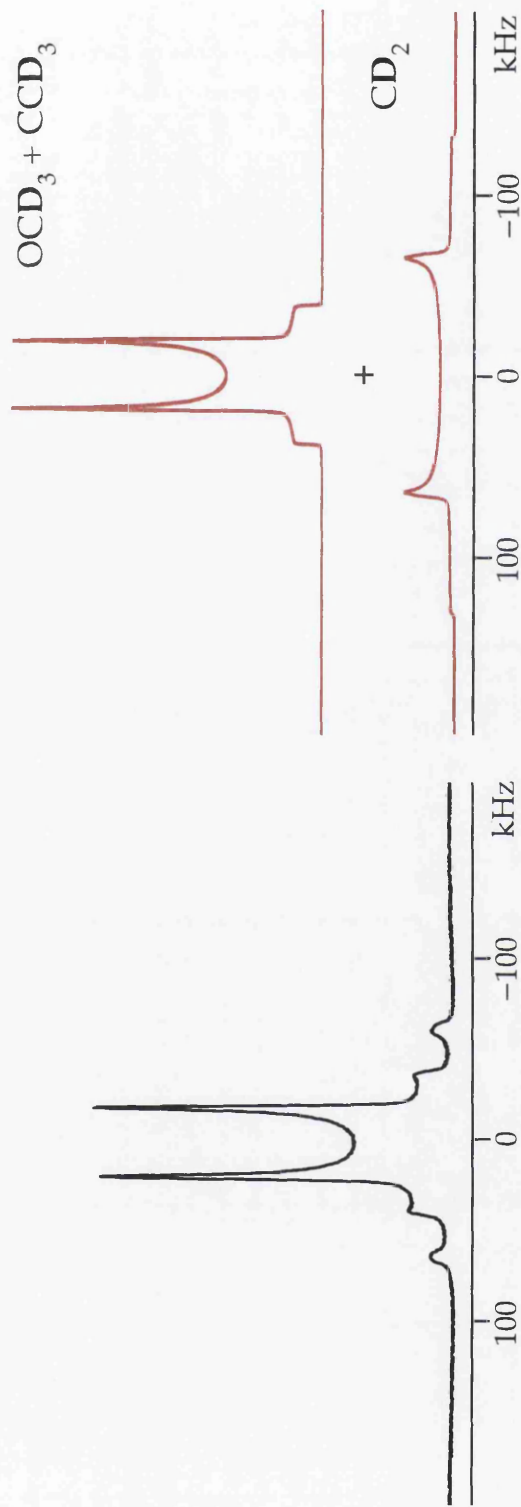


Figure 4.13: One-dimensional static  $^2\text{H}$  NMR spectrum recorded using the Exor-cycled quadrupolar-echo pulse sequence and the simulation of the two Pake doublets marked  $\text{OCD}_3 + \text{CCD}_3$  and  $\text{CD}_2$  respectively, which form the PMMA static lineshape. A relaxation interval of 3 s was used.

#### 4.6.6 Hydroxyl-clinohumite- $d_8$

Deuterated hydroxyl-clinohumite,  $4\text{Mg}_2\text{SiO}_4\cdot\text{Mg}(\text{OD})_2$ , was made by Dr Andrew J. Berry (Department of Earth Sciences and Engineering, at Imperial College London). It is a member of the humite group of minerals. Simplistically, its crystal structure can be described as made up of blocks of forsterite ( $\text{Mg}_2\text{SiO}_4$ ) and intervening layers of brucite ( $\text{Mg}(\text{OH})_2$ ), also known as the hydrated layer. Various analytical techniques such as x-ray diffraction and neutron powder diffraction have already been used to study the crystal structure of this material, and the latter technique has made it possible to accurately determine the hydrogen positions in this humite structure, as this is crucial to understanding the stability of the hydrated layer, which relies on extensive hydrogen bonding network formed between the hydroxyl-clinohumite protons and the adjacent oxygen atoms [4.35].

Figure 4.14a shows four possible hydrogen positions, two marked D1 and another two marked D2; however, only one of each kind of deuteron is present in hydroxyl-clinohumite, i.e., there is always one vacant D1 and D2 position for every filled D1 and D2 site. Berry *et al.* [4.35] explain that the two D1 sites marked on Fig. 4.14a cannot be occupied at the same time, as their close proximity would destabilize the structure. The same applies to the two D2 sites. This means that when one D1 (or D2) position is filled, the next nearest D1 (or D2) position must be empty.

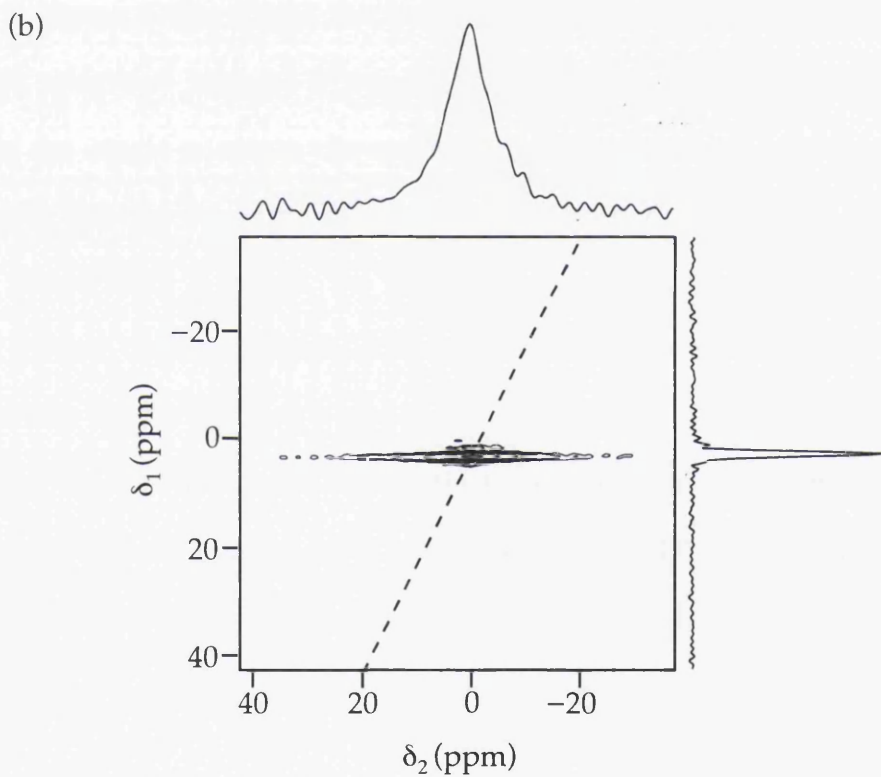
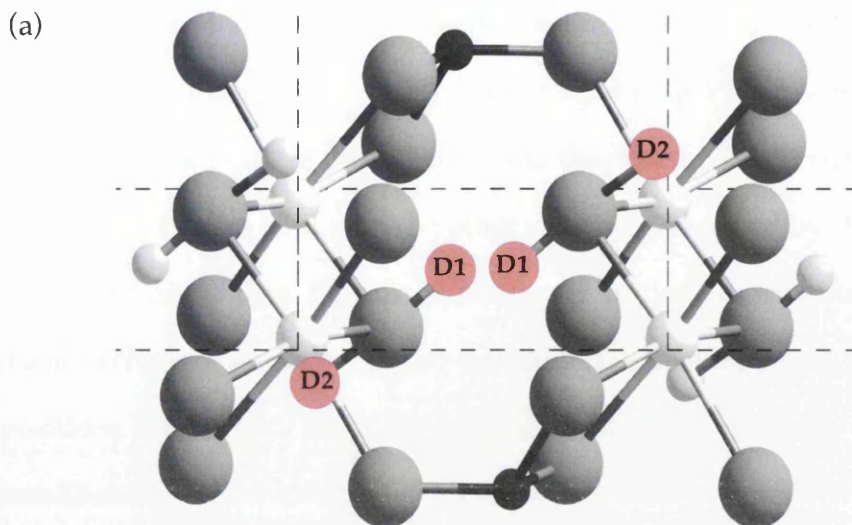


Figure 4.14: (a) Crystal structure of hydroxyl-clinohumite- $d_8$ . (b) Two-dimensional  $^2\text{H}$  double-quantum MAS NMR spectrum of hydroxyl-clinohumite- $d_8$  recorded at  $T = 302$  K, using 160 transients acquired for each of 256 rotor-synchronized  $t_1$  increments. The dashed line in (b) shows the axis  $\delta_1 = 2\delta_2$ .

$^{17}\text{O}$  satellite-transition MAS NMR spectra revealed the presence of dynamics within the structure [4.21]. The  $^2\text{H}$  double-quantum MAS NMR experiment of the deuterated material was therefore used to determine whether the dynamics could also be observed and quantified by  $^2\text{H}$  NMR spectroscopy. Dynamics in this structure is not at all surprising as chemical exchange between the two available D1 positions and the two D2 positions can happen fairly easily because of the very similar energy of these D sites.

Figure 4.14b shows the two-dimensional double-quantum MAS NMR spectrum. Internal dynamics is evidently present in this sample since the single-quantum dimension linewidth (600 Hz) is very much broader than the linewidth of the double-quantum dimension (70 Hz). As the temperature is raised, the single-quantum peak narrows implying that the rate constant  $k$  at which the deuterium is moving lies on the right hand side of the  $\log_{10}$ - $\log_{10}$  plot shown in Fig. 4.4. Neutron diffraction studies show evidence for two distinct deuterium sites, however NMR can only resolve one  $^2\text{H}$  peak, implying that the D1 and D2 sites are crystallographically very similar and NMR cannot distinguish amongst them.

The Pake doublet, shown in Fig. 4.15, does not show evidence of molecular dynamics taking place in this material as it is not a motionally-averaged static lineshape. As in the MAS spectrum, a second distinct  $^2\text{H}$  site is not resolved. It is clear that this material is undergoing dynamic behaviour, which is yet not understood, and further studies need to be

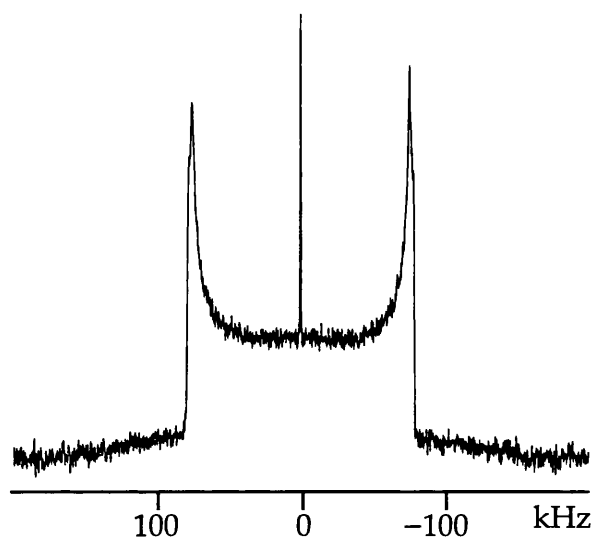


Figure 4.15: One-dimensional static  $^2\text{H}$  NMR spectrum recorded using the Exorycled quadrupolar-echo pulse sequence.

carried out. One possible way of trying to understand the dynamic behaviour of this material is by synthesizing deuterated titanium-substituted forms of clinohumite dihydrate. Substituting the Mg atom with a Ti atom will result in only one possible D1 and one possible D2 position and hence the material should be free of internal motion. One would expect that a two-dimensional double-quantum MAS NMR spectrum of such compound would yield a spectrum with its single-quantum and double-quantum linewidths very similar to one another, suggesting that any broadening observed in the peaks does not arise as a result of internal dynamics in the material.

## 4.7 Conclusions

It has been shown that very strong broadening can occur in  $^2\text{H}$  MAS NMR spectra when  $\mu\text{s}$ -timescale dynamics are present in the material. In this work,  $^2\text{H}$  single-quantum linewidths are compared with the corresponding double-quantum linewidths, as line-broadening due to motion is either absent or greatly reduced in the latter. It has been shown that the inherently narrow lines in the double-quantum dimension combined with a doubling of the chemical shift dispersion in the double-quantum spectrum compared with the single-quantum dimension may make it possible for overlapping peaks in the  $^2\text{H}$  MAS NMR spectra to be resolved (refer to Fig. 4.11b and Fig. 4.12). This increase in resolution makes it possible to measure the linewidth of the peaks in both single- and double-quantum dimensions, including those originally not visible due to overlap in the direct dimension.

It was shown that the motionally-induced line-broadening in MAS spectra can be described analytically by modelling MAS as a series of spin-echoes. Thrippleton *et al.* validated this simple model by comparing it with exact numerical simulations and the conventional method of static lineshape fitting using the quadrupolar-echo technique. Unfortunately, this method fails to provide any information about the mechanism of the dynamics observed. This information is usually obtained by studying the static  $^2\text{H}$  lineshape or the MAS sidebands, hence just by not rotor synchronizing in the  $\delta_2$  dimension, the lost information will be reinstated.

# Effects of spin diffusion on spin-lattice relaxation in solid-state $^2\text{H}$ MAS NMR spectroscopy

---

### 5.1 Introduction

The spin-lattice relaxation time  $T_1$  is a very important parameter in all NMR experiments. The  $T_1$  time is one of the first parameters one needs to investigate before performing any NMR experiments, as this is a measure of the time that the population of spins in a material takes to go back to its equilibrium position after this is disturbed by say, a radiofrequency pulse. If not enough time is allowed for all the magnetization to relax back to equilibrium, the sensitivity of the experiment is affected, and hence the spectra obtained would show peaks less intense than expected. In addition, the  $T_1$  time can give an insight of important dynamic and structural properties of the materials investigated.

While measuring the spin-lattice relaxation time of deuterated materials as a routine procedure, puzzling results were observed. It was

found that for deuterated materials containing more than one dynamically different deuterium site (e.g. CD – rigid and CD<sub>3</sub> – mobile), the  $T_1$  time measured when the material was investigated under static conditions was different than that obtained when it was spinning. This discrepancy instigated further investigation and hence this study.

It is well known that solid-state NMR experiments are often hampered by long  $T_1$  times when compared with liquid-state experiments. This is due to a lack of mobility present in solids when compared to the tumbling that takes place within a liquid [5.1]. However, within a solid material one would also expect a variety of  $T_1$  times as some sites within a solid can be more rigid than others. A rigid site such as the –CD or –ND groups, would have a far longer  $T_1$  relaxation time than a non-rigid one (e.g., –CD<sub>3</sub> or –ND<sub>3</sub><sup>+</sup> groups) in the solid-state. Indeed this was found to be the case, however, when the materials were investigated under spinning conditions, the long  $T_1$  times expected were often not present.

In this chapter, this observation will be discussed in light of earlier work done in this field, namely by Alla *et al.* [5.2] and Gan and Robyr [5.3]. They explain the observed increase in <sup>2</sup>H  $T_1$  times when NMR spectra are recorded under MAS, using the phenomenon of spin diffusion (refer to Section 2.5.2) and  $n = 0$  rotational resonance.

## 5.2 Theoretical Background

### 5.2.1 Spin-lattice relaxation time $T_1$

The time constant  $T_1$  is also known as the longitudinal or spin-lattice relaxation time. It is a measure of the time that it takes for the z-magnetization of the spin energy levels to return to thermal equilibrium after a pulse has been applied. In other words, if at any time the longitudinal magnetization is not equal to the equilibrium nuclear magnetization,  $M_z(0)$ , it will approach it in  $T_1$  seconds. Thus, if at time  $t = 0$  the longitudinal magnetization is  $M_z(0)$ , the z-magnetization at time  $t$  is given by:

$$(M_z(t) - M_0(t)) = (M_z(0) - M_0(0))\exp(t/T_1) . \quad (5.1)$$

Equation (5.1) describes the behaviour of the macroscopic magnetization produced by a large number of spins. At the level of an individual nucleus, the magnetic moment can be parallel to the applied field (the lower energy or ground state), or antiparallel to the external field (excited state). The transition from the ground state to the excited state requires the absorption of energy at the Larmor frequency. Similarly, the transition from the excited state to the ground state (relaxation) requires a stimulating radiofrequency field, which can be provided by the randomly fluctuating fields within the environment that the nucleus experiences. This environment is called the lattice, hence the name spin-lattice relaxation. The randomly fluctuating fields experienced by the nucleus

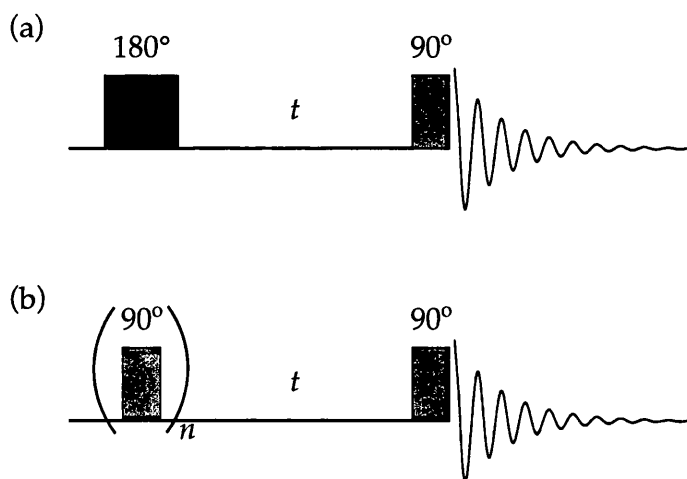


Figure 5.1: (a) Inversion-recovery and (b) saturation recovery pulse sequence.

are caused by the environment it is in. Thus, the rate of the dynamics experienced by the spins or surrounding molecules is a critical component of  $T_1$ . Hence, in a solid that consists of several environmentally inequivalent sites, each nucleus could experience a different relaxation rate constant depending on its position and surroundings.

### 5.2.2 Determination of spin-lattice relaxation times

In this chapter, the  $T_1$  relaxation time is going to be measured using either the 'inversion-recovery method', or the 'saturation-recovery method'. The former, whose pulse sequence is shown in Fig. 5.1a, consists of a  $180^\circ$  pulse that aligns magnetization along the  $-z$ -axis, followed by a variable time,  $t$ , during which the inverted magnetization recovers back to equilibrium, and finally a  $90^\circ$  pulse that gives a measure of the amount of magnetization present. This experiment requires a long preparation

period compared to the  $T_1$  so as to ensure that the spins have enough time to reach thermal equilibrium before the  $180^\circ$  pulse inverts the magnetization. Usually, an interval of around four to five times the magnitude of an estimate of the  $T_1$  of the material is used. This makes the inversion-recovery experiment a very time consuming experiment, especially when dealing with extremely rigid materials.

In contrast, the saturation-recovery method, shown in Fig. 5.1b, involves a series of  $90^\circ$  pulses applied as close as possible to each other to ensure saturation of the spins and then, in the same manner as the previous method, a variable recovery interval  $t$  followed by a  $90^\circ$  pulse is used to monitor the amount of magnetization. Consequently, this experiment does not need a long relaxation interval to allow for thermal equilibrium to be reached and hence is preferred when measuring longer relaxation times [5.4].

### 5.2.3 Rotational resonance

Rotational resonance is a phenomenon that occurs in samples containing homonuclear dipolar-coupled spin pairs spinning at a speed that meets the condition:

$$\Delta\nu^{\text{iso}} = n\nu_{\text{MAS}}, \quad (5.2)$$

where  $\Delta\nu^{\text{iso}}$  is the difference in isotropic chemical shifts,  $\nu_{\text{MAS}}$  is the MAS rate and  $n$  is an integer. When this condition is met, the dipolar coupling that is originally removed when the sample is spun is reintroduced and

the otherwise sharp resonance lines broaden. In this study, we use spin diffusion (see Section 2.5.2) [5.5], to describe the polarization transfer that occurs when the chemical shift differences between the deuterium sites are similar enough hence allowing their peaks to overlap, which introduces intramolecular dipolar coupling back even though the sample is being spun. Under these conditions, the individual spins continually exchange energy with each other through energy-conserving 'flip-flop' terms of the dipolar Hamiltonian as dipolar coupling between the nuclei is no longer quenched [5.2].

This phenomenon was first documented by Andrew *et al.* [5.6], where it was observed that despite spinning a solid material at the magic angle, and hence expecting the peaks observed to narrow due to the suppression of dipolar coupling, at certain frequencies of rotation the lines were observed to broaden again. Andrew *et al.* demonstrate this by acquiring  $^{31}\text{P}$  MAS NMR spectra of polycrystalline phosphorus pentachloride. The spectrum obtained, as expected, consisted of two sharp peaks arising from  $\text{PCl}_4^+$  and  $\text{PCl}_6^-$  ions. However, when the spinning rate was increased to equal exactly half the separation between the two well-resolved peaks, the lines broadened. They extrapolated that this trend should be found in spinning solids containing more than one environmentally distinct nucleus, whose resonances are separated by the applied spinning frequencies.

The subject was revisited in the late eighties by Raleigh *et al.* [5.7]. They came across the phenomenon of rotational resonance while

demonstrating the direct detection of  $^{13}\text{C}$ - $^{13}\text{C}$  homonuclear  $J$ -couplings in MAS NMR. In their work, they point out that the linewidth of glucose changes enormously as spinning speed is increased. They also noted that when spinning at 6 kHz, the linewidths of  $^{13}\text{C}$  doubly labelled glucose were always larger than those of its unlabelled counterpart. Raleigh *et al.* explain that this is due to the strong overlap of the shift tensors of the two coupled sites, hence making the dipolar coupling larger than the difference in isotropic shifts and consequently allowing mutual spin flips to take place. However, this is only valid when the condition described by Eq. (5.2) is met. They go on to explain how at this condition, the flip-flop term of the Hamiltonian is reintroduced and hence leads to line broadening. A year later, Raleigh, Levitt and Griffin [5.8] published a paper, which discussed the theory as well as demonstrated the phenomenon of rotational resonance. This paper was followed by another publication, which presented a more detailed discussion of the theory supported by numerical simulations [5.9]. Another study written by Oas *et al.* [5.10] concentrated on the practical side of this phenomenon. In this paper, a combination of MAS and irradiation of a heteronuclear spin system at the Larmor frequency on the spin species was used to reintroduce the coupling. This only happened if the irradiation intensity instigated a match between the spin nutation and the sample rotation. In addition, they also showed that this technique could potentially measure the heteronuclear dipolar coupling constants which are otherwise obscured by shielding tensor anisotropies. Almost simultaneously, Kubo *et al.* [5.11] also observed and discussed what they called, rotational

relaxation resonance in their study of spectral spin diffusion in polycrystalline solids under MAS.

In this chapter, we are going to be looking at  $^2\text{H}$  systems. Rotational resonance conditions where  $n > 0$  are difficult to meet when dealing with  $^2\text{H}$  nuclei because of the small range of  $^2\text{H}$  chemical shifts [5.3], hence this work is going to concentrate on the polarization transfer between deuterium sites at the  $n = 0$  rotational resonance condition. The  $n = 0$  rotational resonance condition is met when two or more chemically different deuterium sites possess the same chemical shift and hence their respective peaks overlap fully, resulting in a MAS NMR spectrum that consists of a series of spinning sidebands each consisting of a single peak.

#### 5.2.4 *The effects of spin diffusion on spin-lattice relaxation – a simple model*

A simple model for the effects of spin diffusion on spin-lattice relaxation can be constructed by considering the longitudinal magnetizations of two sites, A and B, coupled by a relaxation matrix  $\mathbf{R}$ :

$$\begin{pmatrix} \Delta M_A(t) \\ \Delta M_B(t) \end{pmatrix} = \begin{pmatrix} \Delta M_A(0) \\ \Delta M_B(0) \end{pmatrix} \exp\{-\mathbf{R}t\}, \quad (5.3)$$

where  $\Delta M_i(t) = M_i(t) - M_i^{\text{eq}}$  is the deviation of the magnetization of site  $i$  from thermal equilibrium and  $\mathbf{R}$  is given by:

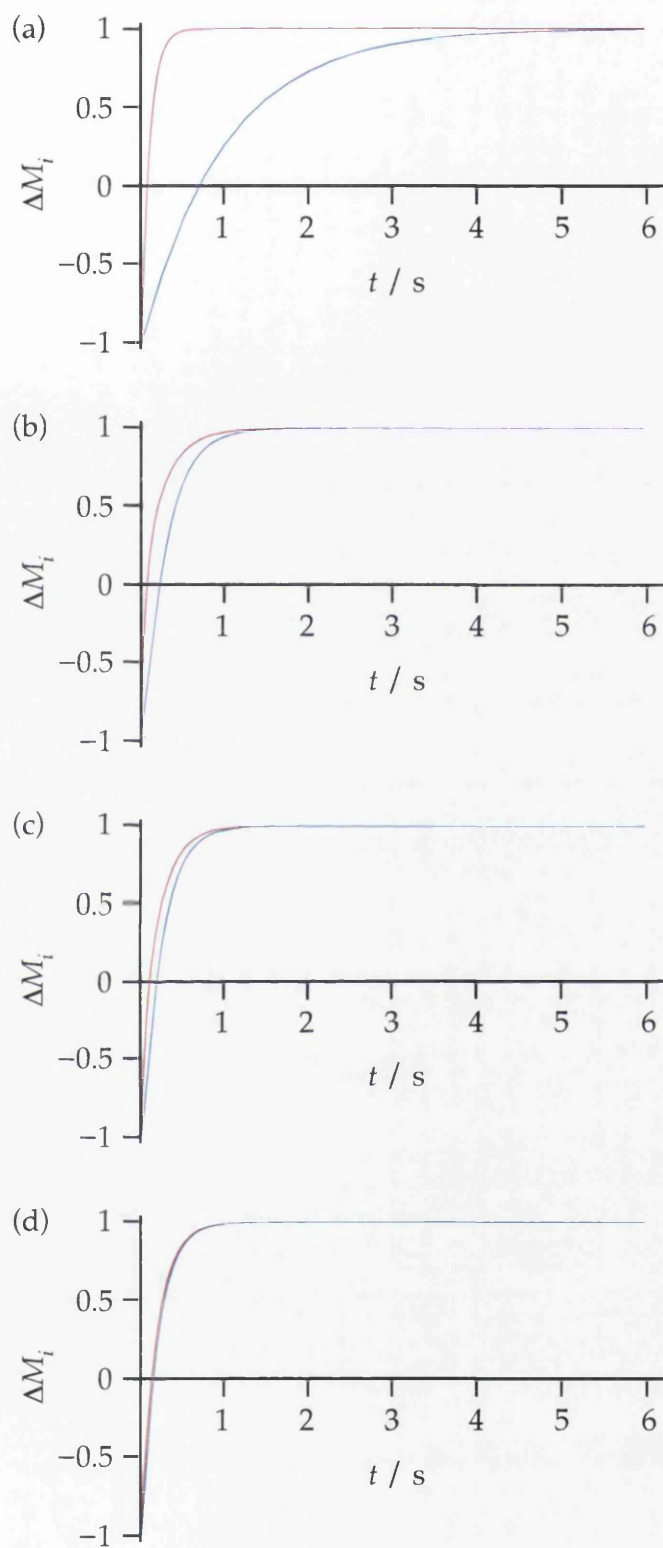


Figure 5.2: Simulations of inversion-recovery experiments of a model compound. The red plot shows a mobile  $^2\text{H}$  site ( $R_f = 10 \text{ s}^{-1}$ ) and the blue plot shows a rigid site ( $R_f = 1 \text{ s}^{-1}$ ). The spin diffusion rate,  $R_{sd}$  between the two sites is 0 in (a) and it increases to  $1 \text{ s}^{-1}$  and  $5 \text{ s}^{-1}$  (b and c) until it is at its strongest at  $10 \text{ s}^{-1}$  in (d).

$$\mathbf{R} = \begin{pmatrix} R_f + R_{sd} & -R_{sd} \\ -R_{sd} & R_s + R_{sd} \end{pmatrix}, \quad (5.4)$$

where  $R_f$  is the rate constant for the fast decay of  $\Delta M_A(t)$  in the absence of spin diffusion,  $R_s$  is the much smaller rate constant for the slow decay of  $\Delta M_B(t)$  in the absence of spin diffusion, and  $R_{sd}$  is the rate constant for spin diffusion between A and B. If spin diffusion is slow ( $2R_{sd} \ll R_f - R_s$ ) then:

$$\begin{aligned} \Delta M_A(t) &= \Delta M_A(0) \exp\{-(R_f + R_{sd})t\}, \\ \Delta M_B(t) &= \Delta M_B(0) \exp\{-(R_s + R_{sd})t\}. \end{aligned} \quad (5.5)$$

$$\begin{aligned} T_{1,A} &= (R_f + R_{sd})^{-1} \approx 1/R_f \text{ and } \Delta M_B(t) \text{ decays slowly with a time constant } t \\ T_{1,B} &= (R_s + R_{sd})^{-1}. \quad \text{it} \\ T_{1,B} &= (R_s + R_{sd})^{-1}. \end{aligned}$$

Figure 5.1 shows simulations of the inversion-recovery experiment used to model what would happen if a compound consisting of two dynamically and crystallographically different  $^2\text{H}$  environments, a rigid site ( $R_s = 1 \text{ s}^{-1}$ ) and a non-rigid one ( $R_f = 10 \text{ s}^{-1}$ ), was used to study the effect on  $T_1$  when spin diffusion is altered. Four graphs of the intensity ( $\Delta M_i$ ) against time ( $t$ ) were plotted each having a different spin diffusion rate constant ( $R_{sd}$ ) as explained in the caption of Fig. 5.2. Figure 5.2a shows the case when very little or no spin diffusion ( $R_{sd} = 0 \text{ s}^{-1}$ ) is present between the two  $^2\text{H}$  sites A (red line) and B (blue line). In this case, as expected, the immobile site (B) experiences a considerably longer  $T_1$  time than the non-rigid site. Similarly, Fig. 5.2b and c show the effect on the

spin-lattice relaxation time constant of sites A and B as the rate of spin diffusion ( $R_{sd}$ ) increases, in this case to 1 and 5  $s^{-1}$ . When spin diffusion is at its strongest ( $2R_{sd} \gg R_f - R_s$ ), then the sum and difference magnetizations relax separately:

$$\begin{aligned} \Delta M_A(t) + \Delta M_B(t) &= [\Delta M_A(0) + \Delta M_B(0)] \exp\left\{-\frac{1}{2}(R_f + R_s)t\right\}, \\ \Delta M_A(t) - \Delta M_B(t) &= [\Delta M_A(0) - \Delta M_B(0)] \exp\{-2R_{sd}t\}. \end{aligned} \quad (5.6)$$

Thus, as seen from Fig. 5.2d, any difference between the two magnetizations will decay very rapidly indeed with a rate constant  $2R_{sd}$ , while the sum magnetization will decay more slowly but still rapidly overall with a time constant  $T_{1,A+B} = 2/(R_f + R_s) \approx 2/R_f$ . For example, if, in the absence of spin diffusion ( $R_{sd} = 0$ ),  $T_{1,A} = 1/R_f = 0.5$  s and  $T_{1,B} = 1/R_s = 100$  s (Fig. 5.2a), then, in the course of a non-selective inversion- or saturation-recovery experiment where there is strong spin diffusion (as induced by MAS),  $\Delta M_A(t)$  and  $\Delta M_B(t)$  would both be observed decaying with a common spin-lattice relaxation time constant  $T_{1,A+B} = 1$  s  $\approx 2T_{1,A}$ , e.g.  $R_{sd} = 10$   $s^{-1}$  (Fig. 5.2d). The most noticeable effect under MAS would be the shortening of the  $T_1$  of site B by two orders of magnitude (100 s to 1 s) while the lengthening of the  $T_1$  of site A (from 0.5 s to 1 s) would be less obvious, it should also be observable.

## 5.3 Review of Previously Documented $^2\text{H}$ MAS NMR Spin-Lattice Relaxation Studies

### 5.3.1 *Alla, Eckman and Pines discussion*

In 1980, Alla *et al.* [5.2] observed that when the  $^2\text{H}$   $T_1$  of a powdered deuterated material was measured while the sample was spinning slowly, a much shorter value than they had expected was obtained. Alla *et al.* proposed a model in which this effect only occurs in solids where there are rapidly reorienting deuterons, such as those in  $-\text{CD}_3$  or  $-\text{ND}_3^+$  groups, which relax very efficiently owing to modulation of the  $^2\text{H}$  quadrupolar interaction on the timescale of the inverse of the Larmor frequency. Consequently, the faster  $T_1$  times observed in the more rigid sites of the materials is a result of spin diffusion between the two types of deuteron (rigid and rapidly reorienting).

This explanation, i.e., the observation of a greatly increased dipolar spin diffusion rate under spinning conditions, might not appear to make sense as MAS is expected to suppress the effects of the  $^2\text{H}$  dipole-dipole interaction. However, the experiments conducted by Alla *et al.* used very slow spinning rates ( $\sim 1$  kHz), and hence dipolar interactions are still present. They explained that, in a static solid, the energy levels of the immobile and rapidly reorienting deuterons are, in general, non-degenerate owing to the difference in the quadrupolar interaction of the crystallographically inequivalent deuterons and, hence, spin diffusion is

suppressed. Consequently, spinning produces a harmonic modulation of the quadrupolar interaction and, even though the deuterons would have different orientations with respect to the axis of rotation, energy-level crossings are induced during which energy-conserving spin diffusion can occur.

In this model, spin diffusion between sites A and B only occurs during the fraction  $x \ll 1$  of the rotor period when energy-level crossings occur. If one assumes that spin diffusion is negligible when the energy levels of the immobile and rapidly reorienting deuterons are non-degenerate but that it is strong (with rate constant  $R_{sd}$ ) during the crossing periods, with  $2xR_{sd} \ll R_f - R_s$  (because  $x \approx 10^{-3}$ ), then:

$$\begin{aligned}\Delta M_A(t) &= \Delta M_A(0) \exp\{-(R_f + xR_{sd})t\}, \\ \Delta M_B(t) &= \Delta M_B(0) \exp\{-(R_s + xR_{sd})t\}.\end{aligned}\tag{5.7}$$

Alla *et al.* further assumed that  $R_s \ll xR_{sd}$  and so  $\Delta M_B(t)$  decays with a time constant  $T_{1,B} \approx (xR_{sd})^{-1}$ . In this model, the shortening of the  $T_1$  of the immobile deuterons is independent of the spinning rate, as Eckman has demonstrated using a spinning rate of just 12 Hz [5.13]. However, the dipolar coupling constant of two deuterons separated by  $r = 0.15$  nm is only  $\mu_0 h \gamma_D^2 / (16\pi^3 r^3) = 0.84$  kHz and, hence, one generally predicts complete suppression of the  $^2\text{H}$  dipole-dipole interaction, including the flip-flop terms responsible for spin diffusion, at typical MAS rates of

~ 10 kHz. Therefore, this model applies only to the case of slow MAS rates, such as the 1 kHz spinning used in the original work.

### 5.3.2 *Gan and Robyr discussion*

In a more recent work conducted by Gan and Robyr [5.3],  $^2\text{H}$  NMR was investigated under faster MAS rates (~10 kHz). They explained the increased spin diffusion rate as being a result of a rotational resonance effect.

For  $^2\text{H}$  MAS NMR,  $n = 0$  is the relevant rotational resonance case at currently available magnetic field strengths. Larger integer conditions are rarely observed because of the small range of  $^2\text{H}$  chemical shifts. In this case, although not referring directly to its effects upon spin-lattice relaxation, Gan and Robyr have discussed  $^2\text{H}$  spin diffusion under typical MAS conditions in terms of a rotational resonance effect. Rather than following the instantaneous positions of the energy levels, the rotational resonance model concentrates on their time-averaged energies under MAS and indicates that strong spin diffusion will only occur when there are degeneracies between these levels. These degeneracies will arise when the centreband frequencies of the two  $^2\text{H}$  sites overlap ( $n = 0$ ). The spin diffusion rate will depend on the degree of overlap of the two MAS NMR resonances with the strongest spin diffusion being experienced in the case of complete overlap.

## 5.4 Experimental Procedures and Results

### 5.4.1 Experimental details

As in the previous chapter,  $^2\text{H}$  MAS NMR spectra were obtained at a Larmor frequency of 61.4 MHz on a Bruker Avance 400 spectrometer, equipped with a widebore 9.4 T magnet. Powdered deuterated samples were packed into 4-mm diameter  $\text{ZrO}_2$  rotors. All materials used were deuterated to enhance the  $^2\text{H}$  abundance from its natural level of 0.015% to  $\sim 100\%$ . Spin-lattice relaxation ( $T_1$ ) times were measured using either the inversion-recovery (for MAS spectra) or saturation-recovery experiments (for static spectra). Static  $^2\text{H}$  lineshapes were recorded using the Exorcypled quadrupolar-echo pulse sequence [5.14] and this was also appended to the saturation-recovery technique for static samples. The radiofrequency field strength ( $\nu_1 = \gamma B_1 / 2\pi$ ) used was approximately 100 kHz, corresponding to a  $90^\circ$  pulse length of 2.5  $\mu\text{s}$ . The spinning angle was adjusted to be as close as possible to the magic angle by minimizing the linewidth of the carboxyl  $^2\text{H}$  resonance in oxalic acid dihydrate- $d_6$ .  $^2\text{H}$  spectra were recorded at room temperature unless otherwise stated.

### 5.4.2 *L*-alanyl-glycine (*ala-gly-d*<sub>4</sub>)

Selectively deuterated *L*-alanyl-glycine (*ala-gly-d*<sub>4</sub>)  $^+\text{ND}_3\text{.CH}(\text{CH}_3)\text{.CO.ND.CH}_2\text{.CO}_2^-$  (Fig. 5.3a), was prepared by dissolving 0.5 g of non-deuterated *L*-alanyl-glycine (SIGMA) in excess  $\text{D}_2\text{O}$  (99.9

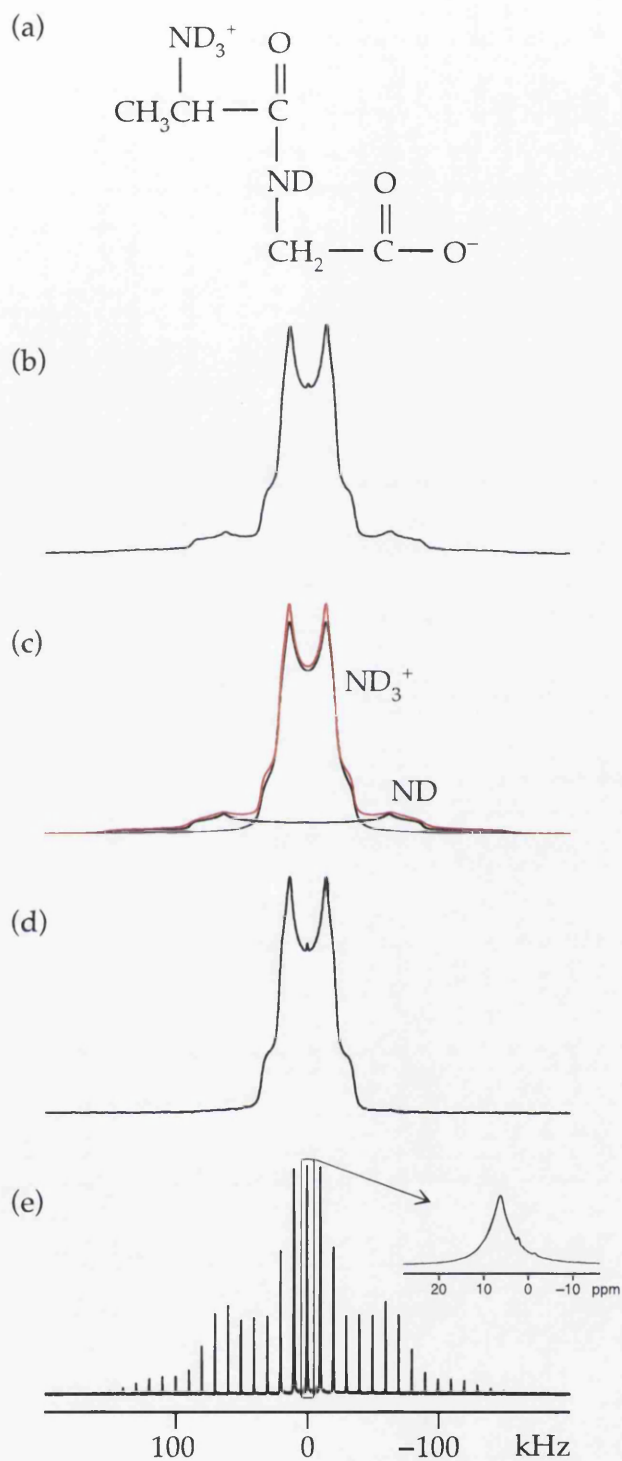


Figure 5.3: (a) Chemical structure of ala-gly- $d_4$ .  $^2\text{H}$  static and MAS NMR spectra of ala-gly- $d_4$ . (b) Static spectrum recorded with a relaxation interval of 900 s. (c) Fitting of spectrum in (b) showing broad (ND) and narrow ( $\text{ND}_3^+$ ) powder patterns making up the total lineshape. (d) Static spectrum recorded with a relaxation interval of 1 s. (e) MAS (10 kHz) spectrum recorded with a relaxation interval of 1 s. The inset shows the centreband.

at.%  $^2\text{H}$ , Aldrich) and allowing the solution to stand overnight before gently evaporating the solvent.

Figures 5.3b–d show  $^2\text{H}$  static and MAS NMR spectra of ala-gly- $d_4$ . The static spectrum recorded with a 900 s relaxation interval (Fig. 5.3b) consists of two overlapping spin  $I = 1$  Pake powder patterns, as confirmed by lineshape fitting (Fig. 5.3c). The broader powder pattern is assigned to the immobile ND deuterons, while the motionally averaged pattern is assigned to the rapidly reorienting  $\text{ND}_3^+$  deuterons. In contrast, the static spectrum recorded with a 1 s relaxation interval (Fig. 5.3d) consists of only the narrower of the two Pake patterns. The reason for this is that, while the  $\text{ND}_3^+$  deuterons relax efficiently owing to the rapid modulation of the  $^2\text{H}$  quadrupolar interaction, the immobile ND deuterons have a very long spin-lattice relaxation time. In the MAS spectrum recorded with a 1 s relaxation interval (Fig. 5.3e), however, both the broad and narrow Pake patterns are clearly present within the spinning sideband manifold, indicating the presence of two  $^2\text{H}$  sites

Table 5.1: Spin-lattice relaxation time constants ( $T_1$ ) in ala-gly- $d_4$  measured at  $B_0 = 9.4$  T.

MAS rate / kHz	Bearing gas temperature / K	$\text{ND}_3^+$	ND
		$T_1 / \text{s}$	$T_1 / \text{s}$
0 (Static)	290	$0.8 \pm 0.1$	$150 \pm 20$
3	290	$1.2 \pm 0.1$	$1.2 \pm 0.1$
5	290	$0.40 \pm 0.04$	$0.38 \pm 0.04$
10	290	$0.19 \pm 0.03$	$0.16 \pm 0.03$
14	290	$0.13 \pm 0.03$	$0.14 \pm 0.03$
3	330	$0.13 \pm 0.04$	$0.11 \pm 0.04$

where both must be possessing a  $T_1$  shorter than the 1 s allowed relaxation interval.

Table 5.1 gives the  $^2\text{H}$  spin-lattice relaxation times of the  $\text{ND}_3^+$  and ND deuterons in ala-gly- $d_4$  measured under static and MAS conditions. The short (0.8 s) and very long (150 s)  $T_1$  time constants of the  $\text{ND}_3^+$  and ND deuterons, respectively, are confirmed in the static solid.

In the centreband of the  $^2\text{H}$  MAS spectrum, the  $\text{ND}_3^+$  and ND resonances are fully degenerate (see inset in Fig. 5.3d) but the individual spin-lattice relaxation times can be determined from a spinning sideband at the edge of the powder pattern (ND) and from one near the centre of the powder pattern under the envelope of the narrower Pake doublet ( $\text{ND}_3^+$ ). Table 5.1 shows that the  $T_1$  time constants of the  $\text{ND}_3^+$  and ND deuterons are short and identical under MAS conditions, indicating the presence of very strong MAS-induced spin diffusion. However, this common  $T_1$  appears to depend on the MAS rate, being 1.2 s at a spinning rate of 3 kHz but only  $\sim 0.1$  s at 14 kHz. We believe that this apparent dependence on the MAS rate is largely due to frictional heating of the rotor to temperatures above that of the bearing gas as the MAS rate increases [5.15]. Variable-temperature spin-lattice relaxation time measurements at a MAS rate of 3 kHz support this proposal, with the  $T_1$  of  $\text{ND}_3^+$  and ND falling from 1.2 s at 290 K to  $\sim 0.1$  s at 330 K. It can be noted that at a MAS rate of 3 kHz, where there is negligible frictional heating, the common  $T_1$  of 1.2 s is intermediate between the short (0.8 s)

and long (150 s)  $T_1$  values in the static solid in accordance with the model of strong spin diffusion presented in Section 5.2.4.

To further investigate the effect of spin diffusion on spinning samples, a further two samples, 50% and 20% deuterated L-alanyl-glycine, were prepared. Both materials yielded very similar  $^2\text{H}$  MAS NMR spectra to that shown in Fig. 5.3e. This implies that both  $\text{ND}_3^+$  and ND peaks are still fully overlapped and hence still experiencing  $n=0$  rotational resonance. Table 5.2 shows the  $^2\text{H}$  spin-lattice relaxation times of the  $\text{ND}_3^+$  and ND deuterons in 50% and 20% deuterated ala-gly- $d_4$ . The  $T_1$  times of both sites get longer as the amount of deuterium in the material decreases. However, the rigid ND site is still relaxing at an extremely fast rate compared to when it is under static conditions. In addition, the common  $T_1$  observed when the material was 100% deuterated is no longer observed, as the  $T_1$  of the ND site is very slightly longer than that of the  $\text{ND}_3^+$  site.

In these cases, in spite of the fact that rotational resonance is still acting as a source of spin diffusion, the amount of deuterium in the material is smaller and hence the deuterated sites are further away within

Table 5.2: Spin-lattice relaxation ( $T_1$ ) time constants in 50% and 20% deuterated ala-gly- $d_4$  measured at room temperature using a MAS rate of 10 kHz.

	$\text{ND}_3^+$	ND
% deuteration	$T_1 / \text{s}$	$T_1 / \text{s}$
50	$0.3 \pm 0.1$	$0.4 \pm 0.1$
20	$1.6 \pm 0.1$	$1.9 \pm 0.1$

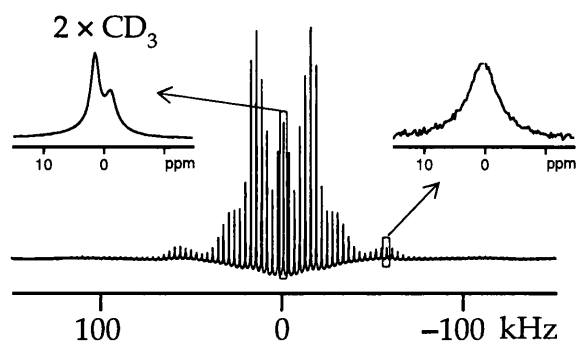


Figure 5.4:  $^2\text{H}$  MAS NMR spectrum of PMMA recorded using a spinning rate of 3 kHz. The inserts show the centreband and a sideband as labelled.

the structure, making it difficult for MAS-induced spin diffusion to act as efficiently as before. This is again in accordance with the model of intermediate spin diffusion presented in Section 5.2.4, which shows that when spin diffusion is not at its maximum, a common  $T_1$  between the sites is not observed (Fig. 5.3b and Fig. 5.3c). The reason why the  $T_1$  of the  $\text{ND}_3^+$  in the 20% deuterated material (1.6 s) site is also longer than its counterpart in the fully deuterated static solid (0.8 s), is still not clear.

#### 5.4.3 Poly(methyl methacrylate- $d_8$ ) – PMMA

The sample, used in Section 4.6.5, is used here to investigate the spin-lattice relaxation time  $T_1$  of this polymer. As already explained by Fig. 4.11, the  $^2\text{H}$  MAS NMR spectrum of this material consists of two visible peaks slightly overlapping, one originating from the methyl ( $\text{CD}_3$ ) group and the other from methoxy ( $\text{OCD}_3$ ) group. The  $\text{CD}_2$  group is not visible in the centreband of the MAS pattern but as already explained for the case of the two  $^2\text{H}$  sites in ala-gly- $d_4$ , because of its larger quadrupolar

Table 5.3: Spin-lattice relaxation ( $T_1$ ) time constants in poly(methyl methacrylate- $d_8$ ) measured at  $B_0 = 9.4$  T.

MAS rate / kHz	Bearing gas temperature / K	$2 \times \text{CD}_3$	$\text{CD}_2$
		$T_1 / \text{s}$	$T_1 / \text{s}$
Static (0)	290	$0.4 \pm 0.1$	$4.2 \pm 0.2$
3	290	$0.22 \pm 0.1$	$0.23 \pm 0.1$
5	290	$0.14 \pm 0.04$	$0.12 \pm 0.04$
10	290	$0.09 \pm 0.03$	$0.08 \pm 0.03$

coupling constant, the  $T_1$  relaxation time can be very accurately measured by using the outer sidebands (as shown in the insert of Fig. 5.4). The static quadrupolar-echo spectrum is also shown in Fig. 4.13 and is clearly made up of two overlapping Pake doublets, one more motionally-averaged than the other.

Table 5.3 gives the  $T_1$  times of the three crystallographically distinct sites measured under various MAS rates as well as under static conditions. As expected, when static, the  $\text{CD}_2$  site experiences the longest relaxation time as it is the most rigid site in the material. Both  $\text{CD}_3$  sites relax very quickly and have the same  $T_1$  relaxation time both when static and spinning. As discussed for the case of ala-gly- $d_4$ , a common  $T_1$  relaxation time is measured for all three sites when recorded under MAS conditions.

#### 5.4.4 Dimethyl terephthalate- $d_{10}$

Dimethyl terephthalate,  $\text{CH}_3\text{CO}_2\text{C}_6\text{H}_4\text{CO}_2\text{CH}_3$  (Fig. 5.5a) was prepared by reacting 0.5 g of terephthalic acid with 5  $\text{cm}^3$  of methanol in

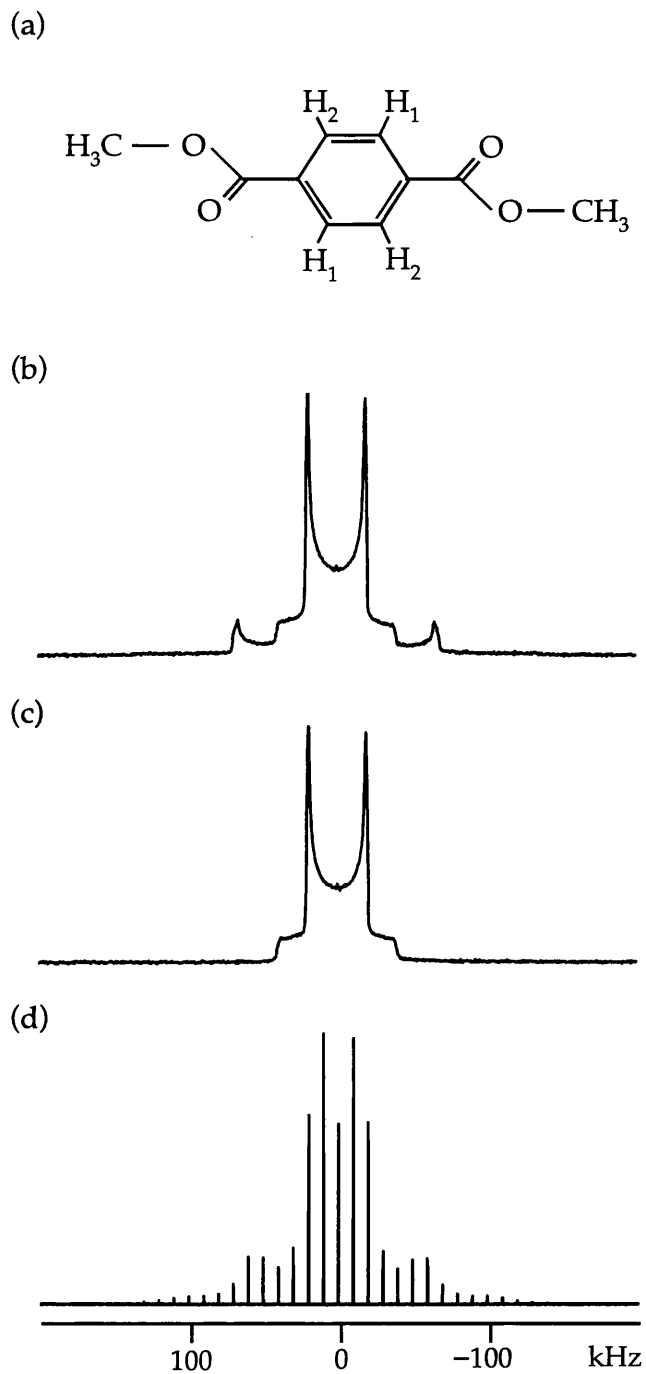


Figure 5.5: (a) Crystal structure of dimethyl terephthalate.  $^2\text{H}$  static and MAS NMR spectra of dimethyl terephthalate- $d_{10}$  (DMT- $d_{10}$ ). (b) Static spectrum recorded with a relaxation interval of 500 s. (c) Static spectrum recorded with a relaxation interval of 4 s. (d) MAS (10 kHz) spectrum recorded with a relaxation interval of 120 s.

the presence of 0.9 cm<sup>3</sup> of thionyl chloride. Full details of this procedure including the necessary safety precautions can be found in Ref. [5.16]. Perdeuterated dimethyl terephthalate-*d*<sub>10</sub> (DMT-*d*<sub>10</sub>), CD<sub>3</sub>.CO<sub>2</sub>.C<sub>6</sub>D<sub>4</sub>.CO<sub>2</sub>.CD<sub>3</sub>, was prepared using terephthalic acid-*d*<sub>4</sub> (98 at.% <sup>2</sup>H, Aldrich) and methanol-*d*<sub>4</sub> (99.8 at.% <sup>2</sup>H, Aldrich), while DMT-*d*<sub>4</sub>, CH<sub>3</sub>.CO<sub>2</sub>.C<sub>6</sub>D<sub>4</sub>.CO<sub>2</sub>.CH<sub>3</sub>, and DMT-*d*<sub>6</sub>, CD<sub>3</sub>.CO<sub>2</sub>.C<sub>6</sub>H<sub>4</sub>.CO<sub>2</sub>.CD<sub>3</sub>, were prepared using the appropriate deuterated and non-deuterated starting materials.

Figures 5.5b–d show <sup>2</sup>H static and MAS NMR spectra respectively of DMT-*d*<sub>10</sub>, which was one of the materials studied originally by Alla *et al.* [5.2]. As with ala-gly-*d*<sub>4</sub>, the static spectrum recorded with a long (500 s) relaxation interval (Fig. 5.5b) consists of two overlapping spin *I* = 1 Pake patterns, with the broader pattern assigned to the immobile aromatic (ArD) deuterons and the narrower to the rapidly reorienting CD<sub>3</sub> deuterons. The static spectrum recorded with a short (4 s) relaxation interval (Fig. 5.5c) again consists of only the narrower of the two Pake patterns. In the MAS spectrum shown in Fig. 5.5d both the broad and narrow <sup>2</sup>H powder lineshapes are evident within the spinning sideband manifold; however, it should be noted that a much longer relaxation interval (120 s) has been used to achieve this result than with ala-gly-*d*<sub>4</sub>.

Figure 5.6 shows the centreband <sup>2</sup>H MAS spectra of DMT-*d*<sub>6</sub>, DMT-*d*<sub>4</sub> and DMT-*d*<sub>10</sub>. The DMT-*d*<sub>6</sub> centreband consists of a single peak (Fig. 5.6a), arising from the two equivalent CD<sub>3</sub> groups, but the DMT-*d*<sub>4</sub> centreband consists of two peaks (Fig. 5.6b), showing that there are two

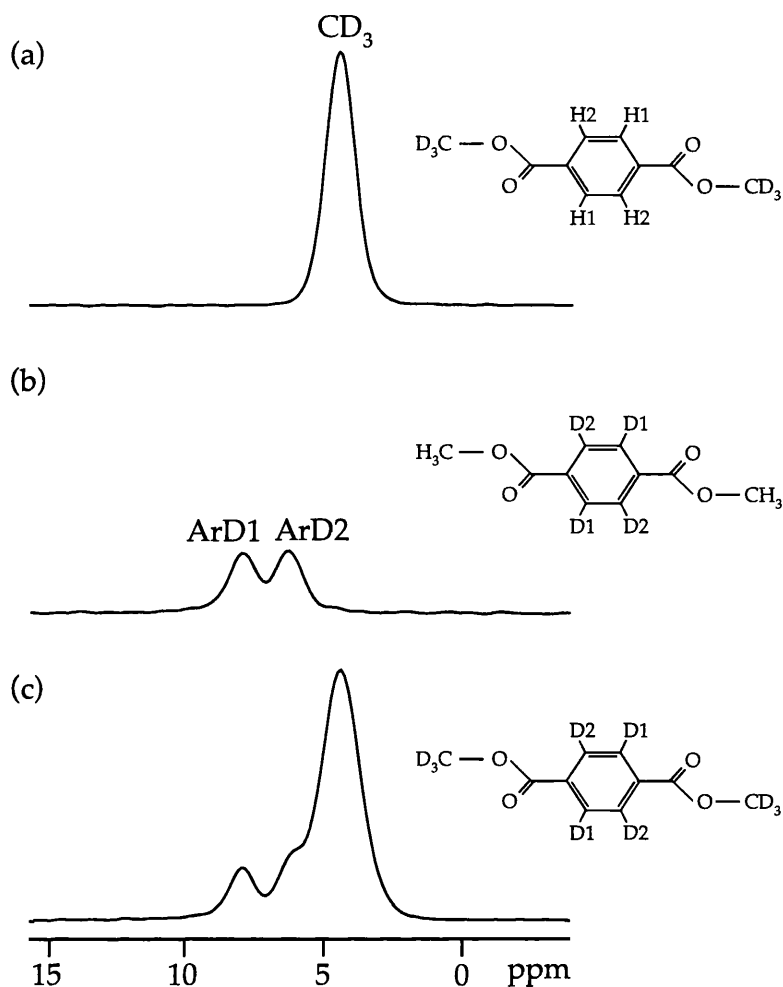


Figure 5.6:  $^2\text{H}$  MAS centreband spectra of (a) DMT- $d_6$ , (b) DMT- $d_4$  and (c) DMT- $d_{10}$ .

distinct chemical environments for the four aromatic deuterons, which can be grouped into crystallographically distinct pairs (labelled ArD1 and ArD2) as a result of the local  $C_2$  symmetry of the molecules pack. As expected, therefore, the DMT- $d_{10}$  centreband (Fig. 5.6c) consists of three peaks ( $\text{CD}_3$ , ArD1 and ArD2), with significant overlap between the  $\text{CD}_3$  and ArD2 peaks.

Table 5.4 gives the  $^2\text{H}$  spin-lattice relaxation times of the  $\text{CD}_3$  and ArD deuterons in  $\text{DMT-}d_{10}$  measured under static and MAS conditions. The short (1.3 s) and very long (230 s)  $T_1$  time constants of the rapidly reorienting  $\text{CD}_3$  and immobile ArD deuterons, respectively, are confirmed in the static solid. Under MAS, the  $T_1$  constants of the ArD deuterons are shorter than in the static solid but remain longer than that of the  $\text{CD}_3$  deuterons; there is no common  $T_1$  in this case.

It can be seen both from the examples of inversion-recovery centreband and sideband spectra in Figs. 5.7a and 5.7b and the  $T_1$  values in Table 5.4 that the ArD2 deuterons in  $\text{DMT-}d_{10}$ , whose centreband overlaps significantly with that of the  $\text{CD}_3$  deuterons, relax faster under MAS than the ArD1 deuterons. In contrast, in the inversion-recovery MAS spectra of  $\text{DMT-}d_4$  shown in Fig. 5.7c, the ArD1 and ArD2 peaks relax at a similar rate, which is much slower than that of the corresponding peaks in  $\text{DMT-}d_{10}$ . These results show that it is spin

Table 5.4: Spin-lattice relaxation time constant ( $T_1$ ) in  $\text{DMT-}d_{10}$  measured at  $B_0 = 9.4$  T.

		$\text{CD}_3$	ArD1	ArD2
MAS rate / kHz	Bearing gas temperature / K	$T_1 / \text{s}$	$T_1 / \text{s}$	$T_1 / \text{s}$
Static (0)	290	$1.3 \pm 0.2$		$230 \pm 20$
2	290	$1.3 \pm 0.1$	$150 \pm 10$	$68 \pm 5$
5	290	$1.4 \pm 0.1$	$55 \pm 5$	$27 \pm 5$
8	290	$1.5 \pm 0.1$	$36 \pm 3$	$15 \pm 4$
10	290	$1.6 \pm 0.1$	$32 \pm 3$	$7 \pm 1$
2	330	$1.8 \pm 0.2$	$52 \pm 5$	$36 \pm 5$

diffusion enhanced by  $n=0$  rotational resonance (the Gan-Roby mechanism [5.3]) that is dominating spin-lattice relaxation under typical MAS conditions: in DMT- $d_{10}$ , the ArD2 peak relaxes fairly rapidly because of its degree of centreband overlap with the  $CD_3$  peak; the ArD1 peak relaxes slower than the ArD2 peak because of its negligible centreband overlap with the  $CD_3$  peak but its relaxation is still enhanced relative to that in the static solid due to its partial overlap with the ArD2 peak.

The  $T_1$  values in Table 5.4 again depend on the MAS rate; in this case, however, the dependence does not appear to be due primarily to temperature-induced dynamical changes in the solid (the changes in  $T_1$  values from 290 to 330 at a MAS rate of 2 Hz are relatively small) but seems to be a genuine effect. Consider first the results at a 2 Hz MAS rate: the Gan-Roby mechanism appears to be already active (the  $T_1$  of ArD2 is shorter than that of ArD1) but the Alla-Eckman-Pines mechanism is possibly still important in enhancing the overall spin diffusion rate constant. As the MAS rate is increased, we would expect the latter mechanism to decline rapidly in importance, however, we observe the  $T_1$  values of the ArD1 and, in particular, ArD2 deuterons becoming progressively shorter, indicating enhanced spin diffusion through a rotational resonance effect. This observation is perhaps unexpected in view of theoretical predictions for  $n=0$  rotational resonance among spin  $I = 1/2$  nuclei [5.17] but is not inconsistent with the spin diffusion rate being very small both in the static solid and under extremely rapid MAS ( $\gg 10$  kHz).

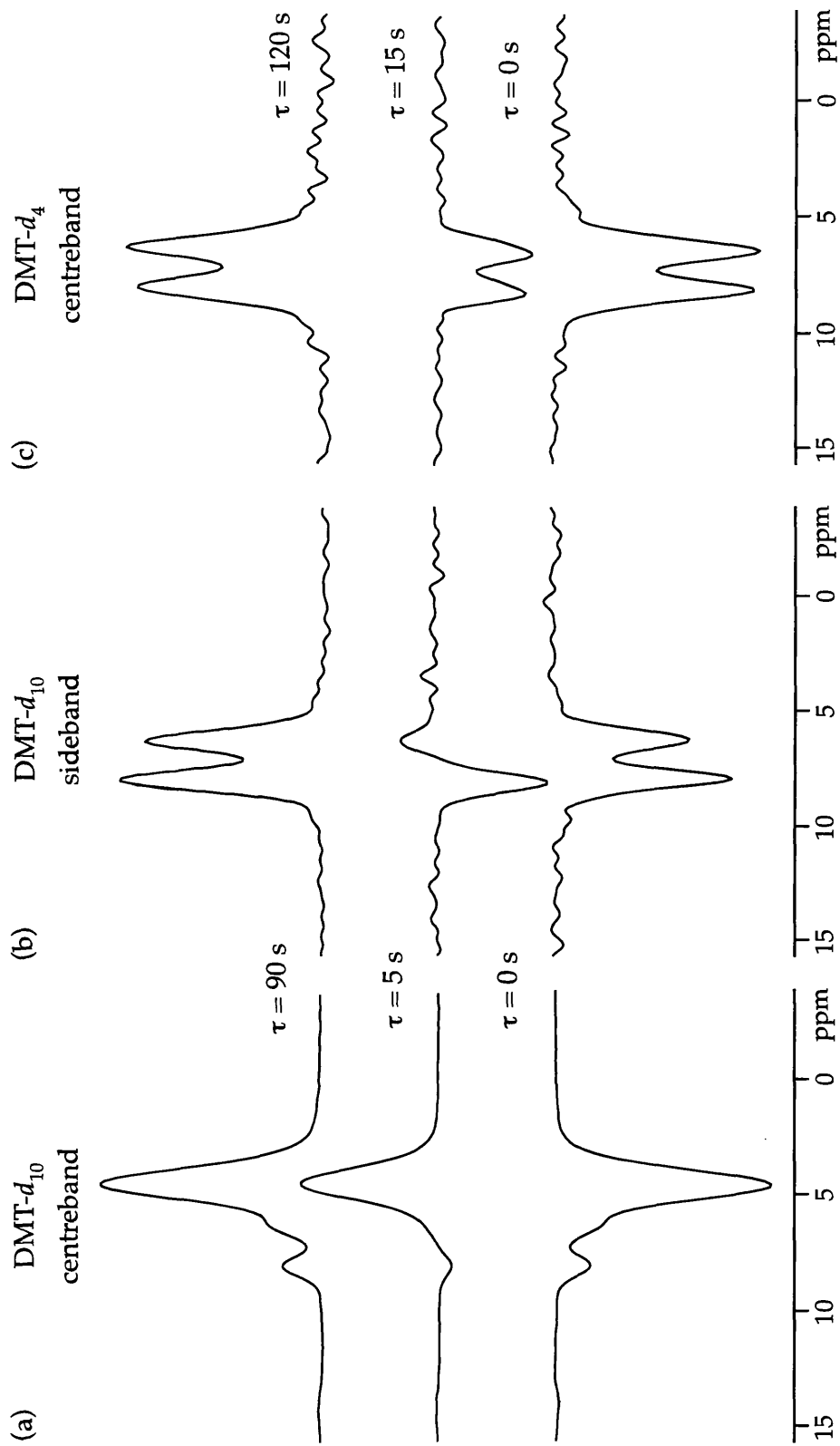


Figure 5.7: Inversion-recovery  $^2\text{H}$  MAS (10 kHz) spectra recorded using the  $\tau$  intervals (between the  $180^\circ$  and  $90^\circ$  pulses) shown. (a) DMT- $d_{10}$  centreband spectra. (b) DMT- $d_{10}$  sideband spectra (where the  $\text{CD}_3$  peak is absent). (c) DMT- $d_4$  centreband spectra.

## 5.5 Conclusions

In materials where the phenomenon occurs, the shortening of the  $^2\text{H}$   $T_1$  time constants of immobile deuterons under MAS is extraordinarily useful. For example, in ala-gly- $d_4$ , the reduction of  $T_1$  from  $\sim 150$  s in the static solid to  $\sim 1$  s under MAS represents a greater than ten-fold increase in the integrated-signal-to-noise ratio per unit experiment time. This increase is multiplicative, of course, as the sensitivity is improved because the signal amplitude is concentrated into the spinning sidebands. Moreover, this is a great advantage when measuring molecular-scale dynamics in the solid-state (recall Chapter 4). Compared with the quadrupolar-echo experiment, which is the conventional approach to measure motion in solids, apart from better sensitivity, the  $^2\text{H}$  double-quantum MAS NMR experiment is also less time consuming.

In this chapter the origin of the shorter  $T_1$  observed in spinning samples was discussed and it was shown that it occurs as a result of increased spin diffusion arising largely, as discussed by Gan and Robyr [5.3], from an  $n = 0$  rotational resonance effect. In materials such as ala-gly- $d_4$  and PMMA where there is complete spectral overlap of the  $^2\text{H}$  MAS NMR centrebands of the immobile and rapidly reorienting deuterons, spin diffusion will be very strong and a common  $T_1$  will be observed. In contrast, in materials such as DMT- $d_{10}$  where there is only incomplete overlap of the MAS centrebands, spin diffusion will still be enhanced and reduced  $T_1$  values observed for immobile deuterons but

these will remain longer than those of the rapidly reorienting deuterons. At the fast MAS rates used routinely nowadays, the mechanism for reduced  $^2\text{H}$   $T_1$  time constants proposed originally by Alla *et al.* [5.2] for the slow spinning case appears to play a much less significant role.

It seems likely that the MAS-induced effects described here for the spin  $I = 1$   $^2\text{H}$  nucleus will also be important in NMR spectroscopy of other quadrupolar nuclei, including those with half-integer spin quantum numbers ( $I = 3/2, 5/2$ , etc.), and Kwak *et al.* have recently shown some interesting results that are relevant to this area [5.18].

# Structure and NMR Assignment in Microporous Aluminophosphates (AlPOs)

---

### 6.1 Introduction

In this chapter heteronuclear correlation NMR experiments in which the  $J$  coupling is used to transfer polarization from a quadrupolar nucleus ( $^{27}\text{Al}$ ,  $I = 5/2$ ) to a spin  $I = 1/2$  nucleus ( $^{31}\text{P}$ ) are used in conjunction with 'first-principles' calculations performed by Dr Sharon E. Ashbrook at St Andrews University to investigate the framework and structure of aluminophosphates (AlPOs). The AlPOs that will be discussed here are AlPO-14 isopropylamine (*ipa*), AlPO-14 piperidine (*pip*) and calcined-dehydrated AlPO-14 [6.1–6.3], and AlPO-53 methylamine (AlPO-53(A)) and calcined-dehydrated AlPO-53 (AlPO-53(B)) [6.4].

The aim of this work is to obtain NMR parameters for each site in the material and consequently assign the NMR spectra of the aluminophosphates being studied. Assignment will give an insight into the framework topology of the material. Assignment using solely NMR

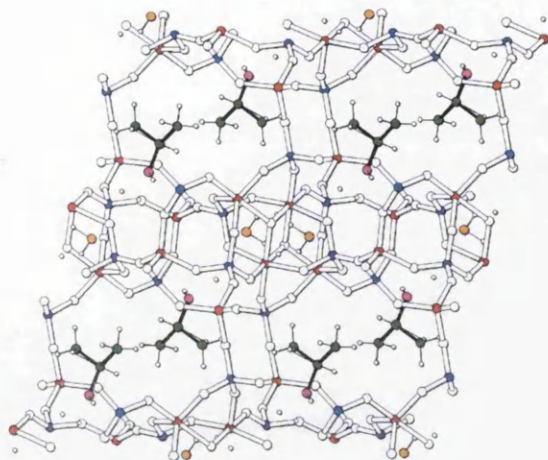
results has been applied previously to AlPO-14 *ipa* [6.5, 6.6]. This involves the use of a two-dimensional  $^{27}\text{Al}$ - $^{31}\text{P}$  heteronuclear correlation NMR experiment (MQ-*J*-HETCOR) that exploits  $^{27}\text{Al}$  multiple-quantum coherences and *J* couplings to yield a correlation spectrum showing Al-O-P connectivities. The existing NMR technique is going to be refined and applied to both calcined-dehydrated AlPO-14 and AlPO-14 *pip*. The NMR assignment of the latter is complicated by the absence of a published crystal structure but it will be shown that it is possible to make plausible progress by assuming a framework topology identical to calcined-dehydrated AlPO-14 and AlPO-14 *ipa*.

Unlike AlPO-14, the three forms of AlPO-53 indicated in Ref. 6.4 have never been investigated using NMR before. Consequently, MAS NMR experiments such as the MQMAS experiment needed to be performed with the aim of obtaining as much information as possible about the materials before the ultimate aim of assigning the NMR spectra of both  $^{27}\text{Al}$  and  $^{31}\text{P}$  nuclei could be achieved.

## 6.2 Aluminophosphates (AlPOs)

AlPOs are microporous materials that have attracted a lot of interest over the past decade because of their ability to be used as molecular sieves and catalysts. They have similar framework topologies to zeolites, but their calcined material consists entirely of  $\text{AlO}_4$  and  $\text{PO}_4$

(a)



(b)

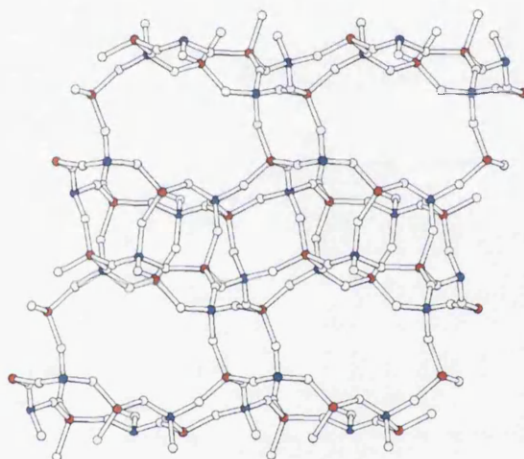


Figure 6.1: Structure of AlPO-14 (a) isopropylamine and (b) calcined-dehydrated.

tetrahedra [6.7]. AlPOs can be templated, i.e., an organic templating agent, such as isopropylamine, can be used to fill the cavity in the AlPO structure as shown in Fig. 6.1a [6.8].

Aluminophosphates are most commonly synthesized hydrothermally from an aqueous mixture of aluminium oxyhydroxide or alkoxide and phosphoric acid. The organic template is introduced by the

addition of an amine or quaternary ammonium salt to the initial reaction mixture. Calcination, i.e., the process that removes the organic template, water, and the hydroxyl group, is done by heating the as-synthesized material to temperatures of 500–600 °C. Figure 6.1b shows the structure of AlPO-14 after calcination, hence showing a template-free cavity in the AlPO structure.

All the AlPOs discussed in this chapter were synthesized for us by the Walton group at the University of Warwick.

### 6.3 Heteronuclear NMR Experiments

#### 6.3.1 *The MQ-J-INEPT experiment*

Figure 6.2 shows the pulse sequence and coherence transfer pathway used for the acquisition of the MQ-J-HETCOR experiment. This pulse sequence is made up of two parts: a MQMAS (multiple-quantum magic angle spinning) part and an INEPT (insensitive nuclei enhanced by polarization transfer) part. The MQ-J-HETCOR sequence described here is a modified version of a published pulse sequence [6.5], removing the unnecessary 90° pulse at the end of the  $t_1$  period and using a 6-step phase cycle to select both +3 and -3 coherences making the experiment amplitude modulated as shown by the coherence transfer pathway in Fig.

6.2. In addition, the States-Harberkorn-Ruben (refer to Section 3.8) method of  $\delta_1$  sign discrimination was used.

The split- $t_1$  MQMAS part of the pulse sequence (refer to Section 3.7), labelled as period A in Fig. 6.2, removes the second-order quadrupolar interaction, hence producing an isotropic spectrum of the  $I$  spin in the  $\delta_1$  dimension, which makes lines narrower and therefore better resolved. To further increase the sensitivity, a SPAM (soft-pulse-added-mixing) [6.9,6.10] composite pulse used for of the second pulse in this period. This involves the application of a low-power central-transition selective  $90^\circ$  pulse immediately after a high-power pulse, with the two having the same relative radiofrequency phase. As illustrated by the coherence transfer pathway, the first hard pulse in the sequence is used to excite triple-quantum ( $m_I = +3/2 \leftrightarrow -3/2$ ) in the  $I$  spins. Triple-quantum is then converted to single-quantum coherence using the SPAM pulse in the split- $t_1$  period. Experimental investigation showed that the addition of the SPAM pulse enhanced the signal obtained by 80%.

The rest of the sequence is essentially a refocused INEPT experiment (refer to Fig. 3.6), where a two-dimensional correlation spectrum is obtained by using the magnetization of the  $^{27}\text{Al}$  ( $I$ ) spins formed during  $t_1$ , as a source of polarization for the  $^{31}\text{P}$  ( $S$ ) spins.

Antiphase magnetization is created during period B on the  $I$  spin which is then transferred to the  $S$  spin using the two pulses in period C through the heteronuclear  $J$  coupling. During period D, the antiphase



state evolves back to in-phase  $S$ -spin magnetization. This will produce a two-dimensional correlation consisting of the spectrum for the  $S$  spin in the direct ( $\delta_2$ ) dimension and that of the  $I$  spin in the indirect dimension ( $\delta_1$ ). The maximum amount of signal is obtained from this sequence when the  $\tau$  interval values are  $1/(4J_{IS})$  and when the magnetization transfer arises from large one-bond heteronuclear couplings.

Further improvement in the resolution of this HETCOR experiment is obtained by decoupling the  $^{31}\text{P}$  spectrum in the  $t_2$  period. Delevoye *et al.* [6.11] were the first to point out that decoupling of  $^{27}\text{Al}$  and  $^1\text{H}$  is essential to resolve all four  $^{31}\text{P}$  peaks present in the templated form of AlPO-14. In addition to decoupling during acquisition,  $^1\text{H}$  decoupling was also employed during the INEPT part of the pulse sequence [6.5].

### 6.3.2 The HMQC experiment

The pulse sequence for the HMQC (heteronuclear multiple-quantum correlation) experiment is shown in Fig. 6.3. Like the MQ- $J$ -HETCOR experiment, the HMQC technique generates two-dimensional through-bond chemical shift correlations between spins  $I$  and  $S$ ; however, the  $S$  spin is detected indirectly. In period A, the  $I$  spin is excited and allowed to evolve into antiphase magnetization. In period B, the antiphase magnetization is converted into heteronuclear multiple-quantum coherence, which is allowed to evolve during the  $t_1$  period (period C). Period D converts the multiple-quantum coherence back into

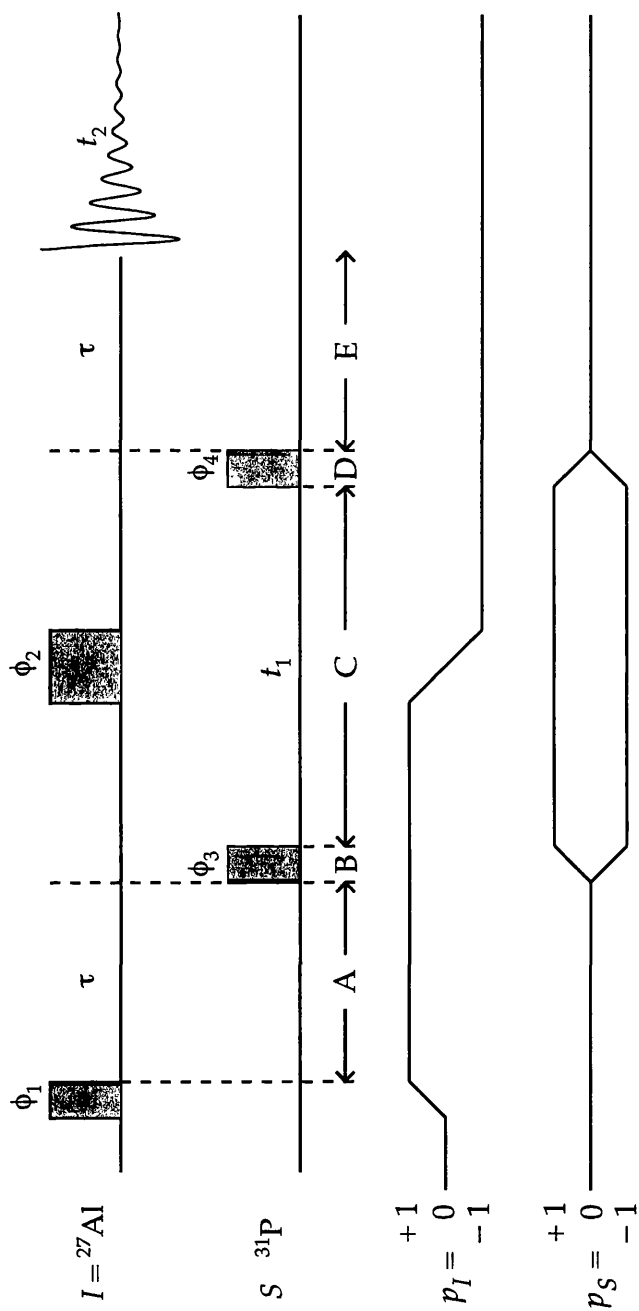


Figure 6.3: Pulse sequences and coherence transfer pathways for HMQC NMR experiments. The coherence transfer pathway was selected with an 8-step phase-cycle:  $\phi_1 = \phi_4 = 0^\circ$ ;  $\phi_2 = 0^\circ$   $90^\circ$   $180^\circ$   $180^\circ$   $0^\circ$   $180^\circ$   $0^\circ$   $180^\circ$   $0^\circ$ ; where  $\phi_R$  is the phase of the receiver.

observable magnetization on the  $I$  spin. Period E leaves enough time for the coupling to rephase, after which the signal is acquired. Furthermore, the offset of spin  $I$  is refocused by the end of the pulse sequence as the  $180^\circ$  pulse in period C creates a spin echo.

## 6.4 Experimental Details

All NMR experiments presented here were performed on a Bruker Avance 400 spectrometer, equipped with a widebore 9.4 T magnet, operating at a Larmor frequency,  $\nu_0$ , of 104.3 MHz for  $^{27}\text{Al}$  ( $I = 5/2$ ), 162.0 MHz for  $^{31}\text{P}$  ( $I = 1/2$ ), and 400.1 MHz for  $^1\text{H}$  ( $I = 1/2$ ) or on a Bruker Avance 200 spectrometer, equipped with a widebore 4.7 T magnet, operating at a Larmor frequency,  $\nu_0$ , of 52.1 MHz for  $^{27}\text{Al}$ , 81.0 MHz for  $^{31}\text{P}$ , and 200.1 MHz for  $^1\text{H}$ . Spectra were recorded at ambient temperatures using 4-mm diameter  $\text{ZrO}_2$  rotors spinning at a rate of 10 kHz. Chemical shifts are recorded in parts per million relative to 1 M  $\text{Al}(\text{NO}_3)_3$  (aq) for  $^{27}\text{Al}$ , and for  $^{31}\text{P}$ , borane triphenylphosphine was used as a secondary reference ( $^{31}\text{P}$  peak at 21 ppm) [6.12]. Where necessary, continuous-wave (CW) decoupling was employed to improve resolution, with typical radiofrequency field strengths ( $\gamma B_1/2\pi$ ) of  $\sim 10$  kHz for  $^{27}\text{Al}$  and  $\sim 80$  kHz for  $^1\text{H}$ .

First-principles calculations of NMR parameters were performed using the CASTEP [6.13, 6.14] density functional theory (DFT) code, a planewave, pseudopotential [6.15, 6.16] code that exploits the periodic

nature of crystalline solids. CASTEP employs the gauge-including projector-augmented wave (GIPAW) [6.17] algorithm, enabling the reconstruction of the all-electron wave function in the presence of a magnetic field.

Structural parameters (the unit cell and all atomic positions) were obtained from experimental diffraction studies in the literature. The crystal structure was reproduced from these parameters by the use of periodic boundary conditions. Where necessary, geometry optimization was also performed within the CASTEP program, with either just the atomic coordinates or both the lattice parameters and atomic coordinates allowed to vary. For AlPO-14 *ipa*, an initial geometry optimization involving just the H positions was performed prior to any further calculations. After full optimization, forces of less than  $\sim 100$  meV  $\text{\AA}^{-1}$  (AlPO-14 *ipa*) and  $\sim 30$  meV  $\text{\AA}^{-1}$  (AlPO-14) were observed. Of course, this method breaks down if the crystal structure is not available, or not accurate. These limitations and possible ways to overcome them will be discussed.

## 6.5 AlPO-14: Results and Discussion

### 6.5.1 AlPO-14: An overview

AlPO-14 was one of the first groups of AlPOs introduced by Wilson *et al.* [6.18] in 1982 and the most widely studied by NMR to date. The structure of AlPO-14 consists of a three-dimensional channel system formed by 8-ring pores with four ( $n = 1-4$ ) crystallographically different aluminium and phosphorus sites,  $P_n$  and  $Al_n$ . As with all other AlPOs, several organic templating agents can be used in the synthesis of AlPO-14. The most extensively studied member of the AlPO-14 family is AlPO-14 with isopropylamine (*ipa*) as the guest molecule in the cavity within the structure, referred to here as AlPO-14 *ipa* ( $Al_8P_8O_{32}(OH)_2(C_3H_7N)_2(H_2O)_2$ ). AlPO-14 *ipa* aroused a lot of interest because it consists of three different types of aluminium polyhedra within its structure: Al2 and Al3 are tetrahedral, Al1 is trigonal-bipyramidal and Al4 is octahedral. The hydroxyl groups provide the extra bond to Al1 and two additional bonds to Al4. The isopropylamine template is protonated and hence balances the negative charge of the hydroxyl group. As seen in Table 6.1, in the AlPO-14 framework [6.3, 6.19], Al1 is connected (via Al-O-P linkages) to all four P species, whereas Al2 has two such linkages to P1, one to P2, and one to P4, but is not connected to P3. Similarly, Al3 is not connected to P2, but has two Al-O-P linkages to P3 and one to each of P1 and P4. Finally, Al4 has two Al-O-P linkages to P2, one to each of P3 and P4, but is not connected to P1.

While the framework and structure of the calcined-dehydrated AlPO-14 material is also well known [6.3,6.19], information about a second as-synthesized material AlPO-14 *pip*, prepared using piperidine as the organic template molecule, is not widely available [6.2]. The unit cell of the calcined-dehydrated form is composed of  $\text{Al}_8\text{P}_8\text{O}_{32}$ , with four crystallographically unique four-coordinate P and Al sites. The powder XRD structure of AlPO-14 *pip* ( $\text{Al}_8\text{P}_8\text{O}_{32}(\text{OH})_2(\text{C}_3\text{H}_7\text{NH}_2)_2(\text{H}_2\text{O})_2$ ) has never been published and therefore the framework and structure are still unknown. What is known however is that when AlPO-14 *pip* is calcined, calcined-dehydrated AlPO-14 is the material produced, implying that its framework topology ought to be the same as that of any other AlPO-14. Evidence of this is found in the high-resolution solid-state NMR experiments published recently [6.20]. Antonijevic *et al.* [6.20] discuss dynamics on the microsecond timescale using multiple-quantum and satellite-transition magic angle spinning techniques on AlPO-14. They show that motion on this timescale is not present in calcined-dehydrated AlPO-14 but both templated materials are dynamic systems. However, the extent of their dynamics is different, implying possibly a slight difference in their framework.

Table 6.1: Identity and number of expected Al-O-P connectivities in the framework of AlPO-14 predicted by XRD data.

	P1	P2	P3	P4
Al1	1	1	1	1
Al2	2	1	-	1
Al3	1	-	2	1
Al4	-	2	1	1

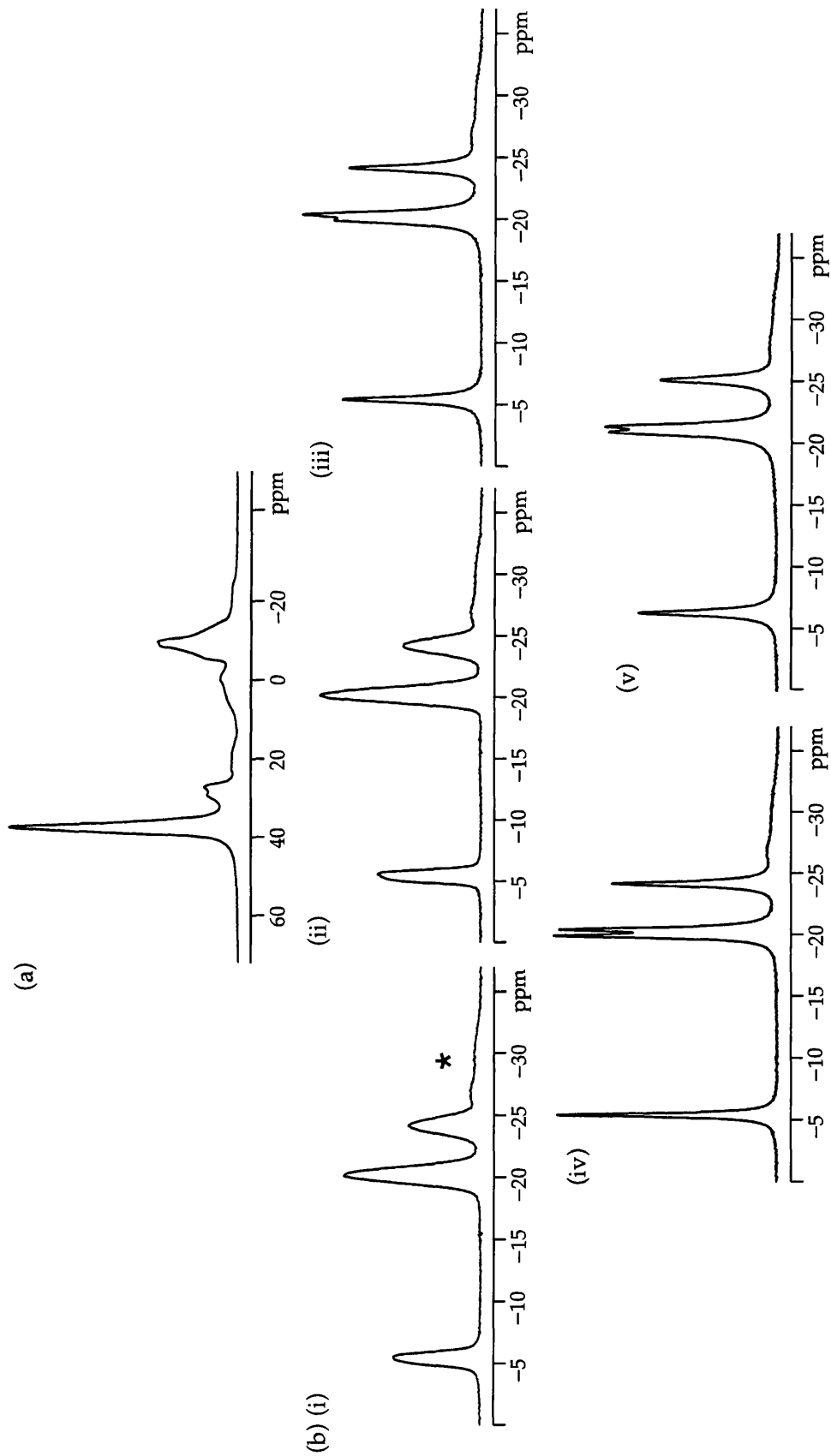


Figure 6.4: AlPO-14 ipa MAS NMR spectra. (a)  $^{27}\text{Al}$ , (b)  $^{31}\text{P}$  MAS NMR (i) not decoupled, (ii)  $^1\text{H}$  decoupled, (iii)  $^{27}\text{Al}$  decoupled, (iv) 70 kHz  $^1\text{H}$  and 6.5 kHz  $^{27}\text{Al}$  decoupled and (v) 70 kHz  $^1\text{H}$  and 8.5 kHz  $^{27}\text{Al}$  decoupled spectrum. Spectra were recorded using (a) 64 transients and 5 s relaxation interval and (b) 4 transients and 180 s relaxation interval. \* marks an  $^{31}\text{P}$  impurity.

AlPO-14 *ipa* is a very well known and extensively studied material and hence we use it here to demonstrate how the  $^{27}\text{Al}$ - $^{31}\text{P}$  MQ-J-HETCOR NMR experiment can be used to obtain structural and framework information for the material under investigation. Also in this section, the calcined-dehydrated AlPO-14 and AlPO-14 *ipa*  $^{27}\text{Al}$ - $^{31}\text{P}$  MQ-J-HETCOR NMR spectrum will be assigned for the first time.

### 6.5.2 AlPO-14 *ipa*

As discussed earlier, structure, framework and connectivities of AlPO<sub>4</sub>-14 *ipa* are well known and it features in several NMR and crystallographic publications. Figure 6.4 shows the  $^{27}\text{Al}$  MAS NMR (Fig. 6.4a) spectrum and the  $^{31}\text{P}$  MAS NMR (Fig. 6.4b) spectrum of AlPO-14 *ipa*. It is rather difficult from these two spectra to make out the four distinct aluminium and phosphorus sites present in this material. An increase in resolution is essential to eventually achieve a clear heteronuclear correlation spectrum. There are various ways possible to increase resolution in MAS NMR experiments, some of which were already discussed in Chapter 3. For the  $^{27}\text{Al}$  NMR spectrum, increased resolution is going to be achieved by performing a MQMAS experiment, which gives an  $^{27}\text{Al}$  spectrum free of second order quadrupolar broadening; in other words, the isotropic spectrum obtained in the  $\delta_1$  dimension will contain much narrower (and hence resolved peaks) making it possible to observe all four expected distinct aluminium sites predicted by XRD data.

Increased resolution in the  $^{31}\text{P}$  NMR spectrum is obtained by applying heteronuclear broadband decoupling to the MAS NMR spectrum. Figure 6.4b illustrates the effect of (i) not decoupled, (ii)  $^1\text{H}$  decoupled, (iii)  $^{27}\text{Al}$  decoupled and (iv) both  $^1\text{H}$  and  $^{27}\text{Al}$  decoupled spectrum. Sharper lines are clearly observed when both  $^1\text{H}$  and  $^{27}\text{Al}$  are decoupled from the  $^{31}\text{P}$  spectrum. Consequently, four peaks corresponding to the four distinct  $^{31}\text{P}$  sites present in AlPO-14 *ipa* are resolved and listed in Table 6.1. The optimum combination of  $^1\text{H}$  and  $^{27}\text{Al}$  decoupling, i.e., the amount of decoupling power that produced the narrowest peaks, was found to be ~80 kHz of  $^1\text{H}$  decoupling power and ~6.5 kHz for  $^{27}\text{Al}$ . It was interesting to observe that as 6.5 kHz  $^{27}\text{Al}$  decoupling power was exceeded the  $^{31}\text{P}$  MAS NMR spectrum started to broaden once again as shown by Fig. 6.4b (v) where ~8.5 kHz of  $^{27}\text{Al}$  decoupling was applied together with the same 80 kHz of  $^1\text{H}$  decoupling power.

Incorporating these resolution-enhancing methods into a heteronuclear correlation experiment pulse sequence produces the MQ-*J*-HETCOR experiment discussed earlier and shown in Fig. 6.2. This experiment gives a two-dimensional spectrum that correlates the  $^{27}\text{Al}$  ( $\delta_1$  dimension) and  $^{31}\text{P}$  ( $\delta_2$  dimension) sites in AlPO-14 *ipa* connected through an Al-O-P bond. Fig. 6.5 shows the MQ-*J*-HETCOR spectrum of AlPO-14 *ipa*. The optimum  $\tau$  interval value for this material was found to be 3.5 ms. As explained earlier, the Al-O-P connectivity was probed via the two-bond *J* couplings, hence every correlation peak in the spectrum corresponds to an Al-O-P connectivity. The high resolution obtained in  $\delta_1$

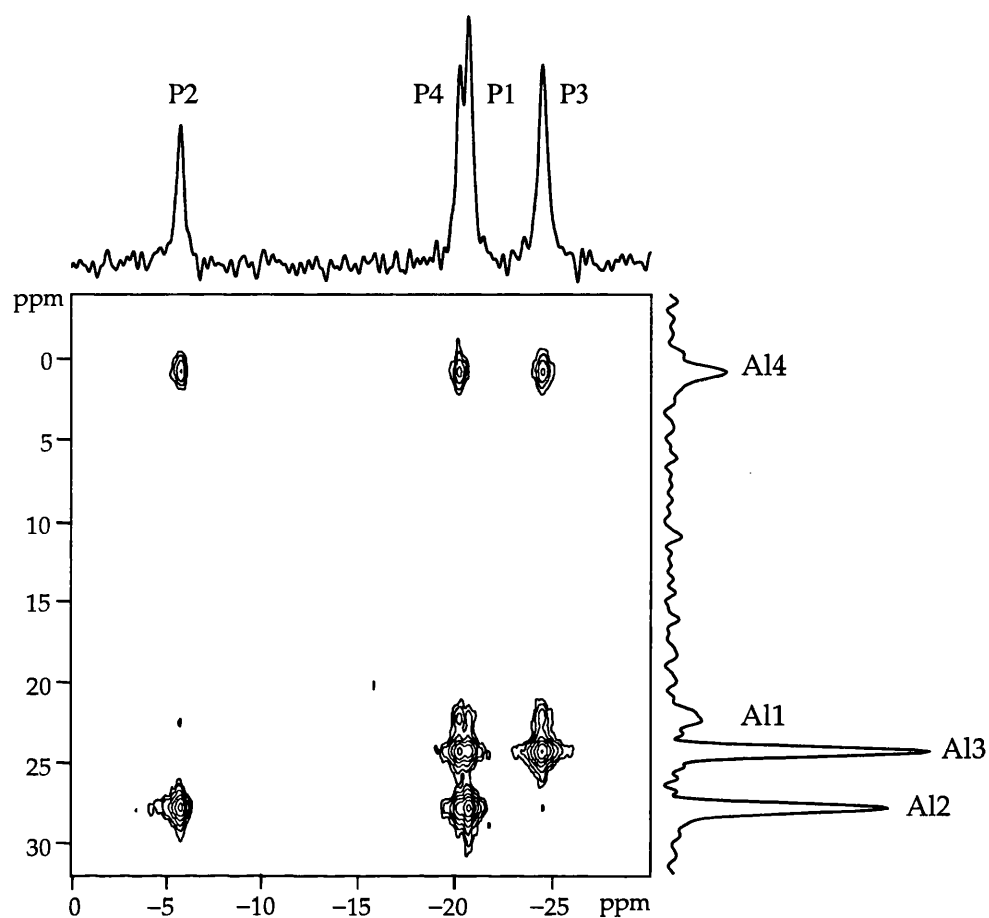


Figure 6.5: MQ-J-HETCOR two-dimensional spectrum recorded with 288 transients acquired for each of 256  $t_1$  increments and relaxation interval of 3 s (and  $\delta_1$  and  $\delta_2$  projections).

enables all eight expected cross peaks to be fully resolved and hence the  $^{27}\text{Al}$  and  $^{31}\text{P}$  spectra of AlPO-14 *ipa* could be assigned. These can be compared with the assignments first proposed by Fyfe *et al.* [6.8] mentioned in Section 6.5.1 and summarized in Table 6.1. The A12/P3, A13/P2 and A14/P1 cross peaks are, as expected, missing. The resulting peak assignments are shown in Fig. 6.5.

The diffraction data in Ref. [6.3] was used to perform first-principles calculations using the NMR CASTEP code [6.17]. The resulting calculated parameters were expected to agree with the  $^{27}\text{Al}$  NMR parameters extracted from the MQMAS experiment [6.20]. However, this was not the case. A satisfactory agreement with the experimental values was only achieved after the structure geometry was first optimized using the energy-minimization capability of the main CASTEP code. First, only the H positions were relaxed, however, the best agreement with NMR experimental parameters was only obtained after all atomic coordinates and the unit cell parameters were optimized as shown in Table 6.2. Only small changes in the atomic positions were observed when the unit cell dimensions were allowed to vary. Expansions between 0.03 and 0.1 Å were seen. This unexpected observation suggests that NMR is extremely sensitive to very slight changes in the geometry of the crystal structure. The assignments obtained from the NMR CASTEP calculations are in full agreement with the assignments labelled on the two-dimensional correlation spectrum in Fig. 6.5 and consequently with the assignments already available in the literature. A reasonable agreement was also obtained for the  $^{31}\text{P}$  chemical shifts obtained from the first-principles calculation and these values are also shown in Table 6.2.

As stated earlier, the knowledge and understanding acquired in using a combination of NMR spectroscopy and first-principles calculations to yield accurate information about the framework topology of AlPO-14 *ipa* is going to be used to investigate other, less well known AlPOs whose NMR spectra are still unassigned.

Table 6.2: Experimental and calculated  $^{27}\text{Al}$  isotropic chemical shifts ( $\delta_{\text{iso}}$ ) and quadrupolar parameters (coupling constant  $C_Q$  and asymmetry  $\eta$ ) for  $\text{AlPO-14 ipa}$ .

Site	$\delta_{\text{iso}}$ (ppm)	$C_Q$ / MHz	$\eta_Q$
Experimental (Ref. 6.20 and this work)			
Al1	27	5.6	1.0
Al2	44	4.1	0.8
Al3	43	1.7	0.6
Al4	-1	2.6	0.7
P1	-20.6		
P2	-5.8		
P3	-24.3		
P4	-20.1		
Calculated (optimization of H positions only)			
Al1	35.9	10.5	0.73
Al2	41.5	-6.5	0.74
Al3	41.6	-3.78	0.59
Al4	6.3	-1.98	0.85
P1	-17.5		
P2	3.2		
P3	-19.5		
P4	-16.0		
Calculated (optimization of all atomic coordinates only)			
Al1	32.5	7.45	0.74
Al2	45.3	4.63	0.88
Al3	41.9	4.57	0.73
Al4	1.3	2.32	0.27
P1	-19.8		
P2	-1.8		
P3	-21.9		
P4	-16.9		
Calculated (optimization of all atomic coordinates and unit cell parameters)			
Al1	29.5	6.01	0.92
Al2	44.8	-3.98	0.94
Al3	42.6	-2.27	0.98
Al4	1.4	2.42	0.56
P1	-19.9		
P2	-1.1		
P3	-22.3		
P4	-17.0		

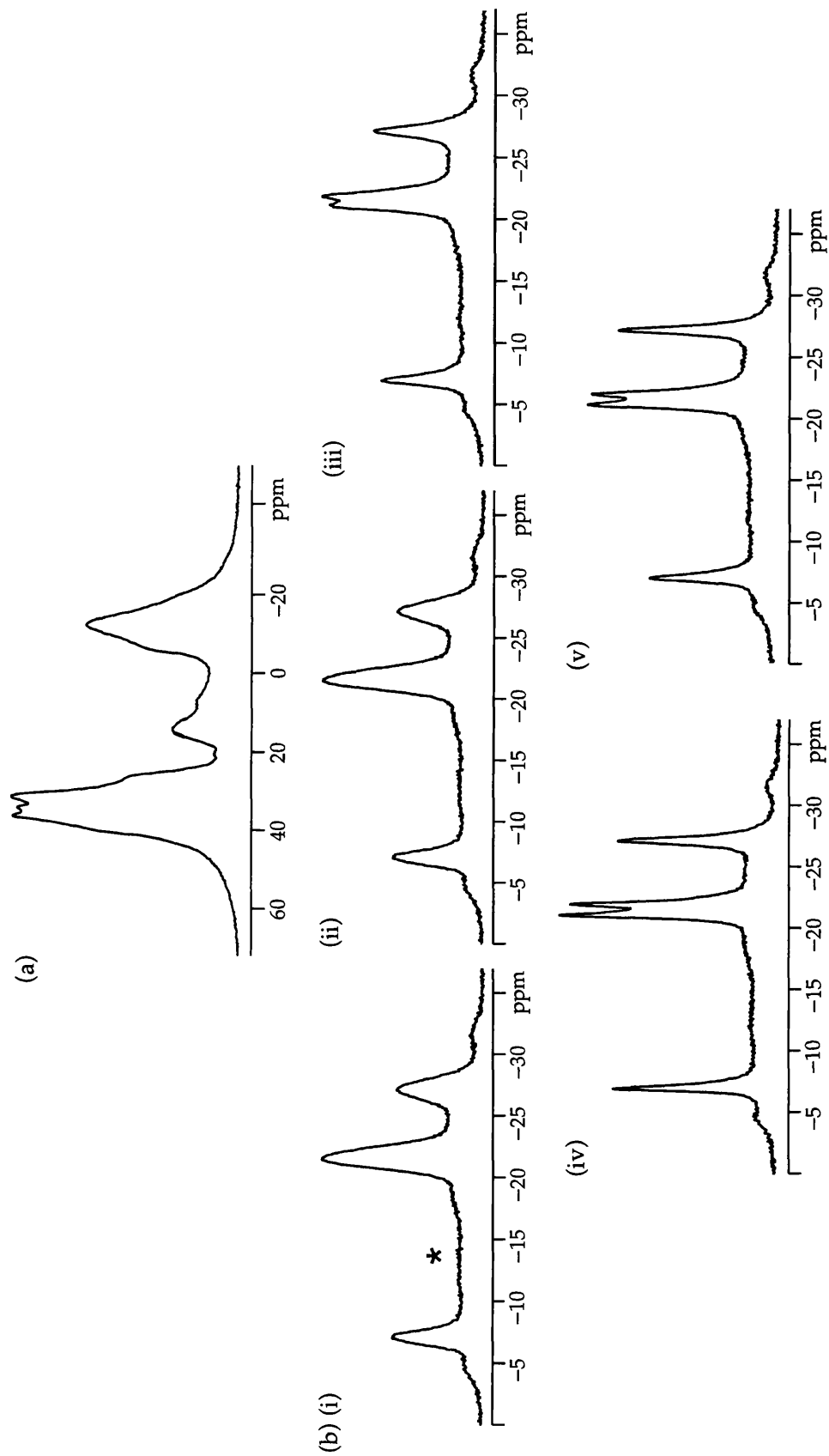


Figure 6.6: AlPO-14 *pip* MAS NMR spectra. (a)  $^{27}\text{Al}$ , (b)  $^{31}\text{P}$  MAS NMR (i) not decoupled, (ii)  $^1\text{H}$  decoupled, (iii)  $^{27}\text{Al}$  decoupled, (iv) 70 kHz  $^1\text{H}$  and 6.5 kHz  $^{27}\text{Al}$  decoupled and (v) 70 kHz  $^1\text{H}$  and 8.5 kHz  $^{27}\text{Al}$  decoupled spectrum. Spectra were recorded using (a) 64 transients and 5 s relaxation interval and (b) 4 transients and 180 s relaxation interval. \* marks an  $^{31}\text{P}$  impurity.

### 6.5.3 AlPO-14 *pip*

The first of the relatively unknown compounds to be studied here is AlPO-14 *pip*. It is the least investigated material of the three forms of AlPO-14 being discussed in this Chapter. Powder x-ray diffraction data was reported by Zibrowius *et al.* [6.2] but the crystal structure and framework topography were never confirmed even though, as mentioned earlier, it was suggested that it might have a similar framework to AlPO-14 *ipa*. Further evidence of the similarities present between these two as-synthesized AlPO-14 structures can be seen in Fig. 6.6. Comparing the one-dimensional NMR spectra of  $^{27}\text{Al}$  (Fig. 6.6a) and  $^{31}\text{P}$  (Fig. 6.6b) with those for AlPO-14 *ipa*, strong similarities are clearly evident. Despite these, it is also clear that, as pointed out in Ref [6.20], the AlPO-14 *pip*  $^{27}\text{Al}$  NMR spectra are broader than those of AlPO-14 *ipa*. One can also observe some differences in their NMR parameters, implying that there is a slight variation between the structures of the two templated materials. As mentioned in Section 6.5.1, this was commented on by Antonijevic *et al.* [6.20], who explained that this might be due to significant differences in the dynamics observed for AlPO-14 *ipa* and AlPO-14 *pip*. In addition, variations between the two could also be caused by differences in the local geometry at each of the framework species or in the interaction between the framework and template.

Figure 6.7 shows the MQ-J-HETCOR spectrum. As expected, it is also very similar to the AlPO-14 *ipa* spectrum shown in Fig. 6.5. As with the AlPO-14 *ipa* spectrum,  $^1\text{H}$  and  $^{27}\text{Al}$  decoupling were applied. The

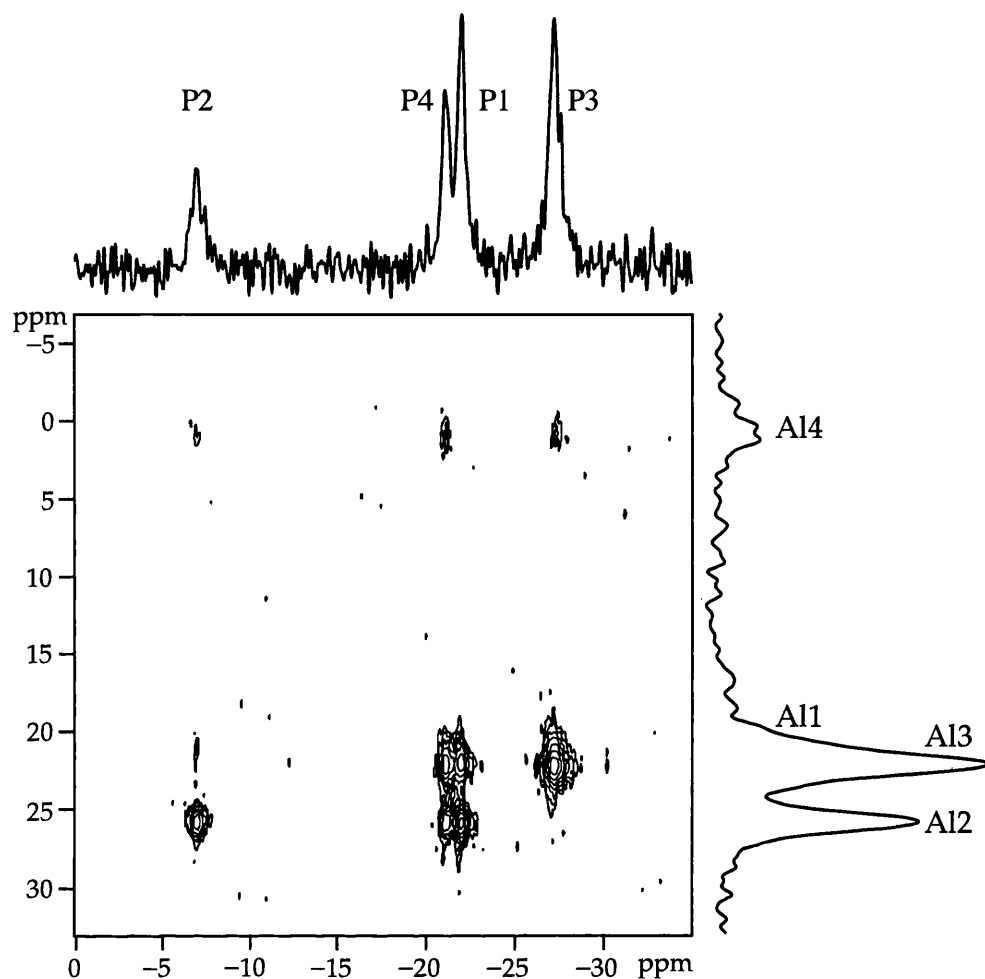


Figure 6.7: MQ-*J*-HETCOR two-dimensional spectrum recorded with 384 transients acquired for each of 256  $t_1$  increments and a relaxation interval of 2 s (and  $\delta_1$  and  $\delta_2$  projections).

optimum decoupling powers were found to be the same as those used for the other as-synthesized material; however, the  $\tau$  interval that yielded most signal was 2.0 ms long, i.e., 1.5 ms shorter. The same peaks observed in Fig. 6.5 in both  $\delta_1$  and  $\delta_2$  dimensions are present in the MQ-*J*-HETCOR spectrum of this material, further confirming that the same Al-O-P connectivities are present in the framework. In addition, calcined-dehydrated AlPO-14 is produced on calcination of AlPO-14 *pip* (i.e., the

material is identical to that produced by the calcination of AlPO-14 *ipa*), implying that both these materials have the same Al-O-P connectivity.

Consequently, the 'assignment' of peaks in AlPO-14 *pip* was possible simply by comparing the correlation spectra of the two as-synthesized materials. Confirmation of this could be achieved by looking at the individual sites and starting the assignment by labelling 'Al1' (which, interestingly, is better resolved here than it was in Fig. 6.5) since it can be readily identified as it is linked by bridging oxygens to all P species; similarly 'P4' can also be assigned. Then, we can proceed with the assignment by considering the relative intensities of the signals in cross sections taken parallel to  $\delta_2$ , all resonances can be assigned to the relevant species in the framework. Unfortunately, in this case, due to the lack of x-ray diffraction data, the NMR  $^{27}\text{Al}$  and  $^{31}\text{P}$  assignments cannot be confirmed by first-principles calculations.

As with other NMR spectra of AlPO-14 *pip*, despite the similarity to the AlPO-14 *ipa* spectra, the MQ-J-HETCOR spectrum in Fig. 6.7

Table 6.3 Experimental  $^{27}\text{Al}$  isotropic chemical shifts ( $\delta_{\text{iso}}$ ) and quadrupolar parameters (coupling constant  $C_Q$  and asymmetry  $\eta$ ) for AlPO-14 *pip*.

	$\delta_{\text{iso}}$ (ppm)	$C_Q$ / MHz	$\eta_Q$
'Al1'	28	5.9	0.5
'Al2'	46	2.9	0.8
'Al3'	39	3.2	0.1
'Al4'	-1	3.3	0.9
'P1'	-22.0		
'P2'	-7.1		
'P3'	-27.2		
'P4'	-21.0		

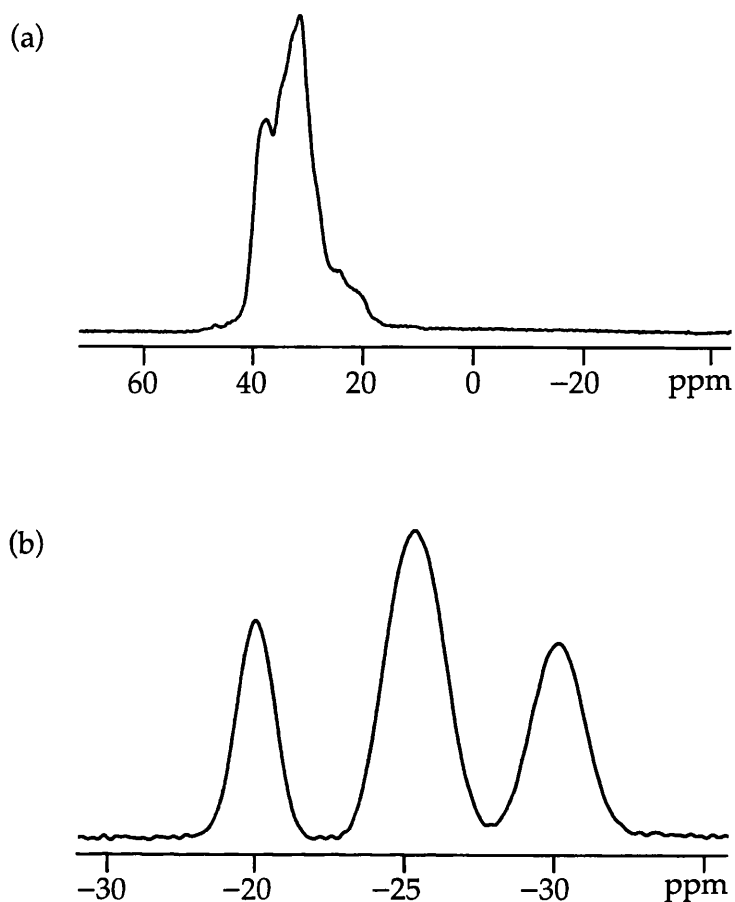


Figure 6.8: (a)  $^{27}\text{Al}$ , (b)  $^{31}\text{P}$  MAS NMR spectra of calcined-dehydrated AlPO-14 MAS NMR spectra. Spectra were recorded using (a) 64 transients and 2 s relaxation interval and (b) 4 transients and 1 s relaxation interval.

displays broader peaks (see the  $\delta_1$  projections). Furthermore, as shown in Table 6.3, the isotropic  $^{27}\text{Al}$  chemical shifts ( $\delta_{\text{CS}}$ ), the quadrupolar coupling constants ( $C_Q$ ) and the asymmetry parameter ( $\eta$ ) are different. As discussed earlier, it is easy to conclude that, even though the framework appears to be identical because of the evidence observed in the MQ-J-HETCOR spectrum, the different template might be causing slight changes in the overall structure. As pointed out by Antonijevic *et al.* [6.20] the dynamics observed in both the as-synthesized materials are very complex.

#### 6.5.4 Calcined-dehydrated AlPO-14

$^{27}\text{Al}$  and  $^{31}\text{P}$  NMR spectra of this compound have been published [6.20] but not assigned. The unit cell ( $\text{Al}_8\text{P}_8\text{O}_{32}$ ) contains four distinct Al and four distinct P species [6.3, 6.19]. Figure 6.8 shows one-dimensional NMR spectra of  $^{27}\text{Al}$  (Fig. 6.8a) and  $^{31}\text{P}$  (Fig. 6.8b). The one-dimensional  $^{27}\text{Al}$  MAS spectrum shows a resonance around  $\sim 30$  ppm, indicating tetrahedral coordination of all Al species. However, all four Al species can be resolved using MQMAS and the quadrupolar and chemical shift parameters in the literature are given in Table 6.4 [6.20]. The  $^{31}\text{P}$  MAS spectrum shows only three of the four resonances expected. Investigation of the effect of  $^1\text{H}/^{27}\text{Al}$  double-resonance decoupling on the one-dimensional  $^{31}\text{P}$  MAS NMR spectrum of this material shows that any combination of decoupling power applied did not resolve the two overlapping  $^{31}\text{P}$  sites in the spectrum. This could be because of the lack of protons present in AlPO-14 after the removal of the organic template, water, and the hydroxyl group to produce a calcined-dehydrated AlPO-14. Despite this lack of resolution in the  $^{31}\text{P}$  spectrum, the two-dimensional spectrum obtained after acquiring the MQ-J-HETCOR NMR experiment, clearly distinguishes between the two overlapping  $^{31}\text{P}$  sites at  $-27$  ppm, as seen in Fig. 6.9.

The peaks in the correlation spectrum were studied to try to match the Al-P correlations observed here with those tabulated in Table 6.1. All can be easily identified (peak at 26.5 ppm) as it correlates with all the four  $^{31}\text{P}$  sites. Similarly, the  $^{31}\text{P}$  resonance at  $-26.2$  ppm could be assigned to P4

Table 6.4 Experimental and calculated  $^{27}\text{Al}$  isotropic chemical shifts ( $\delta_{\text{iso}}$ ) and quadrupolar parameters (coupling constant  $C_Q$  and asymmetry  $\eta$ ) for calcined-dehydrated AlPO-14.

	$\delta_{\text{iso}}$ (ppm)	$C_Q$ / MHz	$\eta_Q$	$\delta_1$ (ppm)
Experimental (Ref. 20 and this work)				
A11	43	4.0	0.8	27.0
A12	43	3.4	0.2	25.7
A13	38	2.5	0.6	22.1
A14	45	4.9	0.3	29.1
P1	-21.4			
P2	-26.7			
P3	-31.5			
P4	-26.7			
Calculated (no optimization)				
A11	38.5	5.30	0.08	26.1
A12	48.6	9.69	0.26	43.7
A13	40.3	-5.55	0.74	28.6
A14	55.9	-7.04	0.57	40.4
P1	-33.5			
P2	-24.0			
P3	-35.7			
P4	-35.8			
Calculated (optimization of all atomic coordinates only)				
A11	46.5	-3.72	0.95	28.7
A12	46.8	-3.44	0.48	27.9
A13	41.8	-2.22	0.37	23.9
A14	48.7	-4.50	0.27	30.4
P1	-19.3			
P2	-25.6			
P3	-30.3			
P4	-24.5			
Calculated (optimization of all atomic coordinates and unit cell parameters)				
A11	43.2	4.54	0.74	28.0
A12	43.8	-3.57	0.25	26.3
A13	38.0	-2.80	0.71	22.5
A14	46.6	-4.96	0.26	30.0
P1	-21.4			
P2	-26.6			
P3	-32.9			
P4	-25.3			

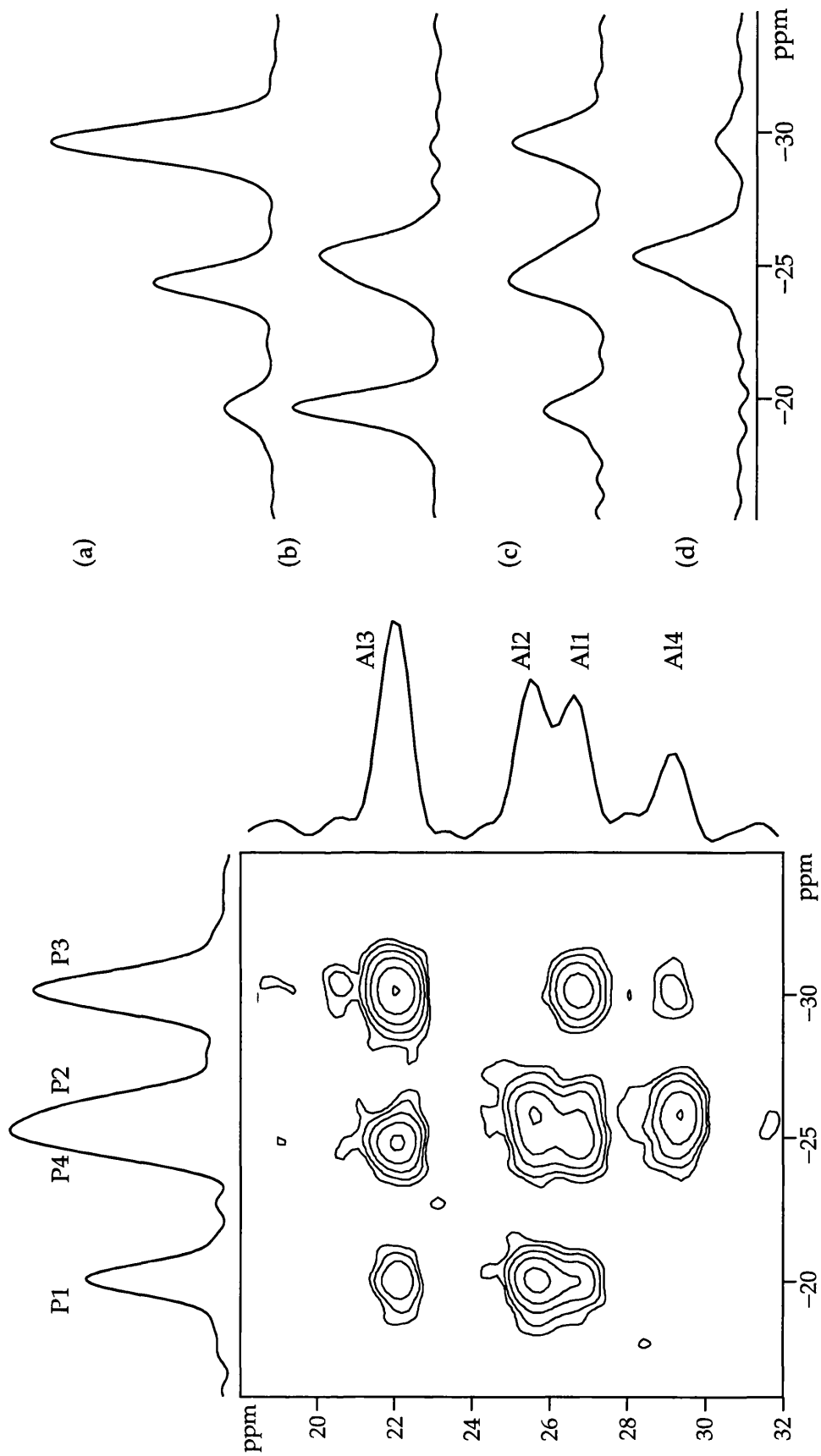


Figure 6.9: MQ-J-HETCOR two-dimensional spectrum (and  $\delta_1$  and  $\delta_2$  projections) recorded with 576 transients acquired for each of 512  $t_1$  increments and a relaxation interval of 1.5 s, as well as  $\delta_2$  cross-sections of (a) Al3, (b) Al2, (c) Al1 and (d) Al4 sites.

For the other assignment, the intensities of the peaks in the cross-sections of each Al site (Fig. 6.9 a–d) were used by matching the most intense peak in spectra a, b and d, to the doubly populated sites marked as '2' in Table 6.1, i.e., resonances containing two different Al-O-P connectivities between two species. The direct dimension of the MQ-J-HETCOR experiment was also assigned by comparison to the published information tabulated in Table 6.1. For example, Al3 exhibits cross peaks with three of the P resonances, but that at -31.9 ppm is significantly more intense, indicating this resonance can be assigned as P3. This is not a very accurate method to assign such spectra as it is unlikely that this correlation spectrum is fully quantitative. Consequently, confirmation of this assignment was only possible after CASTEP calculations were carried out. Table 6.4 lists the NMR parameters obtained from both the first-principles calculation and experiment. It should be noted, that once again, the NMR CASTEP calculation performed using the values obtained after all atomic coordinates and the unit cell parameters were optimized gave the best agreement with the experimental parameters. In most cases, typical bond distances changes from the original structure of ~0.1 Å are observed, with the exception of a few distances, e.g., Al1 – O5, Al2 - O12 and Al2 – O4, where the change is considerably larger (0.07 – 0.1 Å).

## 6.6 AIPO-53: Results and Discussion

### 6.6.1 AIPO-53: An overview

Unlike AIPO-14, AIPO-53 has not previously been studied by NMR. Kirchner *et al.* [6.4] have published structural information on three forms of AIPO-53, two of which will be discussed here. AIPO-53(A) is the as-synthesized form with methylamine as its template (AIPO-53(A)), while AIPO-53(B) is a calcined-dehydrated form of the material.

AIPO-53(B) is the simpler of the two materials. It is produced by heating the as-synthesized material (AIPO-53(A)) up to 400 °C for 45 hours and then dehydrating at a temperature of 300 °C [6.4]. The unit cell composition of this material is given as  $\text{Al}_{24}\text{P}_{24}\text{O}_{96}$  [6.4]. It consists of alternating  $\text{AlO}_4$  and  $\text{PO}_4$  tetrahedra that form a highly distorted 4-, 6- and 8-ring channel system. The XRD data reports three distinct P sites and three distinct Al sites.

The as-synthesized material is templated with methylamine ( $\text{Al}_6\text{P}_6\text{O}_{24}(\text{OH})_2 \cdot 2\text{CH}_3\text{NH}_3 \cdot 2\text{H}_2\text{O}$ ), here referred to as AIPO-53(A), and is isotypic with several other materials of its kind, such as JDF-2 [6.21] and AIPO-EN3 [6.22]. The fact that a large variety of synthesis conditions yield materials with the same topology makes it rather difficult to be sure that AIPO-53(A) is obtained. All the materials produced have very unusual structures as in addition to the  $\text{PO}_4$  and  $\text{AlO}_4$  tetrahedra found in

all the AlPOs discussed in this chapter, their frameworks also contain  $\text{AlO}_4\text{-OH-AlO}_4$  units producing a five-coordinate distorted trigonal-bipyramidal Al sites. X-ray data predicts six distinct Al sites and six distinct P sites for this material making it the most complex AlPO that will be discussed here.

### 6.6.2 Calcined-dehydrated AlPO-53(B)

Figure 6.10 shows MAS NMR spectra of AlPO-53(B). The  $^{27}\text{Al}$  MAS NMR spectrum recorded at 9.4 T (Fig. 6.10a) appears to be made up of three distinct Al sites, two at shifts of 41 and 35 ppm, with another broader peak lying between 12 and 30 ppm. The  $^1\text{H}$  and  $^{27}\text{Al}$  decoupled  $^{31}\text{P}$  MAS NMR spectrum (Fig. 6.10b) reveals three peaks, with shifts of -27.6, -30.4 and -32.0 ppm. The apparent number of sites in each spectrum agrees with the XRD data available [6.4]. Unlike calcined-dehydrated AlPO-14,  $^1\text{H}/^{27}\text{Al}$  decoupling did resolve all of the three P sites in the  $^{31}\text{P}$  MAS spectrum, with the highest resolution being achieved when the same  $^1\text{H}$  and  $^{27}\text{Al}$  decoupling powers were used as in the  $^{31}\text{P}$  spectra presented earlier in this chapter. Figure 6.11 shows the (a) 52.2 MHz and (b) 104.3 MHz  $^{27}\text{Al}$  split- $t_1$  MQMAS spectra. The spectrum acquired at the lower field was essential for extracting the NMR parameters for this material, as two of the three Al sites in the MQMAS spectrum recorded at 104.3 MHz are overlapping, making it more difficult to fit and extract the needed data. Table 6.5 lists the NMR parameters obtained as well as those calculated using NMR CASTEP.

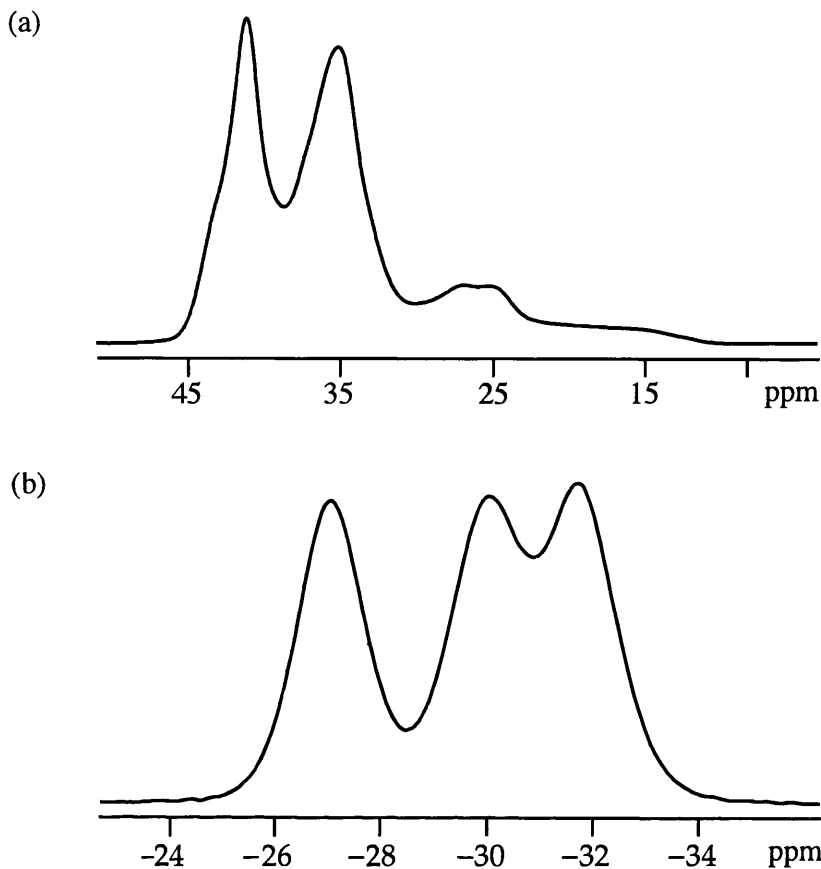


Figure 6.10: (a)  $^{27}\text{Al}$  and (b)  $^{31}\text{P}$  MAS NMR of AlPO-53(B). Spectra were recorded using (a) 64 transients and 5 s relaxation interval and (b) 4 transients and 180 s relaxation interval.

Because of the overlapping sites in the MQMAS spectrum recorded at 9.4 T, the MQ-J-HETCOR experiment would not yield a useful result, while simultaneous  $^1\text{H}$  and  $^{27}\text{Al}$  decoupling were not available at 4.7 T. However, the HMQC experiment described in Section 6.3.2 is here sufficient to resolve both  $^{27}\text{Al}$  and  $^{31}\text{P}$  spectra as can be judged from Fig. 6.10. Figure 6.12 shows the HMQC spectrum of AlPO-53(B), which correlates the  $^{27}\text{Al}$  coherences ( $\delta_2$ ) with the  $^{31}\text{P}$  coherences ( $\delta_1$ ). Unfortunately, as could have been predicted from the structure, this is not a very useful spectrum for the purposes of assignment, as it shows that each of the three P sites are correlated with all three Al sites (refer to

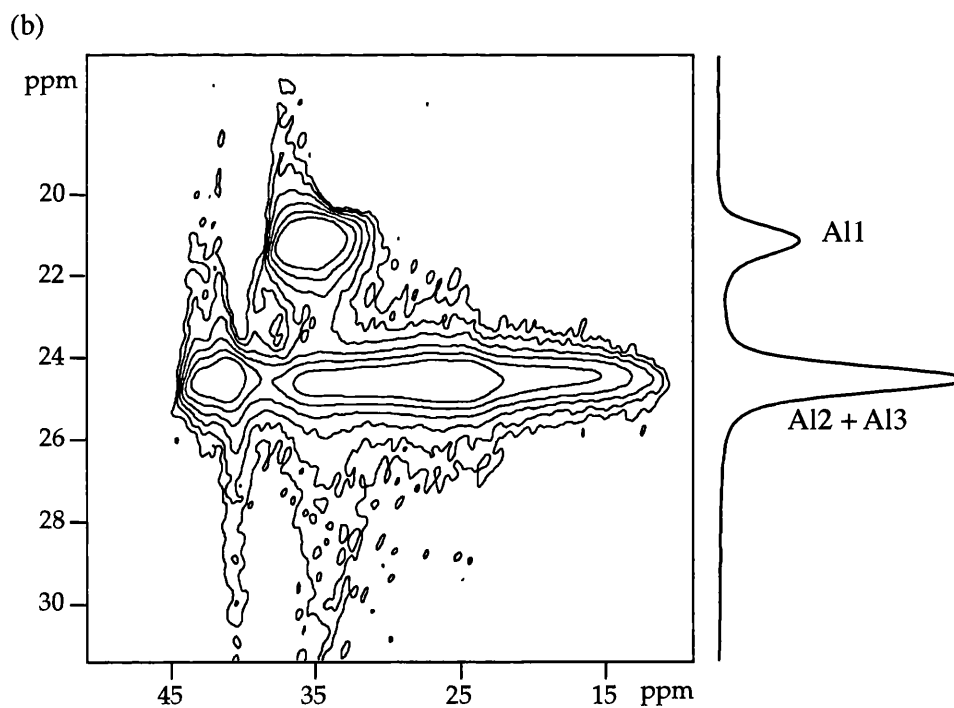
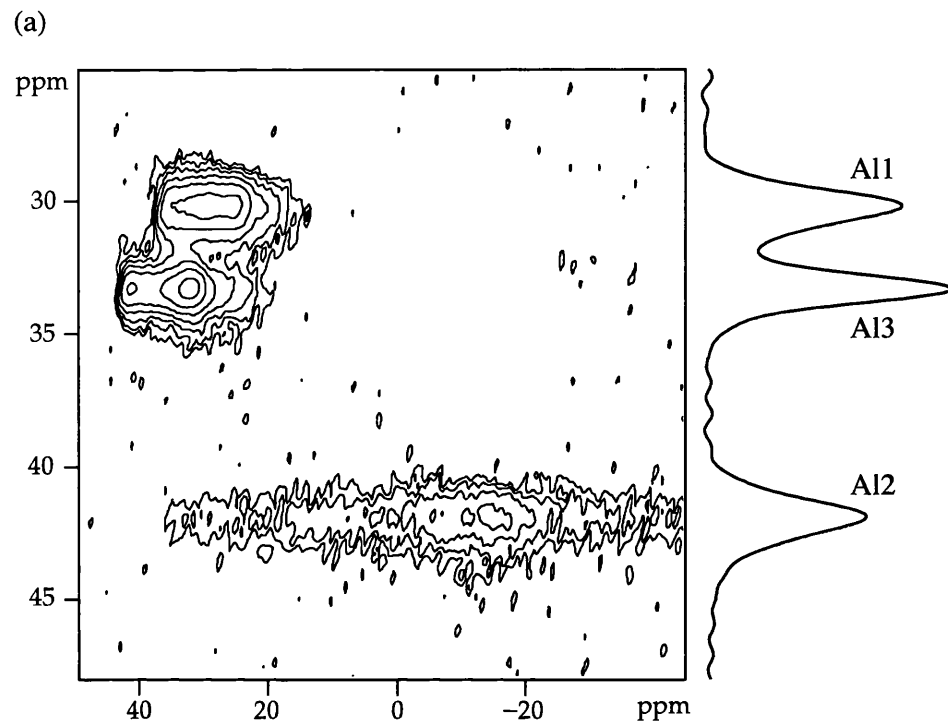


Figure 6.11:  $^{27}\text{Al}$  MQMAS (shown in Figure 3.7 b) NMR spectra of AlPO-53(B) recorded at (i) 4.7 T and (ii) 9.4 T, with 288 and 192 transients acquired for each of 80  $t_1$  increments, respectively, and a relaxation interval of 3 s.

Table 6.5: Experimental and calculated  $^{27}\text{Al}$  isotropic chemical shifts ( $\delta_{\text{iso}}$ ) and quadrupolar parameters (coupling constant  $C_Q$  and asymmetry  $\eta_Q$ ) for calcined-dehydrated AIPO-53 (AIPO-53(B)).

	$\delta_{\text{iso}}$ (ppm)	$C_Q$ / MHz	$\eta_Q$
Experimental (This work)			
Al1	37	1.9	0.5
Al2	36	4.0	0.9
Al3	43	1.9	0.8
P1	-32.0		
P2	-30.4		
P3	-27.6		
Calculated (no optimization)			
Al1	50	5.9	0.9
Al2	44	6.5	0.9
Al3	50	5.0	0.7
P1	-31.3		
P2	-25.8		
P3	-23.9		
Calculated (optimization of all atomic coordinates only)			
Al1	41.9	2.0	0.6
Al2	43.5	3.8	0.8
Al3	48.2	2.1	0.9
P1	-31.8		
P2	-30.3		
P3	-25.9		
Calculated (optimization of all atomic coordinates and unit cell parameters)			
Al1	37	1.90	0.9
Al2	38	4.37	0.8
Al3	44	2.07	0.9
P1	-32.5		
P2	-31.0		
P3	-27.7		

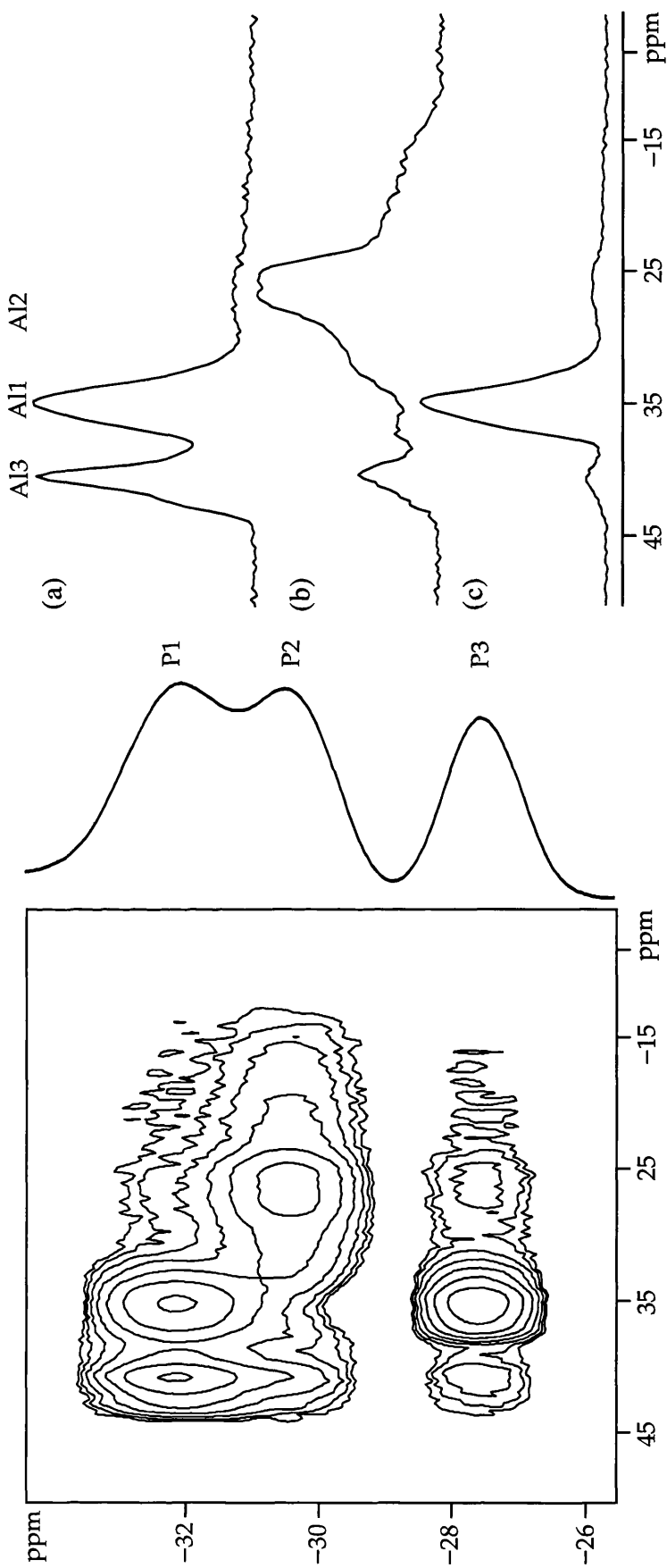


Figure 6.12:  $^{27}\text{Al} - ^{31}\text{P}$  HMQC two-dimensional spectrum of AlPO-53(B) (and  $\delta_1$  projection), recorded with 160 transients acquired for each of 128  $t_1$  increments and a relaxation interval of 3 s and  $\delta_2$  cross-sections ((a) - (c)) show the three  $^{27}\text{Al}$  sites (Al3, Al1 and Al2 respectively) correlated with every  $^{31}\text{P}$  site.

Fig. 6.12). Consequently, peak assignment is not possible solely by studying the NMR spectra.

However, NMR CASTEP calculations, using the x-ray diffraction data available were also performed. Once again, energy-minimization to optimize the geometry of the system was carried out before more accurate NMR parameters were obtained. Both sets of calculated NMR parameters together with the experimental NMR parameters are listed in Table 6.5. Comparing these parameters, assignment of the three Al sites was possible. The assignment of the  $^{31}\text{P}$  spectrum was also made possible by results obtained from the same first-principles calculation. The assignments are labelled on the spectra in Fig. 6.12.

### 6.6.3 *AlPO-53(A)*

The XRD structure of *AlPO-53(A)* (Kirchner *et al.* [6.4]) predicts six distinct Al sites, two four-coordinate and four five-coordinate, and six distinct P sites. NMR experiments on this material, performed over a period of time, indicated that the same sample packed in the same rotor was yielding different spectra every time the experiment was performed. It became evident that *AlPO-53(A)* spontaneously dehydrates over time, making NMR study of this material very difficult indeed. It was also found that full dehydration of as-synthesized *AlPO-53* produces an isotopic material known as JDF-2 [6.21]. The x-ray data shows that, unlike *AlPO-53(A)*, the structure of JDF-2 only contains three distinct Al sites,

one four-coordinate and two five-coordinate, as well as three distinct P sites. The chemical formula for JDF-2 is  $\text{Al}_3\text{P}_3\text{O}_{12}(\text{OH})\cdot\text{CH}_3\text{NH}_3$ .

Full dehydration of AIPO-53(A) to produce JDF-2 was achieved by heating the sample to 100 °C. Note that this will not remove the templating agent, as occurs during calcination, but only ensures that dehydration is complete. It was observed that JDF-2 tends to rehydrate upon exposure to air partly, forming AIPO-53(A) again. A possible way this interconversion occurs is given by the following chemical equation:



Consequently, to ensure that JDF-2 was the material being studied, it was heated prior to every NMR study conducted.

Calcination of both these AIPOs yield the same calcined-dehydrated material, AIPO-53(B), discussed in the previous section. The following chemical equations demonstrate this process:



As shown in Fig. 6.13a, evidence of interconversion is very clear from the  $^{31}\text{P}$  spectra of these materials. The  $^{31}\text{P}$  MAS NMR spectrum of JDF-2 (Fig. 6.13a(i)) consists of two peaks in a ratio of 1 : 2, at chemical shifts of -14 and -25 ppm, respectively. The AIPO-53(A)  $^{31}\text{P}$  spectrum (Fig. 6.13a(iv)), is made up of four peaks in a ratio of 1 : 1 : 2 : 2, at chemical shifts of

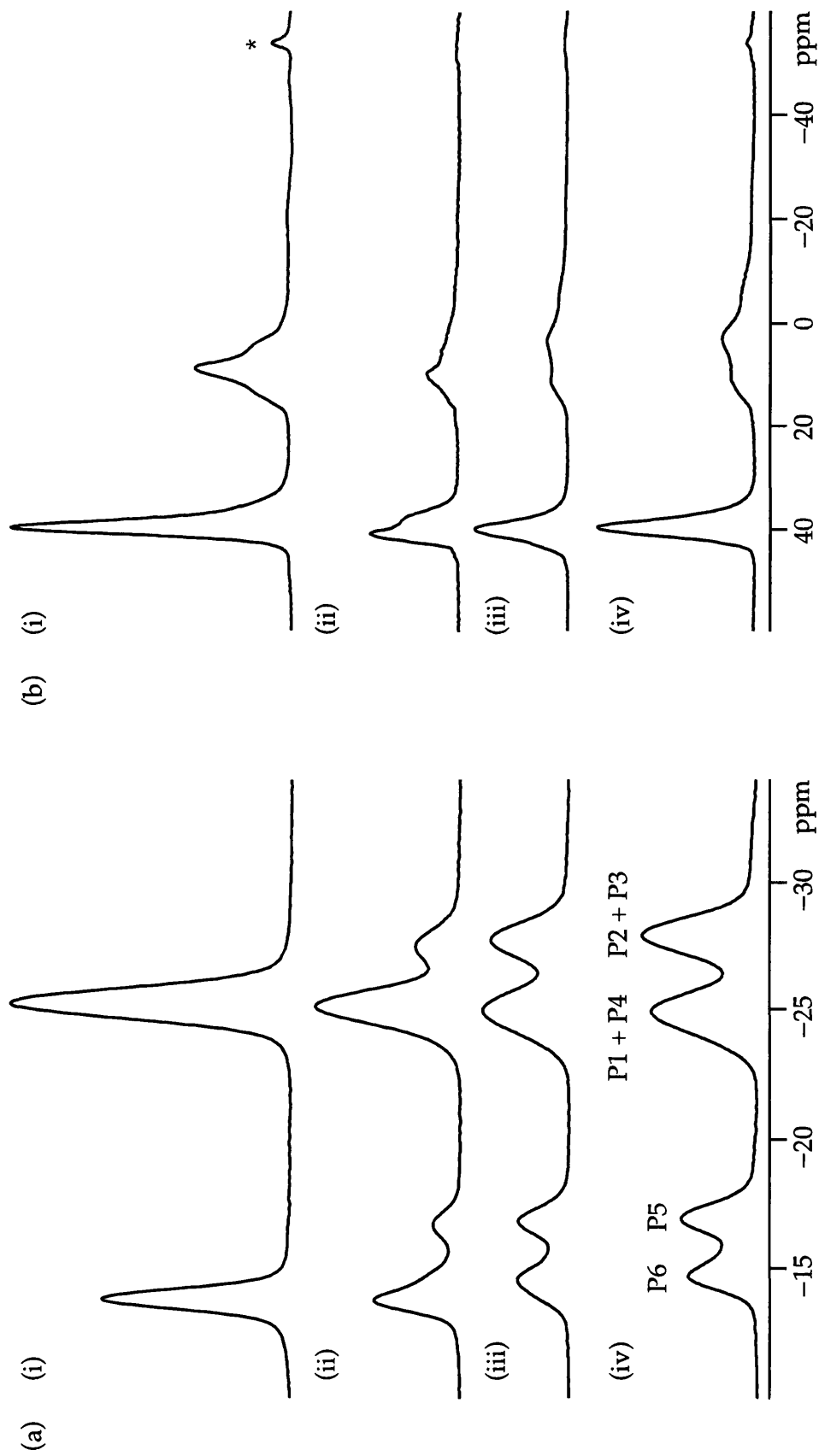


Figure 6.13: (a)  $^{31}\text{P}$  and (b)  $^{27}\text{Al}$  MAS NMR spectra of (i) JDF-2 as it gets transformed into (iv) AlPO-53(A). (ii) and (iii) two intermediate stages during the transformation period, recorded after (ii) three months and (iii) five months from when JDF-2 was synthesized. Spectra were recorded using (a) 4 transients and 180 s relaxation interval and (b) 64 transients and 5 s relaxation interval and (b). \* marks a spinning sideband.

around -15, -17, -25, and -28 ppm, respectively. Figs. 6.13a(ii and iii) show two intermediate stages in the conversion of JDF-2 into AlPO-53(A). The spectrum in Fig. 6.13a(ii) was recorded after three months since the date of synthesis, while the material that produced the spectrum in Fig. 6.13a(iii) was left to stand for five months.

Figure 6.13b shows  $^{27}\text{Al}$  MAS NMR spectra of JDF-2 (Fig. 6.13b(i)) and AlPO-53(A) (Fig. 6.13b(iv)) and two intermediate stages (ii and iii) showing JDF-2 slowly hydrating as explained by the reaction (6.1). None of the spectra resolve all the  $^{27}\text{Al}$  sites predicted by the XRD data. The  $^{27}\text{Al}$  spectra i-iv in Fig. 6.13a all show two well resolved peaks and one very broad underlying resonance. To try to resolve more of the sites predicted by the XRD data,  $^{27}\text{Al}$  MQMAS NMR experiments needed to be performed at every stage during the transformation between JDF-2 and AlPO-53(A).

Since it was concluded that JDF-2 was the only material whose transformation could be controlled, it seemed reasonable to continue the investigation into the as-synthesized AlPO-53 by getting a better understanding of the NMR spectra produced by JDF-2. An  $^{27}\text{Al}$  split- $t_1$  MQMAS spectrum of JDF-2 is shown in Fig. 6.14a. The spectrum shows three crystallographically distinct Al sites, which were fitted to extract their NMR parameters. The narrow peak at a  $\delta_2$  shift of 43 ppm corresponds to a four-coordinate Al site, while a relatively intense second-order broadened resonance lying between -5 and 10 ppm in the  $\delta_2$  dimension and a low-intensity feature lying between around -44 and 0

Table 6.6: Experimental and calculated  $^{27}\text{Al}$  and  $^{31}\text{P}$  isotropic chemical shifts ( $\delta_{\text{iso}}$ ) and  $^{27}\text{Al}$  quadrupolar parameters (coupling constant  $C_Q$  and asymmetry  $\eta$ ) for JDF-2 obtained from experimental data in Fig. 6.14a.

	$\delta_{\text{iso}}$ (ppm)	$C_Q$ / MHz	$\eta_Q$
Experimental (This work)			
Al1	17.9	6.7	0.2
Al2	18.9	2.9	0.4
Al3	45.4	1.7	0.5
P1	-25.3		
P2	-13.9		
P3	-25.3		
Calculated (no optimization)			
Al1	22.6	6.9	0.4
Al2	22.9	3.1	1.0
Al3	49.6	2.0	0.1
P1	-28.5		
P2	-17.8		
P3	-26.7		
Calculated (optimization of all atomic coordinates only)			
Al1	25.4	7.8	0.9
Al2	23.0	4.1	0.4
Al3	48.9	1.6	0.6
P1	-24.5		
P2	-9.1		
P3	-22.4		
Calculated (optimization of all atomic coordinates and unit cell parameters)			
Al1	22.5	7.1	1.0
Al2	19.9	3.4	0.2
Al3	46.0	1.7	1.0
P1	-25.4		
P2	-8.9		
P3	-24.8		

ppm in the  $\delta_2$  dimension correspond to five-coordinate Al sites. These results thus confirm the predicted three Al sites. NMR CASTEP calculations were performed using the x-ray data in Ref. [6.21] to obtain the NMR parameters of this material. Table 6.6 compares these to the experimental values, yielding the assignment shown in Fig. 6.14a.

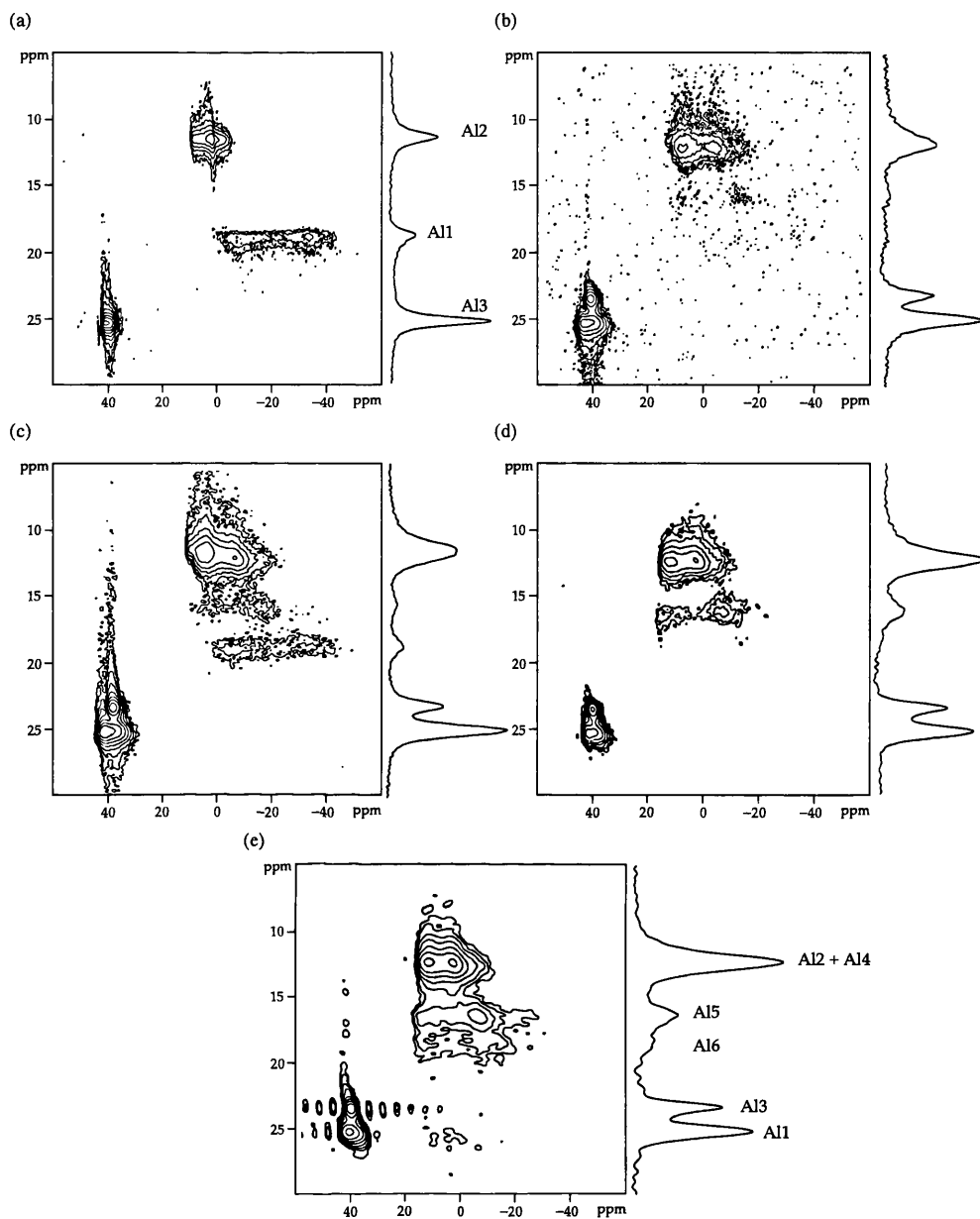


Figure 6.14:  $^{27}\text{Al}$  MQMAS (shown in Figure 3.7 b) NMR spectra of (a) JDF-2, JDF-2 as it gets hydrated by standing in air (b) in a rotor and (c) in an open container for five months. (d) and (e) AIPO-53(A) recorded using a  $\tau$  interval of 4 ms and 2 ms respectively. All spectra were recorded with 96 transients for each 128  $t_1$  increments and a relaxation interval of 4 s.

Figures 6.14b and 6.14c are split- $t_1$  MQMAS spectra of the same batch of JDF-2; however, they were acquired after a sample was left to stand in the MAS rotor (b) and in an open sample bottle (c) for five months. The spectrum in Fig. 6.14b now consists of three intense peaks and one very weak peak. Only the peak at the highest  $\delta_1$  shift ( $\sim 25$  ppm) lies at the same frequency as that in the original JDF-2 spectrum labelled Al3. The peak labelled Al1 in Fig. 6.14a is not present and the remaining peak has shifted slightly to a higher frequency. In addition, a very weak and broad resonance is also observed at around 16 ppm. On the other hand, the spectrum in Fig. 6.14c seems to have five distinct Al peaks, the four already present in Fig. 6.14b and an additional one lying at the same frequency as the peak labelled Al1 in the original JDF-2 spectrum. The spectrum in Fig. 6.14c is possibly evidence of a mixture of JDF-2 and partly rehydrated forms of the material.

Finally, Figs. 6.14d and 6.14e show split- $t_1$  MQMAS spectra of what is believed to be AlPO-53(A). The difference between spectra (d) and (e) is the length of the  $\tau$  (echo) interval used. (d) was recorded using a  $\tau$  interval of 4 ms while spectrum (e) was recorded using an interval of just 2 ms. This was done to help make visible any broader components of the AlPO-53(A) lineshape that could be suppressed when long time intervals are used due to their short  $T_2$ . This compromise, of course, results in severe truncation of the sharper parts of the lineshape as is clearly seen in Fig. 6.14e. However, at least one very broad new site at a  $\delta_1$  shift of  $\sim 19$  ppm could be observed in this spectrum that could not be seen in spectrum (d). Consequently, five Al peaks are observed in total, two

Table 6.7: Experimental and calculated  $^{27}\text{Al}$  and  $^{31}\text{P}$  isotropic chemical shifts ( $\delta_{\text{iso}}$ )  $^{27}\text{Al}$  quadrupolar parameters (coupling constant  $C_Q$  and asymmetry  $\eta$ ) for AlPO-53(A).

	$\delta_{\text{iso}}$ (ppm)	$C_Q$ / MHz	$\eta_Q$
Experimental (This work)			
Al1	44.0	2.6	0.37
Al2	17.8	4.4	0.21
Al3	41.8	1.8	0.56
Al4	/	/	/
Al5	23.7	6.3	0.25
Al5	§	§	§
P1	-25.1		
P2	-27.8		
P3	-27.8		
P4	-25.1		
P5	-16.9		
P6			
§ the intensity of this peak is too low to allow for the extraction of NMR parameters			
Calculated (optimization of all atomic coordinates and unit cell parameters)			
Al1	42.5	2.5	0.38
Al2	16.6	3.4	0.30
Al3	41.5	-2.1	0.92
Al4	16.7	-3.3	0.44
Al5	19.1	5.4	0.94
Al6	17.8	7.0	0.88
P1	-24.3		
P2	-29.7		
P3	-28.7		
P4	-27.0		
P5	-15.6		
P6	-14.0		

relatively narrow, and three broad. Therefore, from these results, it could be concluded that the sixth and last peak is either overlapping with one of the three broad peaks visible in Fig. 6.14e, or else it is too broad to be resolved at this magnetic field.

However, NMR CASTEP calculations of AlPO-53(A) shown in Table 6.7, show that Al2 and Al4 has almost identical  $\delta_{\text{iso}}$ , hence implying

that the peak at a  $\delta_1$  shift of around 13 ppm contains two Al sites. Hence it can be concluded that Al1 and Al3 are the four-coordinate components of the structure, while Al2, Al3, Al4 and Al6 are the five-coordinate sites (labelled on Fig. 6.14e). Also shown in Table 6.7 are the experimental and calculated isotropic chemical shifts of the six  $^{31}\text{P}$  sites present (labelled in Figure 6.13).

## 6.7 Conclusions

The enhanced resolution obtained by using MQMAS and heteronuclear decoupled NMR spectra has been used to confirm MAS NMR spectra assignments of the well known AlPO-14 *ipa* and make new assignments of other, less well known aluminophosphates. All the experimental assignments were confirmed by first-principles calculations.

Furthermore, NMR of two AlPO-53 forms; the as-synthesized form, AlPO-53(A) and the calcined-dehydrated form AlPO-53(B), as well as the related JDF-2 were presented for the first time here. Despite the complexity of this structure, the combination of results obtained from MAS NMR and *ab initio* calculations of these materials allowed for the successful assignment of all the  $^{27}\text{Al}$  and  $^{31}\text{P}$  MAS NMR spectra.

---

## Appendix A

### Matrix Representations of Cartesian Spin Angular Momentum Operators

---

Spin  $I = 1/2$

$$I_x = \frac{1}{2} \begin{pmatrix} 0 & 1 \\ 1 & 0 \end{pmatrix} \quad I_y = \frac{i}{2} \begin{pmatrix} 0 & -1 \\ 1 & 0 \end{pmatrix} \quad I_z = \frac{1}{2} \begin{pmatrix} 1 & 0 \\ 0 & -1 \end{pmatrix}$$

Spin  $I = 1$

$$I_x = \frac{1}{\sqrt{2}} \begin{pmatrix} 0 & 1 & 0 \\ 1 & 0 & 1 \\ 0 & 1 & 0 \end{pmatrix} \quad I_y = \frac{i}{\sqrt{2}} \begin{pmatrix} 0 & -1 & 0 \\ 1 & 0 & -1 \\ 0 & 1 & 0 \end{pmatrix} \quad I_z = \begin{pmatrix} 1 & 0 & 0 \\ 0 & 0 & 0 \\ 0 & 0 & 1 \end{pmatrix}$$

Spin  $I = 3/2$

$$I_x = \frac{1}{2} \begin{pmatrix} 0 & \sqrt{3} & 0 & 0 \\ \sqrt{3} & 0 & 2 & 0 \\ 0 & 2 & 0 & \sqrt{3} \\ 0 & 0 & \sqrt{3} & 0 \end{pmatrix} \quad I_y = \frac{i}{2} \begin{pmatrix} 0 & -\sqrt{3} & 0 & 0 \\ \sqrt{3} & 0 & -2 & 0 \\ 0 & 2 & 0 & -\sqrt{3} \\ 0 & 0 & \sqrt{3} & 0 \end{pmatrix} \quad I_z = \frac{1}{2} \begin{pmatrix} 3 & 0 & 0 & 0 \\ 0 & 1 & 0 & 0 \\ 0 & 0 & -1 & 0 \\ 0 & 0 & 0 & -3 \end{pmatrix}$$

Spin  $I = 5/2$

$$I_x = \frac{1}{2} \begin{pmatrix} 0 & \sqrt{5} & 0 & 0 & 0 & 0 \\ \sqrt{5} & 0 & \sqrt{8} & 0 & 0 & 0 \\ 0 & \sqrt{8} & 0 & 3 & 0 & 0 \\ 0 & 0 & 3 & 0 & \sqrt{8} & 0 \\ 0 & 0 & 0 & \sqrt{8} & 0 & \sqrt{5} \\ 0 & 0 & 0 & 0 & \sqrt{5} & 0 \end{pmatrix} \quad I_y = \frac{i}{2} \begin{pmatrix} 0 & -\sqrt{5} & 0 & 0 & 0 & 0 \\ \sqrt{5} & 0 & -\sqrt{8} & 0 & 0 & 0 \\ 0 & \sqrt{8} & 0 & -3 & 0 & 0 \\ 0 & 0 & 3 & 0 & -\sqrt{8} & 0 \\ 0 & 0 & 0 & \sqrt{8} & 0 & -\sqrt{5} \\ 0 & 0 & 0 & 0 & \sqrt{5} & 0 \end{pmatrix}$$

$$I_z = \frac{1}{2} \begin{pmatrix} 5 & 0 & 0 & 0 & 0 & 0 \\ 0 & 3 & 0 & 0 & 0 & 0 \\ 0 & 0 & 1 & 0 & 0 & 0 \\ 0 & 0 & 0 & -1 & 0 & 0 \\ 0 & 0 & 0 & 0 & -3 & 0 \\ 0 & 0 & 0 & 0 & 0 & -5 \end{pmatrix}$$

---

## Appendix B

### Matrix Representations of Irreducible Spherical Tensor Operators

---

Spin  $I = 1$

	$T_{0,p}$	$T_{1,p}$	$T_{2,p}$
$p = 2$			$\begin{pmatrix} 0 & 0 & 1 \\ 0 & 0 & 0 \\ 0 & 0 & 0 \end{pmatrix}$
$p = 1$		$\begin{pmatrix} 0 & -1 & 0 \\ 0 & 0 & -1 \\ 0 & 0 & 0 \end{pmatrix}$	$\frac{1}{\sqrt{2}} \begin{pmatrix} 0 & -1 & 0 \\ 0 & 0 & 1 \\ 0 & 0 & 0 \end{pmatrix}$
$p = 0$	$\begin{pmatrix} 1 & 0 & 0 \\ 0 & 1 & 0 \\ 0 & 0 & 1 \end{pmatrix}$	$\begin{pmatrix} 1 & 0 & 0 \\ 0 & 0 & 0 \\ 0 & 0 & -1 \end{pmatrix}$	$\frac{1}{\sqrt{6}} \begin{pmatrix} 1 & 0 & 0 \\ 0 & -2 & 0 \\ 0 & 0 & 1 \end{pmatrix}$
$p = -1$		$\begin{pmatrix} 0 & 0 & 0 \\ 1 & 0 & 0 \\ 0 & 1 & 0 \end{pmatrix}$	$\frac{1}{\sqrt{2}} \begin{pmatrix} 0 & 0 & 0 \\ 1 & 0 & 0 \\ 0 & -1 & 0 \end{pmatrix}$
$p = -2$			$\begin{pmatrix} 0 & 0 & 0 \\ 0 & 0 & 0 \\ 1 & 0 & 0 \end{pmatrix}$

## References

---

- 1.1 E. M. Purcell, H. C. Torrey and R. V. Pound, *Phys. Rev.* **69**, 37 (1946).
- 1.2 F. Bloch, W. W. Hansen and M. Packard, *Phys. Rev.* **70**, 474 (1946).
- 1.3 R. R. Ernst, *J. Magn. Reson.* **4**, 51 (1971).
- 1.4 J. Jeener, Lecture presented at Ampere International Summer School II, Basko Polje, Yugoslavia (1971).
- 1.5 E. R. Andrew, A. Bradbury and R. G. Eades, *Nature* **182**, 1659 (1958)
- 1.6 E. R. Andrew, A. Bradbury and R. G. Eades, *Nature* **183**, 1802 (1959).
- 1.7 E. R. Andrew, in "Encyclopedia of Nuclear Magnetic Resonance" (D. M. Grant and R. K. Harris, Eds.), Vol. 3, p. 2891, Wiley, Chichester, 1996.
- 1.8 A. Pines, M. G. Gibby and J. S. Waugh, *J. Chem. Phys.* **59**, 569 (1973).
- 1.9 A. Samonson, E. Lippmaa and A. Pines, *Mol. Phys.* **65**, 1013 (1988).
- 1.10 A. Samonson and E. Lippmaa, *J. Magn. Reson.* **84**, 410 (1989).
- 1.11 K. T. Mueller, B. Q. Sun, G. C. Chingas, J. W. Zwanziger, T. Terao and A. Pines, *J. Magn. Reson.* **86**, 470 (1990).
- 1.12 L. Frydman and J. S. Harwood, *J. Am. Chem. Soc.* **117**, 5367 (1995).
- 1.13 Z. Gan, *J. Am. Chem. Soc.* **122**, 3242 (2000).
- 1.14 M. Cutajar, S. E. Ashbrook and S. Wimperis, *Chem. Phys. Lett.* **423** (2006) 276.
- 1.15 M. J. Duer, "Introduction to Solid-State NMR Spectroscopy", Chapter 6, Blackwell Publishing, Oxford, 2004.
- 1.16 M. Alla, R. Ecmann and A. Pines, *Chem. Phys. Lett.* **71** (1980) 148.
- 1.17 Z. Gan and P. Robyr, *Mol. Phys.* **95** (1998) 1143.
- 1.18 J. W. Wiench and M. Pruski, *Solid State Nucl. Magn. Reson.* **26**, 51 (2004).
- 1.19 C. J. Pickard and F. Mauri, *Phys. Rev. B* **63**, 245101 (2001).

- 2.1 F. Bloch, *Phys. Rev.* **70**, 460 (1946).
- 2.2 R. R. Ernst, G. Bodenhausen and A. Wokaun, in "Principles of Nuclear Magnetic Resonance in One and Two Dimensions", p. 104, Clarendon Press, Oxford, 1987.
- 2.3 A. Abragam, in "Principles of Nuclear Magnetism", p. 33, Oxford Science Publications, 1961.
- 2.4 C. P. Slichter, in "Principles of Magnetic Resonance", p. 157, Springer-Verlag, Berlin, 1990.
- 2.5 P. W. Atkins, in "Molecular Quantum Mechanics", Chapter. 5, Oxford University Press, Oxford, 1983.
- 2.6 A. Abragam, in "Principles of Nuclear Magnetism", p. 26, Oxford Science Publications, 1961.
- 2.7 O. W. Sorensen, G. W. Eich, M. H. Levitt, G. Bodenhausen and R. R. Ernst, *Prog. NMR Spec.* **16**, 163 (1983).
- 2.8 N. Müller, G. Bodenhausen and R. R. Ernst, *J. Magn. Reson.* **75**, 297 (1987).
- 2.9 M. J. Duer, in "Introduction to Solid-State NMR Spectroscopy", p. 41, Blackwell Science Publishing, 2004.
- 2.10 M. H. Levitt, in "Spin Dynamics: basics of nuclear magnetic resonance", p. 192, John Wiley & Sons Ltd., 2001.
- 2.11 M. J. Duer, in "Introduction to Solid-State NMR Spectroscopy", Chapter 4, Blackwell Science Publishing, 2004.
- 2.12 N. Bloembergen, *Physica* **15** 386 (1949).
- 2.13 M. Alla, R. Ecmann and A. Pines, *Chem. Phys. Lett.* **71**, 148 (1980).
- 2.14 D. Suter and R. R. Ernst, *Phys. Rev. B* **32**, 5608 (1985).
- 2.15 Z. Gan and P. Robyr, *Mol. Phys.* **95**, 1143 (1998).
- 2.16 M. H. Levitt, in "Spin Dynamics: basics of nuclear magnetic resonance", p. 211, John Wiley & Sons Ltd., 2001.
- 2.17 T. A. Early, B. K. John and L. F. Johnson, *J. Magn. Reson.* **75**, 134 (1987).
- 2.18 C. A. Fyfe, Y. Feng, H. Gies, H. Grondey and G.T. Kokotailo, *J. Am. Chem. Soc.* **112**, 3264 (1990).
- 2.19 M. Baldus and B. H. Meier, *J. Magn. Reson. A* **121**, 65 (1996).
- 2.20 H. Miura, T. Terao and A. Saika, *J. Magn. Reson.* **68**, 593 (1986).

- 2.21 A. Lesage, D. Sakellariou, S. Steuernagel and L. Emsley, *J. Am. Chem. Soc.* **120**, 13194 (1998).
- 2.22 C. A. Fyfe, K. C. Wong-Moon, Y. Huang and H. Grondy, *J. Am. Chem. Soc.* **117**, 10397 (1995).
- 2.23 H.-M. Kao and C. P. Grey, *J. Magn. Reson.* **133**, 313 (1998).
- 2.24 C. A. Fyfe, H. Meyer zu Altenschildesche, K. C. Wong-Moon, H. Grondy and J. M. Chezeau, *Solid State Nucl. Magn. Reson.* **9**, 97 (1997).
- 2.25 J. W. Wiench and M. Pruski, *Solid State Nucl. Magn. Reson.* **26**, 51 (2004).
- 2.26 D. Massiot, F. Fayon, B. Alonso, J. Trebosc and J.-P. Amoureux, *J. Magn. Reson.* **164**, 160 (2003).
- 2.27 M. J. Duer, in "Introduction to Solid-State NMR Spectroscopy", Chapter 5, Blackwell Science Publishing, 2004.
- 2.28 H. A. Buckmaster, *Can. J. Phys.* **42**, 386 (1964).
- 
- 3.1 P. J. Hore, J. A. Jones and S. Wimperis in "NMR: The Toolkit", Chapter 6, Oxford University Press, Oxford, 2000.
- 3.2 G. Bodenhausen, H. Kogler and R. R. Ernst, *J. Magn. Reson.* **58**, 370 (1984).
- 3.3 E. L. Hahn, *Phys. Rev.* **80**, 580 (1950).
- 3.4 H. Y. Carr and E. M. Purcell, *Phys. Rev.* **94**, 630 (1954).
- 3.5 B. C. Gerstein, in "Encyclopaedia of Nuclear Magnetic Resonance" (D. M. Grant and R. K. Harris, Eds.), p. 1835, Wiley, Chichester, 1996.
- 3.6 J. H. Davis, K. R. Jeffrey, M. Bloom, M. I. Valic and T. P. Higgs, *Chem. Phys. Lett.* **42**, 390 (1976).
- 3.7 S. Antonijevic and S. Wimperis, *J. Magn. Reson.* **164**, 343 (2003).
- 3.8 J. Virlet, in "Encyclopaedia of Nuclear Magnetic Resonance" (D. M. Grant and R. K. Harris, Eds.), p. 2694, Wiley, Chichester, 1996.
- 3.9 E. R. Andrew, "Encyclopaedia of Nuclear Magnetic Resonance" (D. M. Grant and R. K. Harris, Eds.), p. 2891, Wiley, Chichester, 1996.
- 3.10 M. J. Duer, in "Introduction to Solid-State NMR Spectroscopy", p. 61, Blackwell Science Publishing, 2004.

- 3.11 S. E. Ashbrook and S. Wimperis, *J. Magn. Reson.* **177**, 44 (2005).
- 3.12 R. Freeman, in "A Handbook of Nuclear Magnetic Resonance", p. 88, Longman, Harlow, 1997
- 3.13 M. J. Duer, in "Introduction to Solid-State NMR Spectroscopy", p. 77, Blackwell Science Publishing, 2004.
- 3.14 Y. Y. Chen, S. Y. Luo, S. C. Hing, S. I. Chan and D. L. M. Tzou, *Carbohydrate Research*, **340**, 723 (2005).
- 3.15 L. Frydman and J. S. Harwood, *J. Am. Chem. Soc.* **117**, 5367 (1995).
- 3.16 S. P. Brown, S. J. Heyes and S. Wimperis, *J. Magn. Reson.* **A119**, 280 (1996).
- 3.17 D. Massiot, B. Touzo, D. Trumeau, J. P. Coutures, J. Virlet, P. Florian and P. J. Grandinetti, *Solid State Nucl. Magn. Reson.* **6**, 73 (1996).
- 3.18 S. P. Brown and S. Wimperis, *J. Magn. Reson.* **124**, 279 (1997).
- 3.19 S. P. Brown and S. Wimperis, *J. Magn. Reson.* **128**, 42 (1997).
- 3.20 D. J. States, R. A. Haberkorn and D. J. Ruben, *J. Magn. Reson.* **48**, 286 (1982).
- 
- 3.1 J. H. Davis, K. R. Jeffrey, M. Bloom, M. I. Valic and T. P. Higgs, *Chem. Phys. Lett.* **42** (1976) 390.
- 3.2 L. S. Batchelder, in "Encyclopedia of Nuclear Magnetic Resonance" (D. M. Grant and R. K. Harris, Eds.), Vol. 3, p. 1574, Wiley, Chichester, 1996.
- 3.3 M. J. Duer, "Introduction to Solid-State NMR Spectroscopy", Chapter 6, Blackwell Publishing, Oxford, 2004.
- 3.4 C. Schmidt, B. Blümich and H. W. Spiess, *J. Magn. Reson.* **79** (1988) 269.
- 3.5 E. R. deAzevedo, T. J. Bonagamba and D. Reichert, *Prog. NMR Spectrosc.* **47** (2005) 137.
- 3.6 G. L. Hoatson and R. L. Vold, "NMR: Basic principles and progress", (B. Bluemich, Eds.), Vol. 32, Springer-Verlag, Berlin, 1994.
- 3.7 R. Freeman, "A Handbook of NMR", p. 275, Longman Ltd., London, 1997.

- 3.8 M. M. Maricq and J. S. Waugh, *J. Chem. Phys.* **70** (1979) 3300.
- 3.9 M. J. Duer and C. Stourton, *J. Magn. Reson.* **129** (1997) 44.
- 3.10 J. H. Kristensen, G. L. Hoatson and R. L. Vold, *Solid State NMR* **13** (1998) 1.
- 3.11 J. H. Kristensen, G. L. Hoatson and R. L. Vold, *J. Chem. Phys.* **110** (1999) 4533.
- 3.12 J. H. Kristensen, H. Bildsøe, H. J. Jakobsen and N. C. Nielsen, *J. Magn. Reson.* **39** (1999) 314.
- 3.13 A. Hoffmann and I. Schnell, *Chem. Phys. Chem.* **5** (2004) 966.
- 3.14 M. Hologne and J. Hirschinger, *Solid State NMR* **26** (2004) 1.
- 3.15 A. F. Mehlkopf, D. Korbee, T. A. Tiggelman and R. Freeman, *J. Magn. Reson.* **58** (1984) 315.
- 3.16 U. Friedrich, I. Schnell, S. P. Brown, A. Lupulescu, D. E. Demco and H. W. Spiess, *Mol. Phys.* **95** (1998) 1209.
- 3.17 J. H. Kristensen, H. Bildsøe, H. J. Jakobsen and N. C. Nielsen, *J. Magn. Reson.* **100** (1992) 437.
- 3.18 P. J. Hore, in "Nuclear Magnetic Resonance", Chapter 4, Oxford University Press, Oxford, 1995.
- 3.19 J. R. Long, B. Q. Sun, A. Bowen and R. G. Griffin, *J. Am. Chem. Soc.* **116** (1994) 11950.
- 3.20 J. Virlet, in "Encyclopedia of Nuclear Magnetic Resonance" (D. M. Grant and R. K. Harris, Eds.), Vol. 4, p. 2694, Wiley, Chichester, 1996.
- 3.21 S. E. Ashbrook, S. Antonijevic, A. J. Berry and S. Wimperis, *Chem. Phys. Lett.* **364** (2002) 634.
- 3.22 Z. Gan, *J. Am. Chem. Soc.* **122** (2000) 3242.
- 3.23 K. J. Pike, S. E. Ashbrook and S. Wimperis, *Chem. Phys. Lett.* **345** (2001) 400.
- 3.24 S. E. Ashbrook and S. Wimperis, *Prog. NMR Spectrosc.* **45** (2004) 53.
- 3.25 M. J. Thrippleton, M. Cutajar and S. Wimperis, *Chem. Phys. Lett.* **452** (2008) 233.
- 3.26 M. Cutajar, S. E. Ashbrook and S. Wimperis, *Chem. Phys. Lett.* **423** (2006) 276.
- 3.27 G. Bodenhausen, H. Kogler and R. R. Ernst, *J. Magn. Reson.* **58** (1984) 370.

- 3.28 P. J. Hore, J. A. Jones and S. Wimperis, "NMR: The Toolkit", Oxford University Press, Oxford, 2000, Chapter 6.
- 3.29 S. E. Ashbrook and S. Wimperis, *J. Magn. Reson.* **177** (2005) 44.
- 3.30 D. P. Weitekamp, *Adv. Magn. Reson.* **11** (1983) 111.
- 3.31 O. W. Sørensen, M. Rance and R. R. Ernst, *J. Magn. Reson.* **56** (1984) 527.
- 3.32 L. Zheng, K. W. Fishbein, R. G. Griffin and J. Herzfeld, *J. Am. Chem. Soc.* **115** (1993) 6254.
- 3.33 J. A. Ripmeester, S. K. Garg and D. W. Davidson, *J. Magn. Reson.* **15** (1974) 295.
- 3.34 E. D. Stevens, *Acta. Cryst.* B36 (1980) 1876.
- 3.35 A. J. Berry and M. James, *Am. Miner.* **86** (2001) 181.
- 
- 5.1 A. E. Derome, "Modern NMR Techniques for Chemistry Research", Chapter 4, Pergamon Press, Oxford, 1991.
- 5.2 M. Alla, R. Ecmán and A. Pines, *Chem. Phys. Lett.* **71** (1980) 148.
- 5.3 Z. Gan and P. Robyr, *Mol. Phys.* **95** (1998) 1143.
- 5.4 R. Freeman, "A Handbook of Nuclear Magnetic Resonance", p. 275, Longman Limited, London, 1997.
- 5.5 N. Bloembergen, *Physica* **15** (1949) 386.
- 5.6 E. R. Andrew, S. Clough, L. F. Farnell, T. D. Gledhill and I. Roberts, *Phys. Lett.* **21** (1966) 505.
- 5.7 D. P. Raleigh, G. S. Harbison, T. G. Neiss, J. E. Roberts and R. G. Griffin, *Chem. Phys. Lett.* **138** (1987) 285.
- 5.8 D. P. Raleigh, M. H. Levitt and R. G. Griffin, *Chem. Phys. Lett.* **146** (1988) 71.
- 5.9 M. H. Levitt, D. P. Raleigh, F. Creuzet and R. G. Griffin, *J. Chem. Phys.* **92** (1990) 6347.
- 5.10 T. G. Oas, R. G. Griffin and M. H. Levitt, *J. Chem. Phys.*, **89** (1988) 692.
- 5.11 A. Kubo and C. A. McDowell, *J. Chem. Soc. Faraday Trans.* **184** (1988) 3713.
- 5.12 B. H. Meier, *Adv. Magn. Opt. Reson.* **19** (1994) 1.
- 5.13 R. Eckman, *J. Chem. Phys.* **79** (1983) 524.

- 5.14 S. Antonijevic and S. Wimperis, *J. Magn. Reson.* **164** (2003) 343.
- 5.15 B. Langer, I. Schnell, H. W. Spiess and A. R. Grimmer, *J. Magn. Reson.* **138** (1999) 182.
- 5.16 B. D. Hosangadi and R. H. Dave, *Tetrahedron Lett.* **37** (1996) 6375.
- 5.17 R. Challoner, J. Kümmerlen and C. A. McDowell, *Mol. Phys.* **83** (1994) 687.
- 5.18 H. T. Kwak, P. Srinivasan, J. Quine and D. Massiot, *Z. Gan, Chem. Phys. Lett.* **376** (2003) 75.
- 
- 6.1 S. T. Wilson, B. M. Lok, C. A. Messina, T. R. Cannan and E. M. Flanigen, *J. Am. Chem. Soc.* **104**, 1146 (1982).
- 6.2 B. Zibrowius, U. Lohse and J. Richter-Mendau, *J. Chem. Soc. Faraday Trans.* **87**, 1433 (1991).
- 6.3 R. W. Broach, S. T. Wilson and R. M. Kirchner, in *Proceedings of the 12<sup>th</sup> International Zeolite Conference* (M. M. J. Treacy, B. C. Marcus, M. E. Bisher, and J. B. Higgins, Eds.), Vol. 3, p. 1715, Materials Research Society, Warrendale, 1999.
- 6.4 R. M. Kirchner, R. W. Grosse-Kunstleve, J. J. Pluth, S. T. Wilson, R. W. Broach and J. V. Smith, *Microporous Mesoporous Mater.* **39**, 319 (2000).
- 6.5 J. W. Wiench and M. Pruski, *Solid State Nucl. Magn. Reson.* **26**, 51 (2004).
- 6.6 J. W. Wiench, G. Tricot, L. Delevoye, J. Trebosc, J. Frye, L. Montagne, J. P. Amoureux and M. Pruski, *Phys. Chem. Chem. Phys.* **8**, 144 (2006).
- 6.7 C. Baerlocher, L. B. McCusker and D. H. Olson, "Atlas of Zeolite Framework Types", Elsevier, Amsterdam, 2007.
- 6.8 C. A. Fyfe, H. M. zu Altenschildesche, K. C. Wong-Moon, H. Grondey and J. M. Chezeau, *Solid State Nucl. Magn. Reson.* **9**, 97 (1997).
- 6.9 Z. Gan and H.T. Kwak, *J. Magn. Reson.* **168**, 346 (2004).
- 6.10 T. J. Ball and S. Wimperis, *J. Magn. Reson.* **124**, 279 (2007).

- 6.11 L. Delevoeye, C. Fernandez, C. M. Morais, J. P. Amoureux, V. Montouillout and J. Rocha, *Solid State Nucl. Magn. Reson.* **22**, 501, (2002).
- 6.12 W. P. Power, *J. Am. Chem. Soc.* **117**, 1800 (1995).
- 6.13 M. D. Segall, P. J. D. Lindan, M. J. Probert, C. J. Pickard, P. J. Hasnip, S. J. Clark and M. C. Payne, *J. Phys. Cond. Matt.* **14**, 2717 (2002).
- 6.14 S. J. Clark, M. D. Segall, C. J. Pickard, P. J. Hasnip, M. J. Probert, K. Refson and M. C. Payne, *Z. Krist.* **220**, 567 (2005).
- 6.15 J. P. Perdew, K. Burke and M. Ernzerhof, *Phys. Rev. Lett.* **77**, 3865 (1996).
- 6.16 J. R. Yates, C. J. Pickard and F. Mauri, *Phys. Rev. B* **76**, 024401 (2007).
- 6.17 C. J. Pickard and F. Mauri, *Phys. Rev. B* **63**, 245101 (2001).
- 6.18 S. T. Wilson, B. M. Lokand and E. M. Flanigen, U.S. Pat. 4310440 (1982).
- 6.19 R. W. Broach, S. T. Wilson and R. M. Kirchner, *Micropor. Mesopor. Mater.* **57**, 211 (2003).
- 6.20 S. Antonijevic, S. E. Ashbrook, S. Biedasek, R. I. Walton, S. Wimperis and H. Yang, *J. Am. Chem. Soc.* **128**, 8054 (2006)
- 6.21 A. M. Chippindale, A. V. Powell, R. H. Jones, J. M. Thomas, A. K. Cheetham, Q. Huo and R. Xu, *Acta Crystallogr. C* **50**, 1537 (1994).
- 6.22 J. B. Praise, in: B. Drzaj, S. Hocevar, S. Pejovnik (Eds.), *Zeolites, Studies in Surface Science and Catalysis*, **24**, Elsevier, Amsterdam, 271 (1985).

